

University of Warwick institutional repository: <http://go.warwick.ac.uk/wrap>

A Thesis Submitted for the Degree of PhD at the University of Warwick

<http://go.warwick.ac.uk/wrap/35235>

This thesis is made available online and is protected by original copyright.

Please scroll down to view the document itself.

Please refer to the repository record for this item for information to help you to cite it. Our policy information is available from the repository home page.

AUTHOR: Soheil Vasheghani Farahani DEGREE: Ph.D.

TITLE: MHD wave interaction with coronal active region plasmas

DATE OF DEPOSIT:

I agree that this thesis shall be available in accordance with the regulations governing the University of Warwick theses.

I agree that the summary of this thesis may be submitted for publication.

I **agree** that the thesis may be photocopied (single copies for study purposes only).

Theses with no restriction on photocopying will also be made available to the British Library for microfilming. The British Library may supply copies to individuals or libraries, subject to a statement from them that the copy is supplied for non-publishing purposes. All copies supplied by the British Library will carry the following statement:

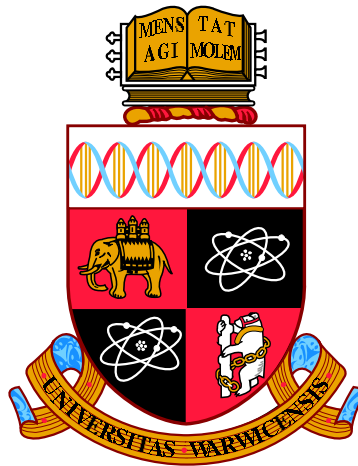
“Attention is drawn to the fact that the copyright of this thesis rests with its author. This copy of the thesis has been supplied on the condition that anyone who consults it is understood to recognise that its copyright rests with its author and that no quotation from the thesis and no information derived from it may be published without the author’s written consent.”

AUTHOR’S SIGNATURE:

USER’S DECLARATION

1. I undertake not to quote or make use of any information from this thesis without making acknowledgement to the author.
2. I further undertake to allow no-one else to use this thesis while it is in my care.

DATE	SIGNATURE	ADDRESS
.....
.....
.....
.....
.....



**MHD wave interaction with coronal active region
plasmas**

by

Soheil Vasheghani Farahani

Thesis

Submitted to the University of Warwick

for the degree of

Doctor of Philosophy

Department of Physics

March 2011

THE UNIVERSITY OF
WARWICK

Contents

Acknowledgments	iv
Declarations	v
Abstract	vi
Chapter 1 Introduction	1
1.1 General review of the Sun	1
1.2 Magnetohydrodynamics (MHD)	4
1.3 MHD waves in uniform medium	8
1.4 Effects of transverse structuring	11
1.5 Effects of parallel structuring	18
1.5.1 Linear wave solution	18
1.5.2 Nonlinear effects	19
1.6 Observational evidence of MHD waves in the solar atmosphere . . .	22
1.6.1 Transverse oscillations	23
1.6.2 Sausage oscillations	25
1.6.3 Longitudinal oscillations	26
1.6.4 Attempts to observe torsional oscillations	28
1.6.5 Anomalous resistivity and magnetic reconnection	29
1.6.6 Quasi-periodic pulsations in solar flares	31
1.6.7 Observations of plasma jets in the corona	33
1.7 Present solar missions	33
Chapter 2 Propagating kink waves in soft X-ray coronal jets	37
2.1 Introduction	37
2.2 Model and equilibrium conditions	39

2.3	Dispersion relations	41
2.4	Expressions for the perturbations of the physical parameters	44
2.5	Estimation of the damping time of kink waves in jets due to resonant absorption	45
2.6	Excitation of transverse waves in jets	50
2.7	Discussions and conclusions	51
 Chapter 3 Long wave-length torsional modes of coronal plasma struc- tures		53
3.1	Introduction	53
3.2	Manifestation of torsional modes in the corona	55
3.3	Model and equilibrium conditions	56
3.4	Dispersion relations	60
3.4.1	Case $J_0 = 0, \Omega_0 = 0$	60
3.4.2	Case $J_0 \neq 0, \Omega_0 = 0$	62
3.4.3	Case $\Omega_0 \neq 0, J_0 \neq 0$, zero- β limit	63
3.4.4	Standing oscillations of an infinite tube	66
3.5	Compressibility of the torsional mode	67
3.6	Conclusions	70
 Chapter 4 Nonlinear long-wave length torsional Alfvén waves		74
4.1	Introduction	74
4.2	Nature of the MHD ponderomotive force	75
4.3	The Cohen-Kulsrud equation	78
4.4	Nonlinear flows induced by Alfvén waves	79
4.5	Compressible flows induced by torsional waves	80
4.6	Propagating torsional waves	83
4.7	Standing torsional waves	86
4.8	Conclusions	88
 Chapter 5 Fast magnetoacoustic waves approaching an X-point		90
5.1	Introduction	90
5.2	Analytical and numerical models of magnetic null-point dynamics . .	91
5.3	Theoretical analysis	92
5.3.1	Model and equilibrium conditions	92
5.3.2	Nonlinear approach	95

5.4	Numerical study	96
5.4.1	Numerical methods	96
5.4.2	Initial setup	97
5.4.3	Phase relations in magnetoacoustic modes	98
5.4.4	Parametric studies	100
5.5	Summary and discussion	104
Chapter 6 Conclusions		106

Acknowledgments

I had the time of my life at the University of Warwick and specially doing my PhD research under the supervision of Prof. Valery Nakariakov. Besides his deep knowledge in physics, Astrophysics, and mathematics which helped me stay on the right path all the way through my research, he is a gentleman which I respect most of all. Valery always answered my questions with patients and never disrespected me even when I asked silly physical questions.

I would like to express my gratitude to my PhD advisor Dr. Erwin Verwichte who always welcomed me for questions on my projects, and also I enjoyed and learned a lot in his lecture course, waves in laboratory and astrophysical plasmas.

I would like to thank Dr. Tom Van Doorselaere who helped me on looking more sharply on the different aspects of MHD wave theory.

I would like to thank Dr. Amir Ali Masoudi who encouraged me to pursue my PhD in the field of MHD wave theory.

I would like to thank the ORS committee for financial support on my PhD research. In the end but most of all I am very grateful to my lovely wife Farkhondeh who has been helping me in all aspects throughout my scientific studies, my mother and father who always provided a peaceful atmosphere for me to study and encouraged me to study and study.

Declarations

Replace this text with a declaration of the extent of the original work, collaboration, other published material etc. You can use any L^AT_EX constructs.

Abstract

Interaction of magnetohydrodynamic (MHD) waves with various structures in a magnetised plasma was considered theoretically in the context of the interpretation of recently observed phenomena in the corona of the Sun. The main emphasis was put on the development of analytical models, utilising various asymptotic techniques based upon the presence of a small parameter. In the consideration of waves guided by field-aligned plasma non-uniformity, such as coronal jets and plumes, the small parameter was the ratio of the diameter of the guiding non-uniformity to the wavelength, the approach known as the “thin flux-tube approximation”. In the consideration of nonlinear effects, the wave amplitude was taken to be finite, but small, and hence could be treated as a small parameter too.

In the thesis, we addressed several specific timely problems of modern solar physics: the interpretation of recently discovered transverse waves on soft X-ray coronal jets in terms of a kink fast magnetoacoustic wave; modelling of enigmatic torsional waves (also known as twisting waves or waves of the electric current) guided by cylindrical coronal structures, such as loops, plumes, filaments and jets, accounting for the effects of the magnetic twisting and rotation of the equilibrium plasma configuration; weakly nonlinear effects appearing during the propagation of the torsional waves along coronal magnetic waveguides, concentrating on the nonlinearly induced compressible perturbations; and nonlinear steepening of fast magnetoacoustic waves in the vicinity of a magnetic null-point, in the context of the possible triggering of magnetic reconnection by the deposition of current-driven anomalous resistivity.

In the first Chapter, we give an overview of the solar atmosphere and dynamical processes observed there such as MHD waves and plasma flows. Also, the set of MHD equations is introduced, and the main modes of a basic coronal plasma structure, a magnetic cylinder, are considered by the method of dispersion relation.

In Chapter 2, we considered the long-wavelength limit in the magnetic cylinder dispersion relations, and derived explicit expressions, which link the phase and group speeds for linear kink magnetoacoustic waves guided by hot plasma jets surrounded by a static plasma. With the use of the derived expressions, we showed that transverse waves recently discovered by Hinode/XRT on coronal jets are the kink waves. In the observationally determined range of parameters, the waves are not found to be subject to either the Kelvin-Helmholtz instability or negative energy wave instabilities, and hence they are likely to be excited at the source of the jet. We also carried out forward modelling of the observables, and demonstrated its consistency with XRT observations.

In Chapter 3 we considered long wave-length axisymmetric magnetohydrodynamic waves, and derived asymptotic dispersion relations linking phase speeds with the plasma parameters using the second order thin flux tube approximation. We showed that when uniform twist and rotation are both present, the phase speed of torsional waves depends upon the direction of the wave propagation. In addition, the twist and rotation causes compressibility of the torsional waves. The phase relations show that in a torsional wave the density and azimuthal magnetic field perturbations are in phase with the axial magnetic field perturbations and anti-phase with tube cross-section perturbations. In a zero- β non-rotating plasma cylinder confined by the equilibrium twist, the density perturbation is found to be about 66 percent of the amplitude of the twist perturbation in torsional waves.

In Chapter 4, we considered the nonlinear phenomena accompanying long-wavelength torsional waves in an untwisted and non-rotating magnetic flux tube. We showed that propagating torsional waves induce compressible perturbations by nonlinear

forces, these compressible perturbations oscillate with double the frequency of the torsional waves. In contrast with plane shear Alfvén waves, the amplitude of compressible perturbations is independent of the plasma- β . But, as in the shear Alfvén wave, the amplitude of compressible perturbations are proportional to the torsional wave amplitude square. It was also shown that standing torsional waves induce compressible perturbations of two kinds, those which grow with the characteristic time inversely proportional to the sound speed, and those which oscillate at double the frequency of the inducing torsional wave. The growing density perturbation saturates at the level, inversely proportional to the sound speed.

In Chapter 5, we studied the generation of fast magnetoacoustic shocks in the vicinity of a magnetic null-point. In the weakly nonlinear limit, we derived a simple wave evolutionary equation, which provided us with the qualitative information about the nonlinear evolution of the fast wave-pulse: formation of the shock and deformation of the initial shape of the perturbation depending upon the polar angle. We compared our analytical solutions with numerical solutions and found that the speed of the fast magnetoacoustic pulse depends on the initial amplitude of the pulse. In our parametric studies we showed that although the initial amplitude of the magnetoacoustic pulse is responsible for the time the pulse overturns, the initial width of the pulse should not be ignored. We showed that narrower and higher amplitude pulses overturn at larger distance from the null-point. In the context of the sympathetic flaring a stronger initial pulse does not guarantee a stronger effect.

Chapter 1

Introduction

1.1 General review of the Sun

Life on Earth depends on the Sun, since it is the main source of energy in the solar system. But the beauty and the fine and nice structures of the Sun's atmosphere which is accompanied by the release of energy is another important reason to study the Sun. The Sun's atmosphere is what we see when we look at the Sun. The solar atmosphere is usually divided into the photosphere, chromosphere and the corona. The temperature of the photosphere decreases with height from 6400 K to 4400 K with an average temperature of about 5800 K and a density between 10^{19}m^{-3} and 10^{20}m^{-3} . The average magnetic field in the photosphere is between 5 G and 10 G, but the magnetic field could reach up to a few kG in magnetic concentrated regions like sunspots and magnetic elements. The upper layer is the chromosphere which lies above the photosphere, and has temperatures between 10,000 and 30,000 K, and density between 10^{16}m^{-3} and 10^{17}m^{-3} . The chromosphere could be seen in a total eclipse as a thin pinkish layer around the disk of the Sun. Next is a sub-layer named the chromosphere-corona transition region where the temperature rises from 20,000 K to 1 MK.

The outer-most part of the solar atmosphere is the corona with temperatures between 1 MK and 10 MK. In the lower corona, at height lower than a few solar radii, the magnetic field is between 1 and 500 G, and density is between 10^{14}m^{-3} and 10^{15}m^{-3} . The solar corona could be seen around the disk of the Sun in a total eclipse and is extended to the edge of the solar system; in other words we could say that we live in the part of the solar corona which is called the solar wind.

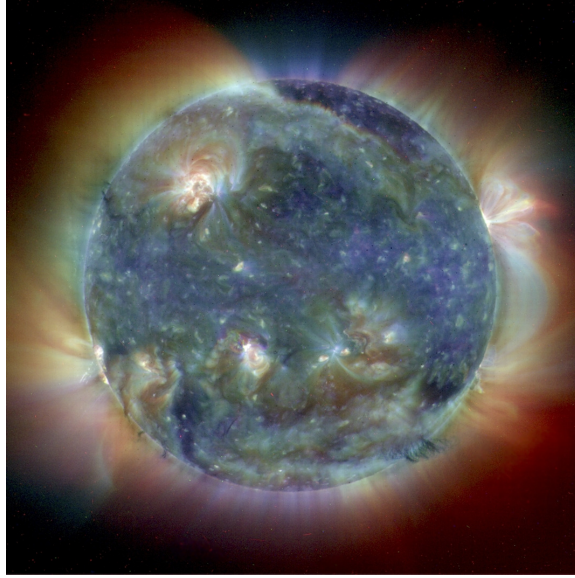


Figure 1.1: A view of the solar atmosphere in its active period with combined EUV (171 Å, 195 Å and 284 Å) images taken by SoHO EIT on May 31, 1998. The bright features are active regions, formed by plasma loops.

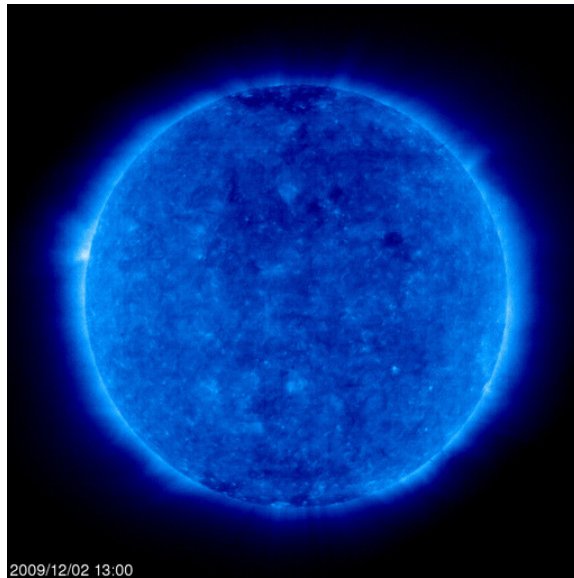


Figure 1.2: A view of the solar atmosphere in its quiet period taken by EIT (171 Å). One active region is seen in the left edge of the solar disk. The dark regions at the poles of the Sun are so-called coronal holes, where the magnetic field is mainly open.

The solar wind is the coronal plasma which extends outward of the solar atmosphere in the solar system with densities less than the solar corona. It contains a frozen-in magnetic flux, and moves at the speeds between 300 km/s and 800 km/s, and highly affects the Earth. The solar wind is responsible for the space weather and it affects telecommunications and satellites orbiting the Earth, affects the Earth's magnetosphere and may cause climate changes on Earth. A very famous and beautiful effect of the solar wind on the Earth's atmosphere is the polar aurora. The solar wind origin and acceleration is one of the aims of studying the Sun.

The Sun has a magnetic cycle of about 11 years, and since the solar activity highly depends on the solar magnetic field, every 11 years the Sun becomes quiet. In Figure 1.1 and Figure 1.2 the Sun is shown while in an active period and in an inactive period (at the time being), which shows that even in the quiet period, still some active regions exist.

To give a deeper insight about the parameters of the solar atmosphere, we could say that the magnetic field has its highest value in the sunspots between 2000 and 3000 G and its lowest value in coronal holes in quiet Sun regions between 0.1 and 0.5 G, gradually decreasing with the expansion of the solar wind. In the visible light sunspots look a bit darker with temperatures about 4000 K which is a bit cooler and less dense than the average temperature and density of the photosphere. Coronal active regions over the sunspots have an average magnetic field between 100 and 300 G, but in some small scale pores the magnetic field could reach up to 1100 G. The electron density in the lower solar corona is 10^{15}m^{-3} , which decreases with height to 10^{12}m^{-3} in the upper solar corona. The electron density is between $0.5 \times 10^{14}\text{m}^{-3}$ and $1 \times 10^{14}\text{m}^{-3}$ in the coronal holes, and is between $1 \times 10^{14}\text{m}^{-3}$ and $2 \times 10^{14}\text{m}^{-3}$ in diffuse quiet Sun regions. The density is between $3 \times 10^{14}\text{m}^{-3}$ and $5 \times 10^{14}\text{m}^{-3}$ at the base of streamers, and is about 10^{17}m^{-3} in the loops [Aschwanden, 2005].

Streamers are usually helmet shaped which is why they are referred to as helmet streamers, and are large structures extending to about several coronal radii. Its lower part looks like concentric loops (closed field lines) where its higher parts looks like an outward flow (open field lines), which makes it overall look like the world war I soldiers' helmet. There are other coronal phenomena in the Sun; loops, jets, plumes, spicules,...etc.. Loops which are closed magnetic field lines looking like a half circle normal to the Sun's surface, with each side on a foot-point having opposite magnetic polarity compared to the other. To give an idea about the size of

coronal loops, Nakariakov et al. [1999] observed a loop 130×10^6 m long. Plumes are cool and dense matter ejected from areas close to the solar poles, that is why they are usually referred to as polar plumes. Spicules are spiky structures normal to the solar atmosphere and are originated in the photosphere or chromosphere. Jets are matter ejecting out of the Sun like an inverse Y shape, and their foot-to-foot distance depends on the layer of the Sun's surface their foot-point's is formed. Shibata et al. [2007] illustrated that coronal jets are larger than chromospheric jets and chromospheric jets are larger than photospheric jets. Jets are studied in more detail in subsection 1.6.7 and Chapter 2. The aim of this thesis is to study the interaction of magnetoacoustic waves with these phenomena.

1.2 Magnetohydrodynamics (MHD)

A successful analytical tool for the study of physical processes in the solar corona is magnetohydrodynamics. In MHD the speeds of bulk plasma flows are non-relativistic, the mass of electrons is neglected compared to the mass of ions. This means that the relative motion of electrons with respect to ions is not considered. In MHD characteristic times are much longer than the ion gyroperiod, the plasma oscillation period, and the mean collision times. It is worth showing here the values of these parameters for coronal conditions where the magnetic field is 10 G and the electron density (n_e) is $5 \times 10^{14} \text{ m}^{-3}$,

$$\begin{aligned} f_{\text{plasma}} &\approx 2 \times 10^8 \text{ Hz}, \\ f_{\text{gyro}} &\approx 1.52 \times 10^4 \text{ Hz}. \end{aligned} \tag{1.1}$$

Also, the characteristic spatial scales described by MHD are much larger than the ion Larmour radius and mean free path length which is between 10^5 m and 10^6 m for typical coronal conditions. Thus, MHD represents large scale, slow dynamics and low frequency waves in plasmas.

Since in the solar atmosphere the speeds of observed plasma motions are not higher than a few thousand km per seconds MHD theory works fine. But applying MHD theory to astrophysical plasmas needs careful attention because sometimes the speeds are close to the speed of light, but with some restrictions MHD theory proves adequate for modelling astrophysical plasmas too.

MHD theory is widely used to describe and model macroscopic (large scale) behaviour of the plasmas of the Sun's atmosphere. It could also be applied to describe the macroscopic behaviour of laboratory space and astrophysical plasmas. Considering the plasma as a fluid and keeping in mind that a plasma is an ionised medium we deduce that the plasma is an electrically conducting fluid. So to obtain a closed set of equations one may use the single-fluid approximation and equations for mass, momentum and internal energy from fluid dynamics, and also Ohm's law and Maxwell's equations. Note that due to conduction there is an electric current and an electric current produces magnetic fields (see [Goossens, 2003]).

$$\rho \frac{\partial \mathbf{V}}{\partial t} + \rho(\mathbf{V} \cdot \nabla) \mathbf{V} = -\nabla p - \frac{1}{\mu} \mathbf{B} \times \nabla \times \mathbf{B} + \mathbf{F}, \quad (1.2)$$

$$\frac{\partial \mathbf{B}}{\partial t} = \nabla \times (\mathbf{V} \times \mathbf{B}) + \eta \nabla^2 \mathbf{B}, \quad (1.3)$$

$$\frac{\partial \rho}{\partial t} + \nabla \cdot (\rho \mathbf{V}) = 0, \quad (1.4)$$

$$\frac{\rho^\gamma}{\gamma - 1} \frac{d}{dt} \left(\frac{p}{\rho^\gamma} \right) = -\mathcal{L}, \quad (1.5)$$

$$\nabla \cdot \mathbf{B} = 0. \quad (1.6)$$

This set of MHD equations relates the plasma velocity \mathbf{V} , the magnetic field \mathbf{B} , the plasma pressure p , and the plasma mass density ρ . Here γ is the ratio of the specific heats which is usually considered as 5/3, μ is the magnetic permeability, \mathcal{L} is the energy loss or gain function, and η is the magnetic diffusivity:

$$\eta = \frac{1}{\mu \sigma}. \quad (1.7)$$

where σ is the electrical conductivity.

The term \mathbf{F} is an external force, e.g. of the form

$$\mathbf{F} = -\rho \mathbf{g} + \nu \rho [\nabla^2 \mathbf{V} + \frac{1}{3} \nabla (\nabla \cdot \mathbf{V})] \quad (1.8)$$

where \mathbf{g} and ν are gravity and kinematic viscosity, respectively. However other forces could still be present and taken into account like the centrifugal, Coriolis, etc. Equation (1.2) is the Euler equation which is a vector equation and has three scalar components, equation (1.3) is the induction equation and is also a vector equation and has three scalar components, equation (1.4) is the continuity equation which shows the conservation of mass, and equation (1.5) is the energy equation. In case of no deposition or dissipation of energy ($\mathcal{L}=0$), equation (1.5) would reduce to the simple adiabatic equation, or in other words the adiabatic gas law.

It is worth introducing two plasma physics parameters which are very important in describing different regions of the solar atmosphere. On the right hand side of the induction equation (1.3) the first term is the convective and the second is the diffusion term. These terms describe a very different behaviour of the plasma, the ratio of these terms is called the magnetic Reynolds number,

$$R_m = \frac{\nabla \times (\mathbf{V} \times \mathbf{B})}{\eta \nabla^2 \mathbf{B}} \approx \frac{VL}{\eta}, \quad (1.9)$$

where L and V are the characteristic length and velocity scale of the considered plasma motion, respectively. Consider two limiting regimes corresponding to different values of R_m . If $R_m \ll 1$, the magnetic diffusivity plays a much greater role than the convective motions, meaning in equation (1.3) the convective term could be neglected, since its effect has become very weak compared to the diffusive effect,

$$\frac{\partial}{\partial t} \mathbf{B} = \eta \nabla^2 \mathbf{B}. \quad (1.10)$$

Equation (1.10) is a vector diffusion equation, it could be deduced that the magnetic field lines diffuse from higher magnetic field regions to lower magnetic field regions. Meaning that after a specific length scale, the magnetic field diffuses, or obtains a constant value in all regions. On the other hand, the case $R_m \gg 1$ means that the magnetic diffusivity is weak in the considered length scale and could be neglected compared to the convective term in equation (1.3)

$$\frac{\partial}{\partial t} \mathbf{B} = \nabla \times (\mathbf{V} \times \mathbf{B}). \quad (1.11)$$

Equation (1.11) means, since there is no diffusivity of the magnetic field lines, the plasma and the magnetic field lines are “glued” together and neither falls behind or goes ahead. This is a condition named frozen-in which happens in a perfectly

conducting regime which in such a case the magnetic flux passing through any closed path having the same speed as the plasma velocity does not depend on time (for a very detailed study see e.g. Goossens [2003]).

The other important parameter is the plasma- β which is defined as the ratio of the plasma pressure to the magnetic pressure,

$$\beta = \frac{p_{\text{plasma}}}{p_{\text{magnetic}}} = \frac{C_s^2 \rho / \gamma}{B^2 / 2\mu} \approx \frac{C_s^2}{C_A^2}, \quad (1.12)$$

where $C_s^2 = (\gamma p / \rho)$ is the sound speed, and $C_A^2 = (B^2 / \mu \rho)$ is the Alfvén speed. The Alfvén speed is a characteristic speed which indicates the speed of a purely magnetic incompressible wave named as the Alfvén wave in honour of Hannes Alfvén. In order to show the contribution of plasma- β in the MHD equations, we use equation (1.2) and the mathematical relation

$$\nabla (B^2) = 2(\mathbf{B} \cdot \nabla) \mathbf{B} + 2\mathbf{B} \times (\nabla \times \mathbf{B}), \quad (1.13)$$

we obtain

$$\rho \frac{\partial \mathbf{V}}{\partial t} + \rho (\mathbf{V} \cdot \nabla) \mathbf{V} = -\nabla \left(p + \frac{B^2}{2\mu} \right) + \frac{1}{\mu} (\mathbf{B} \cdot \nabla) \mathbf{B} + \mathbf{F}, \quad (1.14)$$

The first term on the RHS of equation (1.14) is the force connected to the total pressure p_T , and the second term is the magnetic tension force. The total pressure force shows the contribution of the gas pressure gradient and the magnetic pressure gradient where the value of β gives information about the dominant pressure gradient.

In particular, in the solar corona the magnetic pressure is usually dominant over the gas pressure and the plasma- β is much smaller than unity, between 0.01 and 0.1. Hence, in the MHD equations the plasma pressure could be neglected for all motions except the motion along the magnetic field. But in the photosphere the plasma- β is greater than 1. In fact this is a very interesting feature because the propagation of MHD perturbations highly depends on whether the magnetic pressure gradient or the plasma pressure gradient is dominant.

Gradients of the magnetic field can be described in terms of electric current

$$\mathbf{j} = \frac{1}{\mu} \nabla \times \mathbf{B}. \quad (1.15)$$

The use of MHD equations allows one to calculate the electric field \mathbf{E} and the temperature T .

1.3 MHD waves in uniform medium

In this section we simplify MHD equations (1.2)-(1.5) and determine the types of waves that exist in unbounded uniform plasmas. Consider the case when dissipative processes are neglected, also not taking into account the term $-\rho g$, we obtain the ideal MHD equations

$$\rho \frac{\partial \mathbf{V}}{\partial t} + \rho(\mathbf{V} \cdot \nabla) \mathbf{V} = -\nabla p - \frac{1}{\mu} \mathbf{B} \times \nabla \times \mathbf{B}, \quad (1.16)$$

$$\frac{\partial \mathbf{B}}{\partial t} = \nabla \times (\mathbf{V} \times \mathbf{B}), \quad (1.17)$$

$$\frac{\partial \rho}{\partial t} + \nabla \cdot (\rho \mathbf{V}) = 0, \quad (1.18)$$

$$p = C_s^2 \rho \quad (1.19)$$

Consider an equilibrium as:

$$\vec{B}_0 = B_0 \mathbf{e}_x, \quad \vec{V}_0 = 0, \quad \rho_0 = \text{const}, \quad p_0 = \text{const}, \quad (1.20)$$

where the index 0 indicates the equilibrium quantities. Linearising the ideal MHD equations around the equilibrium and neglecting the effect of gravity, we obtain two decoupled wave equations:

$$\left(\frac{\partial^4}{\partial t^4} - (C_s^2 + C_A^2) \frac{\partial^2}{\partial t^2} \nabla^2 + C_s^2 C_A^2 (\mathbf{1}_{\parallel} \cdot \nabla)^2 \nabla^2 \right) p_T = 0, \quad (1.21)$$

where $\mathbf{1}_{\parallel}$ is the unit vector in the parallel direction.

$$\left(\frac{\partial^2}{\partial t^2} - C_A^2 (\vec{1}_{\parallel} \cdot \nabla)^2 \right) J_{\parallel} = 0, \quad (1.22)$$

which is second order in time, and J_{\parallel} is the projection of the current density on the x -axis.

Considering plane waves propagating along e_x , we make the Fourier decomposition of the perturbation of the perturbed parameters with ω the frequency and k longitudinal wave number $\propto \exp i(kx - \omega t)$, which means we could take $\frac{\partial}{\partial t} = -i\omega$ and $\nabla = i\mathbf{k}$. Also due to symmetry, propagation along the z -direction could be ignored ($k_z = 0$).

The condition of the non-trivial solution of equation (1.21) is

$$\frac{\omega}{k} = \pm \left(\frac{1}{2} C_A^2 (\beta + 1) \left(1 \pm \sqrt{1 - 4 \frac{\beta}{(\beta + 1)^2} \cos^2 \varphi} \right) \right)^{1/2}, \quad (1.23)$$

where φ is the angle between the wave vector and the magnetic field. Equation (1.23) is dispersion relation linking the frequency and wave number with the parameters of the plasma. The ratio of the frequency and the wave number ω/k , is the phase speed. The positive and negative signs outside the brackets mean that the wave propagates in two opposite directions and the positive and negative signs inside the brackets refer to the phase speeds of the fast and slow magnetoacoustic waves, respectively. In equation (1.23) the plasma- β plays an important role in the phase speed of the fast and slow magnetoacoustic waves, which means that the magnetic and plasma pressure forces are the restoring forces for the propagation of these wave. These waves are compressible, as the perturbation of the total pressure in equation (1.21) induces perturbations of the plasma density. Also from equation (1.23) we notice that the slow wave phase speed is zero when the plasma- β is zero, this limit is called ‘‘The cold plasma limit’’.

Similarly, (1.22) gives the dispersion relation

$$\frac{\omega}{k} = \pm C_A \cos \varphi, \quad (1.24)$$

which describes the phase speed of another wave, called the Alfvén wave with the positive and negative signs meaning the Alfvén wave also propagates in two opposite directions. Note that in equation (1.22) the current density comes into play, which means that for the Alfvén wave the restoring force is the magnetic tension, due to the curvature of the field lines. Note that the linear Alfvén wave propagates in the direction of the magnetic field lines, it is a purely magnetic wave with no density and pressure perturbations. Hence, an Alfvén wave is incompressible. Another interest-

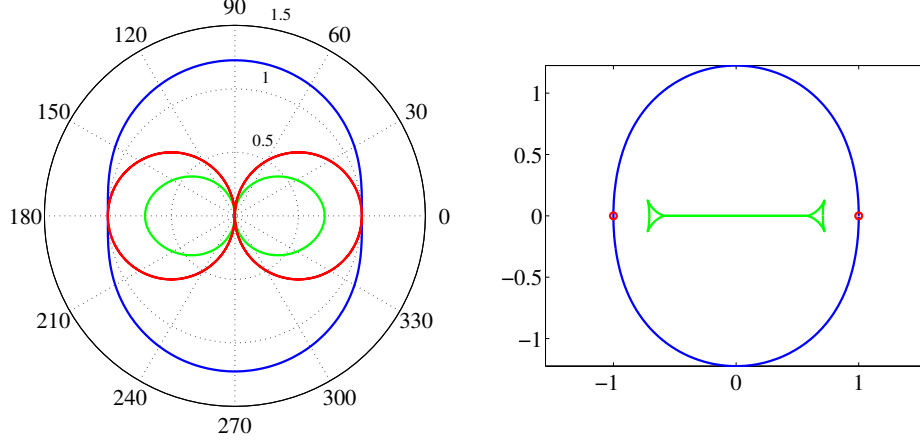


Figure 1.3: The left panel shows polar plots of the phase speeds and the right panel shows polar plots of the group speeds of MHD waves. The fast and slow magnetoacoustic waves are shown in blue and green, respectively, and the Alfvén wave is shown in red. The speeds are all normalised by the Alfvén speed.

ing deduction from equations (1.23) and (1.24) is that since the phase speeds do not depend on the wave number, the Alfvén wave, and the fast and slow magnetoacoustic waves are non-dispersive: all spectral components propagate at the same speeds. Both equations (1.23) and (1.24) contain the dependence on the propagation angle φ . Hence, the waves are anisotropic, and their properties depend on the direction of propagation. To illustrate that, we show the dependence of phase and group speeds on the angle φ in Figure 1.3. In the left-hand panel of Figure 1.3, it could be seen from the phase speed diagram that the slow magnetoacoustic wave and the Alfvén wave are anisotropic, meaning their properties depend upon the angle between the wave vector and the magnetic field. Alfvén and slow waves do not propagate perpendicular to the magnetic field. In contrast, the fast magnetoacoustic wave is almost isotropic and can propagate perpendicular to the magnetic field. In the right hand panel of Figure 1.3 which shows the group speed polar diagram and indicates the energy propagation in the waves, shows that the energy of the slow magnetoacoustic wave and the Alfvén wave propagates along the field line and is anisotropic, but for

the fast magnetoacoustics wave the energy propagation is almost isotropic.

1.4 Effects of transverse structuring

In this subsection, we follow the analysis by Edwin and Roberts [1983] to consider the different kinds of oscillations in a basic plasma structure, magnetic flux tube. The effects of magnetic structuring are taken into account but the effects of gravity are neglected (Figure 1.4). The cylindrical geometry is used to model a homogeneous magnetised plasma in the solar atmosphere which is known as the magnetic flux tube and is a very wide spread magnetic configuration. For example, it could be used for coronal loops, plumes, spicules, jets, prominence filaments. Consider an untwisted non-rotating plasma cylinder, extended along a straight uniform magnetic field (Figure 1.4). If B_{z0} and B_{ze} are the equilibrium magnetic fields inside and outside the cylinder respectively, p_0 and p_e the equilibrium gas pressure inside and outside the cylinder respectively, and ρ_0 and ρ_e the equilibrium mass density inside and outside the cylinder respectively, the total pressure balance implies:

$$p_0 + B_0^2/2\mu = p_e + B_e^2/2\mu. \quad (1.25)$$

Hence the ratio of the outside density to the inside density is:

$$\frac{\rho_e}{\rho_0} = \frac{2C_{s0}^2 + \gamma C_{A0}^2}{2C_{se}^2 + \gamma C_{Ae}^2}, \quad (1.26)$$

where $C_{s0} = (\gamma p_0/\rho_0)^{1/2}$ and $C_{se} = (\gamma p_e/\rho_e)^{1/2}$ are the sound speeds inside and outside the tube, respectively, $C_{A0} = B_0/\sqrt{\mu\rho_0}$ and $C_{Ae} = B_e/\sqrt{\mu\rho_e}$ are the Alfvén speeds inside and outside the tube, respectively. Linearising the ideal MHD equations about the equilibrium we obtain:

$$\mu\rho_0 \frac{\partial v_r}{\partial t} = -\mu \frac{\partial p}{\partial r} + B_0 \frac{\partial B_r}{\partial z} - B_0 \frac{\partial B_z}{\partial r} \quad (1.27)$$

$$\mu\rho_0 \frac{\partial v_\varphi}{\partial t} = \frac{B_0}{r} \frac{\partial}{\partial z} (r B_\varphi) - \frac{B_0}{r} \frac{\partial B_z}{\partial \varphi} \quad (1.28)$$

$$\rho_0 \frac{\partial v_z}{\partial t} = -\frac{\partial p}{\partial z} \quad (1.29)$$

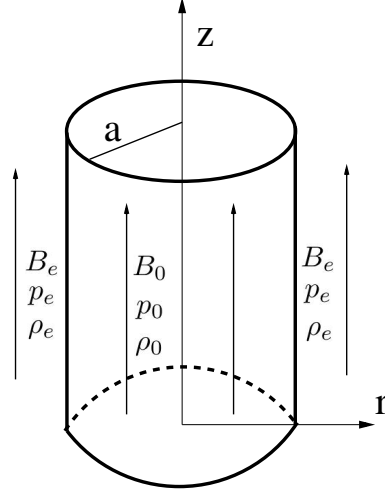


Figure 1.4: The sketch of a magnetised cylindrical flux tube with radius a , density ρ_0 , and gas pressure p_0 embedded in a magnetised medium with density ρ_e and gas pressure p_e . Both magnetic fields inside and outside the tube are parallel to the z -direction.

$$\frac{\partial B_r}{\partial t} = \frac{1}{r} \frac{\partial}{\partial z} (r B_0 v_r) \quad (1.30)$$

$$\frac{\partial B_\varphi}{\partial t} = \frac{\partial}{\partial z} (B_0 v_\varphi) \quad (1.31)$$

$$\frac{\partial B_z}{\partial t} = -\frac{1}{r} \frac{\partial}{\partial r} (r B_0 v_r) - \frac{1}{r} \frac{\partial}{\partial \varphi} (B_0 v_\varphi) \quad (1.32)$$

$$\frac{\partial \rho}{\partial t} + \frac{1}{r} \frac{\partial}{\partial r} (r \rho v_r) + \frac{1}{r} \frac{\partial}{\partial \varphi} (\rho v_\varphi) + \frac{1}{r} \frac{\partial}{\partial z} (r \rho v_z) = 0 \quad (1.33)$$

$$\frac{\partial}{\partial t} p - C_s^2 \frac{\partial \rho}{\partial t} = 0, \quad (1.34)$$

after some algebra two partial differential equations. One is a second-order partial differential equation for the Alfvén wave

$$\left(\frac{\partial^2}{\partial t^2} - C_A^2 \frac{\partial^2}{\partial z^2} \right) \Gamma = 0, \quad (1.35)$$

where

$$\Gamma = \frac{1}{r} \frac{\partial}{\partial r} (r v_\varphi) - \frac{1}{r} \frac{\partial}{\partial \varphi} v_r, \quad (1.36)$$

where it is also known as the torsional wave which is discussed in Chapters 3 and 4. The other is a fourth-order differential equation which is for magnetoacoustic waves [Edwin and Roberts, 1983],

$$\frac{\partial^2}{\partial t^2} \left(\frac{\partial^2}{\partial t^2} - (C_{s0}^2 + C_A^2) \nabla^2 \right) \Delta + C_{s0}^2 C_A^2 \frac{\partial^2}{\partial z^2} \nabla^2 \Delta = 0, \quad (1.37)$$

where ∇^2 is the Laplacian operator in cylindrical coordinates (r, θ, z) .

$$\nabla^2 \equiv \frac{\partial^2}{\partial r^2} + \frac{1}{r} \frac{\partial}{\partial r} + \frac{1}{r^2} \frac{\partial^2}{\partial \varphi^2} + \frac{\partial^2}{\partial z^2}, \quad (1.38)$$

and

$$\Delta = \nabla \cdot \mathbf{V}. \quad (1.39)$$

Equation (1.37) is a cylindrical analogue of equation (1.21). Note that the divergence of \mathbf{V} is a measure of the plasma compressibility. This could be shown from equation (1.4),

$$\frac{\partial}{\partial t} \rho = -\rho \nabla \cdot \mathbf{V} - \mathbf{V} \cdot \nabla \rho, \quad (1.40)$$

where for ρ being constant (incompressible case) we obtain

$$\nabla \cdot \mathbf{V} = 0. \quad (1.41)$$

Hence equation (1.37) describes compressible perturbations. Consider all the perturbed quantities proportional to $\exp i(\omega t + m\varphi + kz)$ and since we are looking at transverse structuring, only take into account the variations in the radial direction, we could write

$$\Delta = R(r) \exp i(\omega t + m\varphi + kz), \quad (1.42)$$

where m is the azimuthal wave number. We cannot make the Fourier transform with respect to the radial coordinate r , as the equilibrium quantities are non-uniform in this direction. Substituting equation (1.42) in equation (1.37) for the internal

medium, we obtain

$$\frac{d^2 R}{dr^2} + \frac{1}{r} \frac{dR}{dr} - \left(m_0^2 + \frac{m^2}{r^2} \right) R = 0, \quad (1.43)$$

which is a Bessel equation in terms of $R(r)$ and

$$m_0^2 = \frac{(k^2 C_{s0}^2 - \omega^2)(k^2 C_{A0}^2 - \omega^2)}{(C_{s0}^2 + C_{A0}^2)(C_{T0}^2 k^2 - \omega^2)}, \quad C_{T0}^2 = \frac{C_{s0}^2 C_{A0}^2}{C_{s0}^2 + C_{A0}^2}. \quad (1.44)$$

A similar equation describes the perturbations in the external medium with m_0 substituted by m_e

$$m_e^2 = \frac{(k^2 C_{se}^2 - \omega^2)(k^2 C_{Ae}^2 - \omega^2)}{(C_{se}^2 + C_{Ae}^2)(C_{Te}^2 k^2 - \omega^2)}, \quad C_{Te}^2 = \frac{C_{se}^2 C_{Ae}^2}{C_{se}^2 + C_{Ae}^2}, \quad (1.45)$$

where C_{Te} is the outside tube speed. Its solutions depend on the sign of m_0^2 , the solutions could be either the Bessel functions $J_{\pm m}(r)$, $Y_m(r)$ in case of a negative sign for m_0^2 , or modified Bessel functions $I_{\pm m}(r)$, $K_m(r)$ in case of a positive sign for m_0^2 [Abramowitz et al., 1988]. The bounded solution for the internal medium in coronal conditions would be

$$R(r) = \begin{cases} A_0 I_m(m_0 r), & \text{if } m_0^2 > 0 \\ A_0 J_m(n_0 r), & \text{if } m_0^2 = -n_0^2 < 0 \end{cases}, \quad (1.46)$$

where $I_m(m_0 r)$ is the solution for surface waves and C_{T0} is the inside tube speed and $J_m(n_0 r)$ is the solution for body waves [Roberts et al., 1984].

For the external medium the solution would be:

$$R(r) = A_e K_m(m_e r), \quad (1.47)$$

Note that in order to have oscillatory behaviour of trapped modes in the tube and evanescent behaviour of them outside the tube we need to have $m_e^2 > 0$. So body waves oscillate inside the tube and are evanescent outside, but surface waves are evanescent in both regimes. In this stage in order to eliminate the two coefficients A_0 and A_e we apply the two boundary conditions which are the continuity of the Lagrangian displacement across the boundary and the total pressure balance at the boundary of the cylinder with radius a , we obtain as the condition for the existence

of a non-trivial solution

$$\frac{\rho_0}{\rho_e} \frac{(k^2 C_{A0}^2 - \omega^2)}{(k^2 C_{Ae}^2 - \omega^2)} \frac{m_e}{m_0} \frac{K'_m(m_e a)}{K_m(m_e a)} = \frac{I'_m(m_0 a)}{I_m(m_0 a)}, \quad (1.48)$$

for surface waves ($m_0^2 > 0$), and

$$\frac{\rho_0}{\rho_e} \frac{(k^2 C_{A0}^2 - \omega^2)}{(k^2 C_{Ae}^2 - \omega^2)} \frac{m_e}{n_0} \frac{K'_m(m_e a)}{K_m(m_e a)} = \frac{J'_m(n_0 a)}{J_m(n_0 a)}, \quad (1.49)$$

for body waves ($n_0^2 = -m_0^2 > 0$). Equations (1.48) and (1.49) are dispersion relations which relate the frequency ω to the longitudinal wave number k and the parameters of the flux tube. Equations (1.48) and (1.49) are transcendental implicit algebraic equations that do not have general exact analytical solutions.

There is another category which the magnetoacoustic waves are divided into and that is slow and fast. If $\beta < 1$, fast refers to a magnetoacoustic wave whose dynamics are controlled by the gradient in the magnetic pressure, and slow refers to a magnetoacoustic wave whose dynamics are controlled by the plasma gas pressure gradient.

The shape of the eigen-functions is largely determined by the parameter m through the order of the Bessel function and the angular dependence $\exp(i m \varphi)$. In case of $m = 0$, the mode of oscillation has a symmetrical (in respect to the axis of the tube) sausage shape without any displacement of the tube axis, hence it is called the sausage mode. In case of $m = 1$ the mode of oscillation has an oscillation around the axis of the tube which is called the kink mode; in this mode the axis of the tube has a transverse oscillation. In case of $m = 2, 3, \dots$ the oscillations unlike the $m = 0$ mode are not symmetric and the value of m indicates the number of nodes; in this mode the tube axis has no transverse displacement and is called the ballooning mode. The observation and dispersion relation of the kink mode is discussed in subsection 1.6.1 and Chapter 2, and the observation and dispersion relation of the sausage mode is discussed in subsection 1.6.2 and Chapter 3.

Figure 1.5 shows the dispersion curves for the trapped fast and slow sausage $m = 0$, kink $m = 1$, and ballooning modes $m > 1$ for typical coronal conditions ($\beta < 1, C_{se} < C_{s0}, C_{Ae} > C_{A0}$) using equation (1.49). It shows that except the fundamental sausage mode, all other fast fundamental modes approach the kink

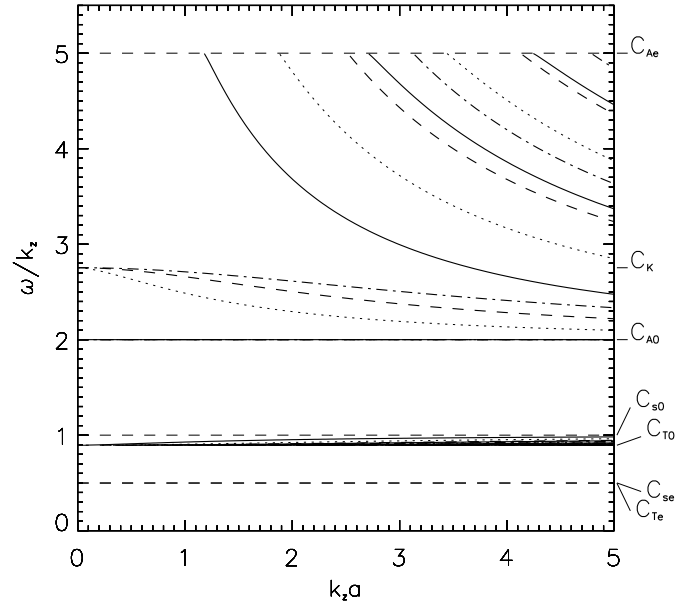


Figure 1.5: Dispersion curves for the phase speeds of the fast and slow magnetoacoustic waves [Nakariakov and Verwichte, 2005] plotted using equation (1.49) for coronal conditions normalised by the internal sound speed. The values for the characteristic speeds are $C_{A0} = 2C_{s0}$, $C_{Ae} = 5C_{s0}$, and $C_{se} = 0.5C_{s0}$. The solid, dotted, dashed and dash-dotted curves correspond to the sausage, kink, and flute or ballooning modes, respectively. The solid straight line with $\omega/k_z = 2$, is for the torsional Alfvén wave.

speed

$$C_k^2 = \frac{\rho_0 C_{A0}^2 + \rho_e C_{Ae}^2}{\rho_0 + \rho_e}, \quad (1.50)$$

in the long wave-length ($ka \rightarrow 0$) limit. Also the curves show that the phase speeds of the trapped fast magnetoacoustic modes are situated between the inside and outside Alfvén speeds and the slow modes only exist in a narrow band between the inside tube and sound speeds. Note that using the cylindrical geometry for modelling the coronal loops ($\beta \ll 1$) in an untwisted plasma cylinder, no surface waves exist [Edwin and Roberts, 1983]. But in case of the slab geometry, if there exists a shear between the magnetic field and the fast magnetoacoustic wave there are surface waves [Nakariakov and Verwichte, 2005].

It could be noticed that the fast modes are highly dispersive in the long wave length limit and only the fundamental kink mode survives at $k = 0$ and travels with the characteristic kink speed which depends on the inside and outside densities and Alfvén speeds. An important feature in Figure 1.5 is that except for the fundamental kink mode all other modes have speeds tending to infinity in the long wave-length limit $ka \rightarrow 0$. Trapped waves need to be within the internal and external Alfvén speeds, hence the maximum speed that trapped modes could obtain is the external Alfvén speed. Modes with speeds above the external Alfvén speed leak out. Hence, the cutoff values are the values for ka where each mode is about to exceed the external Alfvén speed and could be obtained using the roots of the Bessel function. These values are 1.17, 1.87, and 2.51 for the first harmonic of the sausage, kink, and ballooning modes for typical coronal conditions respectively. For values higher than the cutoff we would have leaky waves. Trapped modes may become leaky modes (or in other words radiate out) by changing the boundaries of the cylinder or any physical parameter, leaky modes have complex frequencies. Thus the main four modes of a plasma cylinder are: sausage, kink, ballooning, and longitudinal. However, torsional or rotational waves which travel at the Alfvén speed also exist in coronal structures and could be considered as Alfvén waves. Properties of these waves are discussed in detail in Chapters 3 and 4.

It was shown that magnetoacoustic waves are guided by cylindrical plasma structures. This introduces wave dispersion, making different spectral harmonics propagate at different speeds. In general, transverse structuring of the plasma introduces guided propagation of magnetoacoustic waves. The phase speed diagram showed that the wave guide could make the fast magnetoacoustic wave propagate parallel

to the magnetic field which would not be the case in a uniform structure. In the next subsection the effects of longitudinal stratification will be taken into account.

1.5 Effects of parallel structuring

1.5.1 Linear wave solution

In this subsection we follow the analysis by Ofman et al. [1999].

The solar corona is structured not only across the magnetic field, but also along. In this section we illustrate how this structuring can be taken into account, using a simple example. A one dimensional model in spherical coordinates is considered to describe linear slow magnetoacoustics waves propagating radially along the magnetic field in the solar atmosphere. The magnetic field is normal to the solar surface, and the gravity causes longitudinal structuring. The equilibrium density is:

$$\rho_0 = \rho_{00} \exp \left[-\frac{R_\odot}{H} \left(1 - \frac{R_\odot}{r} \right) \right], \quad (1.51)$$

where ρ_{00} is the equilibrium density amplitude and R_\odot is the Sun's radius, $H = 2k_B T R_\odot^2 / (G M_\odot m_H)$ is the scale height, with M_\odot , k_B , T , G and m_H being the Sun's mass, Boltzman's constant, temperature which is taken constant here, gravitational constant, and hydrogen mass respectively. The coordinate system is the spherical (r, φ, θ) and the waves are assumed spherical and propagate in the radial direction. In this case $\partial/\partial\theta$ and $\partial/\partial\varphi$ are both zero.

Linearising the ideal MHD equations and considering only the perturbations of ρ and v_r , meaning that the perturbations of v_θ and v_φ and the corresponding components of the magnetic field are zero, we obtain:

$$\rho_0 \frac{\partial v_r}{\partial t} + C_s^2 \frac{\partial \rho}{\partial r} + \rho g = 0, \quad (1.52)$$

which is the radial component of the Euler equation (1.2) with $g = GM_\odot/r^2$ being the gravity, and

$$\frac{\partial \rho}{\partial t} + \frac{1}{r^2} \frac{\partial}{\partial r} (r^2 \rho_0 v_r) = 0, \quad (1.53)$$

which is obtained from the continuity equation (1.4). In equation (1.52) we assumed the equilibrium temperature and hence the sound speed to be constant.

Note that the equilibrium value of v_{r0} is taken zero, thus the plasma up flows are

neglected. Eliminating v_r from equations (1.52) and (1.53) we obtain the spherical wave equation,

$$\frac{\partial^2 \rho}{\partial t^2} - \frac{C_s^2}{r^2} \frac{\partial}{\partial r} \left(r^2 \frac{\partial \rho}{\partial r} \right) - g \frac{\partial \rho}{\partial r} = 0, \quad (1.54)$$

which describes slow magnetoacoustic waves. Because of the symmetry of the problem, the waves propagate strictly along the field, they degenerate to acoustic waves. A similar expression to equation (1.54) has been derived by Torkelsson and Boynton [1998]. The amplitude of wave, propagating upwardly at the constant speed C_s , can be approximated as:

$$\rho \approx \frac{R_\odot}{r} \exp \left[-\frac{R_\odot}{2H} \left(1 - \frac{R_\odot}{r} \right) \right]. \quad (1.55)$$

Equation (1.55) shows that the amplitude of the density perturbations decreases with the increase in altitude. The ratio of the density perturbation and the equilibrium density could be obtained by equations (1.55) and (1.51):

$$\frac{\rho}{\rho_0} \approx \frac{R_\odot}{r \rho_{00}} \exp \left[\frac{R_\odot}{2H} \left(1 - \frac{R_\odot}{r} \right) \right]. \quad (1.56)$$

Equation (1.56) shows that the ratio of the density perturbation amplitude and the equilibrium density is growing with altitude. Since the relative amplitude is growing and the nonlinear effects depend on the amplitude, the nonlinear effects could not be neglected any longer and they need to come into play.

We would like to point out that the density profile given by equation (1.51) does not tend to zero when $r/R_\odot \rightarrow \infty$. Hence this model is applicable in the lower corona for $r/R_\odot < 5$, where the solar wind begins, only.

1.5.2 Nonlinear effects

In this subsection we follow the analysis by Ofman et al. [2000].

Taking into account weakly nonlinear effects, meaning $\rho/\rho_0 \ll 1$, where ρ is a perturbation of density, and considering only the quadratically nonlinear terms, equations (1.52) and (1.53) should be modified:

$$\rho_0 \frac{\partial v_r}{\partial t} + C_s^2 \frac{\partial \rho}{\partial r} + \rho g = N_1, \quad (1.57)$$

$$\frac{\partial \rho}{\partial t} + \frac{1}{r^2} \frac{\partial}{\partial r} (r^2 \rho_0 v_r) = N_2, \quad (1.58)$$

where

$$N_1 = -\frac{\partial}{\partial t}(\rho v_r) - \frac{1}{r^2} \frac{\partial}{\partial r}(r^2 \rho_0 v_r^2), \quad (1.59)$$

$$N_2 = -\frac{1}{r^2} \frac{\partial}{\partial r}(r^2 \rho v_r). \quad (1.60)$$

Combining equations (1.57) and (1.58), we obtain:

$$\frac{\partial^2 \rho}{\partial t^2} - \frac{C_s^2}{r^2} \frac{\partial}{\partial r} \left(r^2 \frac{\partial \rho}{\partial r} \right) - g \frac{\partial \rho}{\partial r} = \frac{\partial N_2}{\partial t} - \frac{1}{r^2} \frac{\partial}{\partial r}(r^2 N_1). \quad (1.61)$$

Equation (1.61) reduces to equation (1.54) in case of neglecting the nonlinear terms. Note that v_r can be excluded from the RHS of equation (1.61), if one takes the linear dependence v_r on ρ from equation (1.57).

If we consider the wavelength small compared to the scale height ($\frac{\lambda}{H} \ll 1$), and consider the modification of the waves to be slow, we may use the WKB approximation to find the asymptotic solution to equation (1.61). If the nonlinear terms are neglected, one solution of equation (1.61) is the linear wave propagating upwards, with the amplitude given by equation (1.55) at the sound speed. In the WKB approximation we can consider the slow evolution of the wave amplitude and shape caused by the weak nonlinearity on the RHS of equation (1.61). We introduce new variables to indicate the slow modification by the weak nonlinearity and non uniformity gravity, and change the running frame of reference as:

$$\xi = r - C_s t, \quad R = \varepsilon r, \quad (1.62)$$

where $\varepsilon \ll 1$ is a small parameter at the same order as ρ/ρ_0 . Choosing the negative sign in front of the term with C_s , we restrict our attention to the waves propagating outwards in the radial direction. In the new frame of reference, the derivatives are

$$\frac{\partial}{\partial r} = \varepsilon \frac{\partial}{\partial R} + \frac{\partial}{\partial \xi}, \quad \frac{\partial}{\partial t} = -C_s \frac{\partial}{\partial \xi}. \quad (1.63)$$

In the new frame of reference by neglecting smaller terms in equations (1.57), (1.59), and (1.60) we obtain:

$$v_r = \frac{C_s}{\rho_0} \rho, \quad N_1 = 0, \quad N_2 = -\frac{C_s}{\rho_0} \frac{\partial \rho^2}{\partial \xi}. \quad (1.64)$$

Writing the nonlinear wave equation (1.61) in the new frame of reference, and substituting expressions (1.64) we obtain:

$$\frac{\partial \rho}{\partial R} + \left[\frac{1}{R} + \frac{Rg}{2C_s^2} \right] \rho + \frac{\rho}{R\rho_0} \frac{\partial \rho}{\partial \xi} = 0, \quad (1.65)$$

we see in equation (1.65) that ρ depends on R , meaning that the perturbation evolves with height. That is a simple wave equation in the spherically stratified medium. To find the solution to equation (1.65) we first make the parameters dimensionless by:

$$\xi' = \frac{\xi}{R_\odot}, \quad R' = \frac{R}{R_\odot}, \quad \rho' = \frac{\rho}{\rho_{00}}, \quad H' = \frac{H}{R_\odot}, \quad \rho'_0 = \frac{\rho_0}{\rho_{00}}, \quad (1.66)$$

and get:

$$\frac{\partial \rho}{\partial R} + \left(\frac{1}{R} + \frac{1}{2HR^2} \right) \rho + \frac{\rho}{R\rho_0} \frac{\partial \rho}{\partial \xi} = 0. \quad (1.67)$$

For simplicity we have omitted the prime. If we neglect the third term in the left hand side of equation (1.67), the solution would be:

$$\rho = \frac{\rho(R=1)}{R} \exp \left[-\frac{1}{2H} \left(1 - \frac{1}{R} \right) \right]. \quad (1.68)$$

Expression (1.68) shows that the amplitude of the density perturbation decreases with altitude, the same as expression (1.55) which is for the simple wave. Note that in case of $\lambda \ll H$ and taking small amplitude oscillations the solution for equation (1.67) would be harmonic in the form

$$\rho = \frac{\rho(R=1)}{R} \exp \left[-\frac{1}{2H} \left(1 - \frac{1}{R} \right) \right] \exp(ik\xi), \quad (1.69)$$

where k is the dimensionless wavenumber. Ofman et al. [2000] taking into account the effects of compressive viscosity showed that for different initial wave amplitudes, the relative amplitude $\rho(1)/\rho_0(1)$ increases from unity and reaches a maximum value before it decreases. Smaller initial amplitudes reach their maximum value further away from the Sun, for example the maximum value for the initial wave amplitude about 0.02 increases with height until 1.2 solar radii, but then starts to decrease.

1.6 Observational evidence of MHD waves in the solar atmosphere

It has been made clear by various observations and theoretical models that MHD waves play an important role in the physics of the solar corona. MHD waves of different kinds have been detected in the solar corona with high spatial and temporal resolution in structures like loops, plumes, spicules, filaments, jets, etc., by both imaging and spectral devices onboard satellites and on ground which are summarised in this Chapter.

There are several important reasons for the intensive study of MHD waves in the corona. It is connected with the possible role the waves play in the enigmatic problems of solar physics such as coronal heating, solar wind acceleration and flaring energy release, and also because of the possibility of the plasma diagnostics, provided by waves as natural probes of coronal plasmas.

Roberts et al. [1984] proposed the possibility that MHD waves may be good candidates for coronal seismology (diagnostics of the physical parameters of solar coronal plasmas by means of MHD waves). They showed that MHD oscillations take place in coronal structures for example a coronal loop, and stated that sausage waves of solar coronal plasma structures are similar to Perkins waves in oceanography and kink waves are similar to Love waves in seismology. Thus, studying these waves is a reliable approach on understanding the corona, since the radio band pulsations observed could be due to fast magnetoacoustic oscillations.

Possible mechanisms of coronal heating are put into two categories, AC and DC. AC mechanisms include Alfvén wave phase mixing and magnetoacoustic wave resonant absorption and DC mechanisms includes magnetic reconnection. The key ingredient of both phase mixing and resonant absorption is the creation of small transverse scales, which are subject to enhanced dissipation by viscosity or resistivity (e.g. Walsh and Ireland [2003], Nakariakov and Verwichte [2005], e.g. Priest and Forbes [2000]). Both mechanisms are being widely studied by scientists all over the world to finally give exact answers to the solar coronal heating problem, but the problem still remains open.

Possible mechanisms for acceleration of the solar wind plasma by MHD waves are reviewed in e.g. Ofman [2004] and Cranmer [2009]. These mechanisms include nonlinear cascade of wave energy to shorter scales, gyroresonances with minor species, and nonlinearly induced upflows. Both comprehensive numerical simulations and state-

of-art low-dimensional analytical models are present in the literature, e.g. Cranmer and van Ballegoijen [2005], Ofman [2010]. For example, in a model proposed by Suzuki [2008], using a one dimensional MHD model it was suggested that the solar wind acceleration could be due to the dissipation of low-frequency nonlinear Alfvén waves. However, there is still no clear evidence of the operation of those mechanisms in coronal plasmas. Also observational knowledge of MHD waves in the regions of the solar wind acceleration (1-3 solar radii) as well as in other coronal plasma structures is fragmented and inconclusive, despite recent progress in the field. These waves are studied in Chapter 4

In the next subsections we summarise the observational evidence of coronal MHD waves.

1.6.1 Transverse oscillations

The kink ($m = 1$, see Section 1.4) mode, is one of the main four MHD modes. This mode is transverse and shows itself, for example, in a coronal loop as periodic displacements of the loop axis across the field of view. This mode is weakly compressible. In a coronal loop, this mode can form a standing pattern. The fundamental (or global) mode of a loop has the maximum displacement at the top of the loop and zero perturbations at the loop foot points. The period of the global (or fundamental) standing kink mode which is the longest period of this mode is obtained by:

$$P = \frac{2L}{C_k}, \quad (1.70)$$

where L is the loop length and C_k (see equation (1.50)) is the kink speed introduced in Roberts et al. [1984].

Transverse waves had been known to exist in the solar atmosphere for years. The first periodic Doppler shift of coronal emission lines, most likely caused by the periodic variation of the line of sight velocity of the plasma, was observed by Koutchmy et al. [1983]. Their observations showed Doppler velocity oscillations for short period coronal waves without any noticeable intensity fluctuations. The periods of the waves were found about 43 s, 80 s, and 300 s, and were initially interpreted as resonant Alfvén waves. Roberts et al. [1984] demonstrated that these observations are associated with the standing kink modes.

Recently, this discussion was continued by Van Doorselaere et al. [2008b] in the context of observations of transverse waves detected by Tomczyk et al. [2007], De

Pontieu et al. [2007], and Okamoto et al. [2007]. It was argued by Van Doorselaere et al. [2008b] that the observations have to be interpreted in terms of fast magnetoacoustic kink waves and not the Alfvén wave.

Continuing this discussion Van Doorselaere et al. [2008a] performed a numerical simulation to model the time evolution of a velocity pulse transverse to the magnetic field, in both a homogeneous medium and a medium with transverse density structuring. This was done to compare the numerical results with the observations of transverse waves by Tomczyk et al. [2007], who detected coronal waves with phase speeds between 1000 km/s and 4000 km/s, and periods of about 300 s with the Coronal Multi-Channel Polarimeter (CoMP). Van Doorselaere et al. [2008a] showed, that in case of a homogeneous medium, the transverse velocity perturbation localised in the transverse direction propagates perpendicular to the magnetic field, which means that the wave has no energy flux along the magnetic field and can not produce the observed pattern. On the other hand in a structured medium, there exists propagation of transverse waves along the magnetic field. These are fast magnetoacoustic kink waves which have been described by Edwin and Roberts [1983] and in section 1.4.

The first spatially resolved transverse oscillations, which are standing kink waves, were observed almost simultaneously by Aschwanden et al. [1999] and Nakariakov et al. [1999], studying the 14 July 1998 coronal loop event. These waves which were interpreted as standing kink oscillations were observed with the EUV imager onboard the Transition Region and Coronal Explorer (TRACE). These oscillations were generated by a flare and dissipated very quickly after a few periods.

Aschwanden et al. [1999] studied oscillations of five loops with a distance between 60 Mm and 70 Mm from the epicentre of the flare, with an average length of $130,000 \pm 30,000$ km, a transverse displacement amplitude of about 4100 ± 1300 km, and a period of about 280 ± 30 s. Since this period is very close to the period of the fast kink mode found analytically for coronal conditions, namely 205 s, they interpreted these oscillations as fast magnetoacoustic kink modes.

Nakariakov et al. [1999] studied oscillations of another loop, with a foot point distance of about $(83 \pm 4) \times 10^6$ m, the displacement amplitude of 2030 ± 580 km, a frequency of 3.90 ± 0.13 mHz, and a decay time of about 12.1 ± 6.7 min. In these conditions the period of oscillations was estimated 256 s and the arc length of the loop would be about $(130 \pm 6) \times 10^6$ m. Then the phase speed of the waves was

calculated,

$$\frac{\omega}{k} = \frac{2L}{P} \approx 1020 \pm 132 \text{ kms}^{-1}. \quad (1.71)$$

Since this value is close to the expected phase speed of the fast kink mode, these oscillations were interpreted as the fast magnetoacoustic kink mode.

Williams et al. [2001] observed short period MHD waves with periods about 6 s (frequencies about 0.16 Hz), while studying coronal loops in the 1999 eclipse event with the Solar Eclipse Coronal Eclipse Imaging System (SECIS) instrument. The phase speed of the waves was about 2,000 km/s observed as propagating intensity. Cooper et al. [2003] showed that the observed variation in the emission intensity was consistent with the modulation of the observed column depth of the loop by a kink wave due to a line-of-sight integration effect.

Propagating transverse waves were also observed in flaring supra-arcade regions by Verwichte et al. [2005] with TRACE. The observed periods were about 90-220 s. The observed apparent phase speeds were several hundred km/s, decreasing with height. These waves are interpreted as propagating, fast magnetoacoustic kink waves guided by a plasma structure. Propagating kink waves have been recently observed in other coronal structures such as coronal jets which will be discussed and modelled in full detail in Chapter 2. Note that the presence of kink waves is only possible in case of transverse structuring of the medium or in other words having a wave guide.

1.6.2 Sausage oscillations

The sausage mode ($m = 0$) is compressible and shows itself as periodic symmetric changes in the cross section of a structure, for example a loop or a jet. The period of the global sausage mode of a coronal loop is estimated as

$$P_{sausage} = \frac{2L}{C_p}, \quad (1.72)$$

where C_p is the phase speed of the global sausage mode with wave number $k_z = \pi/L$, which is between the internal and external Alfvén speeds. Note that as stated by Edwin and Roberts [1983] the global sausage mode reaches a cutoff value as k decreases, meaning that for the existence of a trapped global sausage mode the loop length must be smaller than π/k_{cutoff} not to violate the $k > k_{\text{cutoff}}$, where k_{cutoff} is a certain cutoff value determined by physical conditions in the plasma cylinder, see Figure 1.5. The 14 – 17 s oscillations observed by the Nobeyama Radioheliograph

were studied by Nakariakov et al. [2003] and interpreted as the global sausage mode. Inglis et al. [2009] studied the sausage oscillations of coronal loops and proved that the cutoff frequency is almost independent of the values of the internal and external plasma- β . Srivastava et al. [2008] detected oscillations in chromospheric loops with periods about 587 s near the loop apex, and 349 s near the loop foot-points and referred these oscillations to the global and second harmonic sausage oscillations, respectively.

1.6.3 Longitudinal oscillations

Two types of longitudinal waves have been observed in the solar atmosphere. These waves are compressible, and are seen to be either standing or propagating. The slow magnetoacoustic waves which are propagating longitudinal waves are sometimes called acoustic, since their speed is close to the sound speed. In Figure 1.3, the propagation of this mode has been shown to be parallel to the magnetic field in a homogeneous medium. In a plasma cylinder, this mode propagates at a speed a bit lower than the sound speed see Figure 1.5. This mode is predominantly longitudinal. This means that the longitudinal mode does not affect the transverse components of the velocity and only perturb the parallel component of the velocity. Also it perturbs the density and hence is essentially compressible.

The period of the global slow magnetoacoustic mode of a coronal loop is

$$P_{slow} = \frac{2L}{C_{T0}}, \quad (1.73)$$

where $C_{T0} = C_s C_A / (C_s^2 + C_A^2)^{1/2}$ is the tube speed inside loop which in a low- β corona is very close to the sound speed inside the loop.

Strongly damped standing Doppler shift oscillations in coronal loops with temperatures above 10^6 K were observed by Wang et al. [2002] with SoHO/SUMER. The periods were between 14 and 18 min and the decay time between 12 and 19 min, with average amplitude speeds about 77 km/s. These oscillations were modelled by Ofman and Wang [2002] with a 1D numerical model using typical observed parameters and taking into account the thermal conduction, obtained the period and the fast decay time in the range of the observations and interpreted these oscillations as standing slow magnetoacoustic waves.

Wang et al. [2003a] studied this phenomenon statistically, using both the Doppler shift velocity and intensity observations. The average oscillation period for the in-

tensity was about 17 min with a decay time about 21 min, but for the Doppler velocity the period was 17 min with decay time of about 37 min. They deduced that, since the observed oscillations for the Doppler velocity and the intensity were the same but with a quarter of a period phase difference, these oscillations coincide with the analytical prediction of the standing slow magnetoacoustic waves. Moreover, the analytical value for the period of the standing waves for typical loop parameters made by Roberts et al. [1984] was consistent with the observations. In a more detailed study Wang et al. [2003b] found the periods of these oscillations to be between 7 and 31 min, with decay times between 5.7 and 36.8 min, and the average amplitude velocity about 200 km/s. The phase speed of these oscillations was consistent with the sound speed 370 km/s for temperatures about 6 MK.

Numerical modelling of this phenomenon performed by Nakariakov et al. [2004b] concluded that quasi periodic pulsations with periods between 10 s and 300 s observed in the radio, visible, and X-ray bands could be created by the second harmonic of the standing slow magnetoacoustic wave.

In addition to standing magnetoacoustic slow waves, propagating magnetoacoustic slow waves were also detected in the solar atmosphere. De Moortel et al. [2002] performed a comprehensive review of physical properties of these waves observed near foot-points of large coronal loops of propagating speeds from 80 km/s to 160 km/s with variations of intensity about 4.1 ± 1.5 percent of the background loop brightness. Similarly to the standing waves propagating waves were observed to be very strongly damped with periods between 281 s and 283 s. Propagating slow magnetoacoustic waves are regular events in large coronal loops (e.g. de Moortel [2009]).

Nakariakov et al. [2000c] proposed a theoretical one dimensional model of propagating longitudinal waves in a coronal loop taking into account the density stratification, the effects of thermal conductivity along the magnetic field and viscosity. They obtained an evolutionary equation being able to deduce that the waves with periods between 5 and 15 minutes experience amplitude growth as they propagate up the loop and after reaching a maximum amplitude, they quickly dissipate which was consistent with observations (not seeing downward propagation).

Studying propagating slow waves is important because these waves travel at the speed close to the sound speed, which is related to the local plasma temperature. Thus, they provide us with a tool for the diagnostics of the thermal structure. Also, as these waves propagate predominantly along the field their observations allow one

to determine the magnetic field directivity.

1.6.4 Attempts to observe torsional oscillations

Torsional waves propagate along field-aligned plasma structures (e.g. loops, filaments or jets) at the local Alfvén speed and manifest themselves as twisting of the structure. These waves could not be detected by coronal imagers in an initially untwisted loop because of the incompressible nature of these waves, but may be detected with spectrometers. In a coronal loop, the resonant period of the global torsional mode is:

$$P_{torsional} = \frac{2L}{C_{A0}}. \quad (1.74)$$

If the Alfvén speed is non-uniform across the magnetic field, different magnetic surfaces oscillate with different periods. This leads to the creation of steep gradients across the field, which grow with time. This effect dramatically increases the wave dissipation by viscosity, and is known as phase mixing Heyvaerts and Priest [1983]. Recently, Jess et al. [2009] claimed to have observed torsional waves in the lower solar atmosphere, but it is unclear whether alternative interpretations due to the complicated nature of the observed spectral line are excluded. They detected oscillations in a 430,000 square km area located near the centre of the solar disk. The waves observed by Jess et al. [2009] have periods between 126 s and 700 s, and amplitude velocities about 2.6 km/s which are coupled with the chromospheric line of sight Doppler velocities about 23 km/s. They claim, since there is neither any co-spatial intensity variations which is a possible feature of sausage oscillations, nor transverse displacements which is a feature of kink oscillations, magnetoacoustic waves are not the case, meaning this could be an Alfvén torsional wave. However, the interpretation in terms of a sausage wave can not be ruled out too, in this mode the decrease in the density is accompanied by the increase in the loop radius, and their product responsible for the line intensity can be nearly constant.

Banerjee et al. [2009] studying polar coronal holes observed non-thermal broadening and since the velocity broadening was inversely proportional to the square root of the electron density they deduced it is associated to Alfvén waves. The increasing attention and applications of the torsional modes in the solar atmosphere's active regions made two Chapters of this work be dedicated to torsional modes of coronal structures. The properties and concepts of linear torsional waves are discussed in Chapter 3 and nonlinearly induced flows by the torsional waves are studied in

1.6.5 Anomalous resistivity and magnetic reconnection

Magnetic reconnection is a hot topic in both solar and space plasmas and laboratory plasmas. This phenomenon can cause release of energy, liberating the energy stored in the magnetic field and converting it into the internal energy of the plasma, and the kinetic energy of bulk flows (e.g., jets), various waves and nonthermal particles [Priest and Forbes, 2000]. In section 1.2 it was mentioned that ideal MHD leads to frozen-in condition, which takes place in a highly conductive regime. Finite magnetic diffusivity violates the frozen-in condition, allowing for topological changes in the magnetic configuration and hence the possibility of evolution of the plasma system to a state with lower potential energy. In the solar coronal context, the released energy can lead to plasma heating, generation of jets, flares and coronal mass ejections (CME).

The classical value of the plasma resistivity of the solar corona is very small, just $10^{-4} \Omega\text{m}$ (e.g. Boyd and Sanderson [2003]). It is very difficult to explain a number of observed phenomena, e.g. flares, without the use of the concept of anomalously high resistivity. For the violation of the frozen-in condition, enhancement of resistivity by several orders of magnitude, at least at some specific locations and during some time intervals, is required. This could be achieved by electric current driven anomalous resistivity. For example, the concept of enhanced, in comparison with the classical value, resistivity, is often employed in massive numerical simulations of flaring energy releases in the form of a piece-wise current-dependent function,

$$\eta(x, t) = \begin{cases} 0, & \text{if } |v_D| \leq v_{cr} \\ \eta_{anomalous}, & \text{if } |v_D| > v_{cr} \end{cases}, \quad (1.75)$$

see Ugai [2001]. For example $\eta_{anomalous}$ could be taken as

$$\eta_{anomalous} \propto \frac{v_D(x, t) - v_{cr}}{v_D(0)}, \quad (1.76)$$

where v_D and v_{cr} are the drift and threshold velocity, respectively, see Kliem et al. [2000]. The anomalous resistivity in this piece-wise form is often used in numerical simulations of solar coronal dynamics (e.g. Nishida et al. [2009]). In those numerical simulations, the current-dependent resistivity was necessary for the initial trigger-

ing of magnetic reconnection, and for the interpretation of preferable locations of reconnecting current sheets.

Anomalous resistivity is a feature of collisionless plasmas; where the instabilities and turbulence create electromagnetic field perturbations causing wave-particle interactions, resulting in the increase in electric current which causes anomalous resistivity. In MHD, the sudden increase in the resistivity when the current density exceeds a certain threshold cannot be explained. However, this effect is well known in plasma physics, the stages of this phenomenon are as follows; first the electric current density must exceed the threshold; second, this causes plasma instability (e.g. ion-acoustic instability, streaming instability, ion-cyclotron instability) which leads to the onset of micro-turbulence, which dramatically enhances the plasma transport coefficients in the region of the high electric current density [Büchner and Elkina, 2005]. Thus, essentially, the effect of anomalous resistivity is described in terms of wave-particle interaction with the use of the Vlasov equation, usually solved numerically. For example, the enhanced resistivity generated by current-driven ion-acoustic waves was numerically studied by Watt et al. [2002] and Petkaki et al. [2003], who showed the increase in the resistivity by several orders of magnitude in a time scale about a few hundred electron plasma periods. As the period of plasma oscillations in MHD is infinitely small, the onset of the anomalous resistivity occurs practically instantly on the MHD time scales.

In a further study Büchner and Elkina [2006] and Büchner [2007], extended the previous studies with more realistic boundary conditions and concluded that if only currents are concentrated in thin sheets, anomalous resistivity caused by wave-particle interaction is a candidate for coronal reconnection. Still this phenomenon is not yet fully understood, since 2D and 3D simulations need to be carried out e.g. Büchner [2007].

Nakariakov et al. [2006] proposed a model where an externally generated fast magnetoacoustic wave, causes variations of current, seeding anomalous resistivity in the vicinity of a potential site for magnetic reconnection. This model will be discussed in subsection 1.6.6 in the context of quasi period pulsations. Also, this effect is interesting in the context of sympathetic flare phenomenon. The ejected fast magnetoacoustic wave from one flare could somehow trigger the magnetic reconnection at another site and hence trigger another solar flare.

A possible evidence of the phenomenon of sympathetic flares was presented by Moon et al. [2002], who studied “chains” of flares occurring at different, spatially separated

locations, and found that there are pairs of flares which occur almost simultaneously. Flares are violent releases of energy, and hence can generate a propagating perturbation that can trigger another flare. A possible scenario could be as follows: the first, “mother”, flare generates a fast magnetoacoustic wave, which approaches a region where the magnetic field configuration is about to reconnect, and seeds there anomalous resistivity. It can trigger the “daughter” flare. In Chapter 5, we study the interaction of a fast wave pulse with a magnetic null-point and determine the position where the current density spikes, which can generate anomalous resistivity, for different initial parameters of the pulse.

1.6.6 Quasi-periodic pulsations in solar flares

Another common example of oscillating processes in the corona is quasi periodic pulsations (QPP) in the emission generated in solar flares. Quasi-periodic pulsations have been detected in the solar atmosphere from radio to the γ -ray band with various periods ranging from a fraction of a second to a few minutes [Nakariakov and Melnikov, 2009]. For example, Svestka et al. [1982], while studying the two-ribbon flare on November 1980, detected QPP in the active region below the arch of the flare in the X-ray band with the hard X-ray imaging spectrometer on board the Solar Maximum Mission (SMM). The period of the observed pulsations, about 1200 s, was one of the longest, reported in solar literature. Harrison [1987] studied pulsations observed by SMM in the foot-point of a loop with periods about 1440 s in the soft X-ray band and concluded the pulsations are possibility due to MHD wave oscillations. Svestka [1994] also suggested that the quasi-periodic X-ray brightening observed in a large-scale loop with periods about 1200 s may be caused by MHD oscillations. There is also abundant evidence of short period (less than 1 s) and medium period (from 1 s to a few minutes) oscillations in flares. For example, Nakariakov et al. [2003] observed 13-17 s QPPs with Nobeyama Radioheliograph. Kai and Takayanagi [1973] with the interferometer of the Nobeyama solar radio station while studying the 5th November 1970 complex outburst, observed smaller than 1 s periods. For a detailed table of observed QPPs, see Aschwanden [2005]. The main current question connected with quasi-periodic pulsations is understanding the physical mechanism responsible for their generation with a specific period. According to Nakariakov and Melnikov [2009] there could be two groups of mechanisms responsible for the generation of long quasi period oscillations: MHD oscillations and load/unload mechanisms. MHD oscillations could either affect the energy

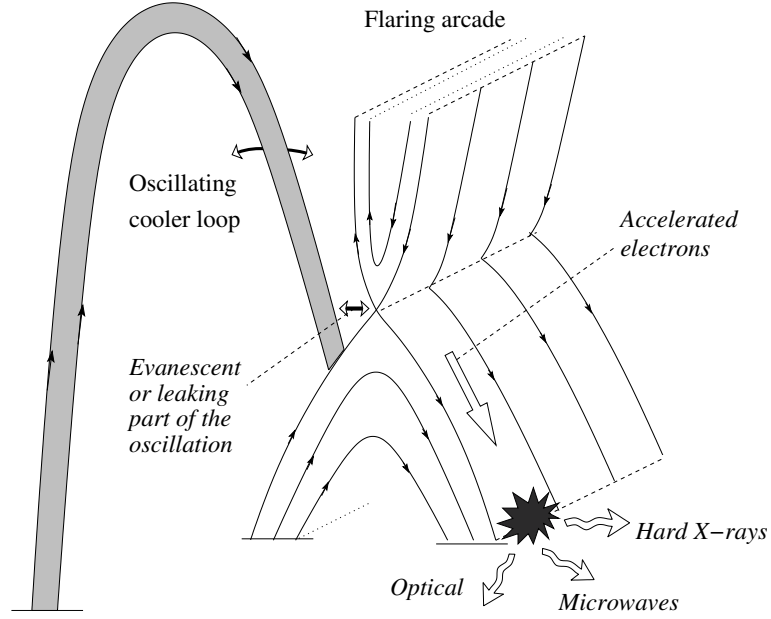


Figure 1.6: Sketch of a possible mechanism for the generation of quasi-periodic pulsations by MHD oscillations in a neighbouring plasma structure (Nakariakov et al. [2006]). The leaking MHD waves from the oscillating cooler loop interact with the current sheet above the X-point of a nearby arcade causing periodic variations of the electric current density, triggering magnetic reconnection, resulting in quasi periodic pulsations in radio, visible, and X-ray bands.

release and electron acceleration in the flaring site coming from external oscillations [Foullon et al., 2005] or by modes inside the emitting flare itself [Asai et al., 2001]. Load/unload mechanisms include oscillatory magnetic reconnection [Kliem et al., 2000; Murray et al., 2009] or thermal over-stability [Kuin and Martens, 1982; Müller et al., 2004].

Nakariakov et al. [2006] proposed a model in which QPP were generated by a non-flaring loop oscillating either with the fast kink or sausage mode, situated in the neighbourhood of a flaring arcade. If by any chance a leaky wave from the cooler loop could interact with the X-point above the flaring arcade (or a current sheet), the interaction would cause periodic variations in the electric current density, which creates instabilities that causes anomalous resistivity (see subsection 1.6.5) being able to trigger magnetic reconnection. This results in quasi periodic pulsations in radio, visible, and X-ray bands.

To understand the type of MHD wave which is responsible for the QPP, spatially

resolved observations are a need. The first imaging observation of quasi periodic pulsations was analysed by Asai et al. [2001] with the Nobeyama Radioheliograph and the Yohkoh soft and hard X-ray telescopes while studying the C7.9 flare on 10th, November 1998. The pulsations were observed in the X-ray and microwave bands and since the Alfvén transit time along the loop was found almost equal to the period of the QPP they deduced that oscillations of coronal loops affect the efficiency of particle injection and acceleration.

1.6.7 Observations of plasma jets in the corona

An important element of the magnetic reconnection theory are fast plasma jets (about the Alfvén speed) which are generated at the reconnection site. The search for such jets aims to prove the basic theories of coronal plasma heating by reconnection, and hence attracts great attention. The typical speeds of the jets, predicted by MHD theories, are about the Alfvén speed. Recently, the X-ray Telescope on-board Hinode (Hinode/XRT) made a great progress in studying high temperature coronal events specially coronal jets [Golub et al., 2007]. Hinode/XRT revealed the appearance of up to 10 jets per hour in the corona [Cirtain et al., 2007] with an average temperature of about 6 MK. Such a frequency of appearance is an order of magnitude greater than determined with previously available X-ray imagers, e.g. Yohkoh/SXT.. The typical lifetime of jets was found to be about between 100 s and 2500 s. This is consistent with the results obtained for the lifetime of jets with SXT. The size of the X-ray jets are in the range 2×10^3 km and 2×10^4 km in width and 1×10^5 km in length. The speeds of the outflows which were estimated to be in the range from 200 to 800 km/s, and the number of detected jets made [Cirtain et al., 2007] deduce that this could be a contribution to solar wind acceleration. A detailed forward modelling of waves in the X-ray jets observed by Cirtain et al. [2007] is presented in Chapters 2 and 3.

1.7 Present solar missions

In order to study various events taking place on the Sun and also performing measurements on various physical parameters of the events on the Sun, in addition to successful ground-based instruments like e.g. Nobeyama Radioheliograph, and the Coronal Multi-channel Polarimeter (CoMP), space missions are crucial. Spaceborne instruments provide us with the continuous, usually uninterrupted flux of

data, which is free of atmospheric effects (while can be affected by the Earth's radiation belts). But, more importantly, space-borne observational facilities can use observational bands, which are not available from ground, e.g. EUV, X-ray and gamma-ray. Here the aims and abilities of some current effective solar missions are mentioned.

The Solar and Heliospheric Observatory (SoHO) was launched on December 2, 1995 as a joint mission between the European Space Agency (ESA) and NASA, aiming to study all the regions of the Sun from core to outer atmosphere which helps understand the origin of the solar outbursts and wind. Note that SoHO is not a satellite, since it does not orbit the Earth, instead it is placed at the neutral gravity point between the Sun and Earth, the Lagrangian 1 point.

There are twelve instruments onboard SoHO: the Coronal Diagnostic Spectrometer (CDS); the Charge, Element, and Isotope Analysis System (CELIAS); the Comprehensive Suprathermal and Energetic Particle analyser (COSTEP); the Extreme Ultraviolet Imaging Telescope (EIT); the Energetic and Relativistic Nuclei and Electron experiment (ERNE); the Global Oscillations at Low Frequencies (GOLF), the Large Angle and Spectrometric Coronagraph (LASCO); the Michelson Doppler Imager (MDI), the Solar Ultraviolet Measurements of Emitted Radiation (SUMER), the Solar Wind Anisotropies (SWAN), the Ultraviolet Coronagraph Spectrometer (UVCS), and the Variability of Solar Irradiance and Gravity Oscillations (VIRGO). The main part of the data is in the open access.

A few years after SoHO, the Transition Region and Coronal Explorer (TRACE) was launched in April 1998, aiming to study the solar photosphere, chromosphere, and corona in order to identify relations between the fine-scale magnetic fields and the associated plasma structures on the Sun. This aim would be achieved by studying the 3D magnetic field structure, the temporal evolution of the magnetic field due to photospheric flows, and studying the thermal topological effects on the magnetic field. Note that the spatial resolution of images observed by TRACE is very high, about 1 arc second, with the pixel size being 0.5 arc second, which corresponds to the spatial size of about 318 km on the solar disk.

Another small but also effective mission is the Reuven Ramaty High Energy Solar Spectroscopic Imager (RHESSI) which was launched in February 2002 aiming to study the solar flares in the context of particle propagation and acceleration, explosive energy releases, and coronal heating. Its temporal resolution is 4 seconds having an energy range between 3 keV and 17 MeV.

Another revolutionary mission is the Solar Terrestrial Relations Observatory (STEREO) which was launched in October 2006 to study the Sun-Earth system. This mission, aiming to study the flow erupted from the Sun which envelopes the Earth, involves two twin satellites one travelling ahead of the Earth around the Sun (STEREO A), and the other travelling behind the Earth, orbiting the Sun in a direction opposite to Earth's (STEREO B). Combination of the images obtained with STEREO A and B with images obtained from the Earth satellites or the L1 point allow one to reconstruct 3D images of the heliosphere. In particular, 3D images from the mass eruptions of the Sun give us clues for their triggering. There are four instruments on board STEREO: the Sun Earth Connection Coronal and Heliospheric Investigation (SECCHI), which itself contains of a EUV imager, 2 white-light chronographs, and a heliospheric imager, SWAVES which is a radio wave tracker, IMPACT which does 3D measurements of plasma characteristics of solar energetic particles and local magnetic field, and PLASTIC which provides plasma characteristics of protons, alpha particles and heavy ions.

Hinode (Solar-B) launched in September 2006, is a Japanese funded mission having United States and United Kingdom as collaborators. The aim of Hinode is to understand the solar activity by studying the Sun's magnetic field. Hinode carries three instruments, the Solar Optical Telescope (SOT), The X-ray telescope (XRT), and the Extreme Ultraviolet Imaging Spectrometer (EIS). XRT is able to capture X-ray images of the outer solar atmosphere which has temperatures above 1 million K. XRT provides coronal images at different temperatures, both full disk and partial disk of view. There are 10 filters which can be used on XRT, this provides excellent temperature coverage, which ranges as $6.1 < \log T < 7.5$. The temperature discrimination of XRT is $\log T = 0.2$ and the angular resolution is 2 arc second, also it has a field of view for a full disk greater than 30 arc min.

The combination of observations by SOT and XRT on board Hinode, give the ability to study how the erupted solar events are triggered by the changes of the solar magnetic field. EIS onboard Hinode is able to measure the flow speeds and density changes in the chromosphere-corona transition region, meaning that it could somehow find relations between the photosphere and the corona.

A recent mission to study the solar atmosphere and specially solar flares was the complex orbital observations near-Earth of activity of the Sun, Coronas Photon. It was a Russian mission with collaborations from Ukraine and India launched in January 2009 and stopped on November 2009. The main aim of this mission was

to understand the energy transport by accelerated particles during solar flares. In addition this mission had astrophysical and solar-terrestrial aims too. On board Coronas Photon there was a solar telescope/imaging spectrometer (TESIS) which monitored the solar activity in the X-ray band with temporal resolution of 1 second and spatial resolution about 1 arc sec with a field of view about 45 arc min (full disk).

The most recent solar mission is the Solar Dynamic Observatory (SDO) which was launched on February 2010. Its aims are to help understand the magnetic field generation and structuring of the Sun, and also help understand the solar activity which accelerates the solar wind and effects the space weather. There are three instruments onboard SDO, the Atmospheric Imaging Assembly (AIA) which gives images in ten wave lengths every 10 seconds, making full-Sun images of 4096x4096 pixels, with the pixel size of 0.6 arc seconds, the Extreme Ultraviolet Variability experiment (EVE), and the Helioseismic and Magnetic Imager (HMI) which provides a full disk coverage of the Sun. Note that the image resolution of SDO/AIA is twice the resolution of STEREO and four times the resolution of SOHO. Also, in the fast cadence mode, SDO could take an image a second which is 180 times faster than STEREO and 720 times faster than SOHO, which is showing the advances of SDO compared to previous solar missions.

Chapter 2

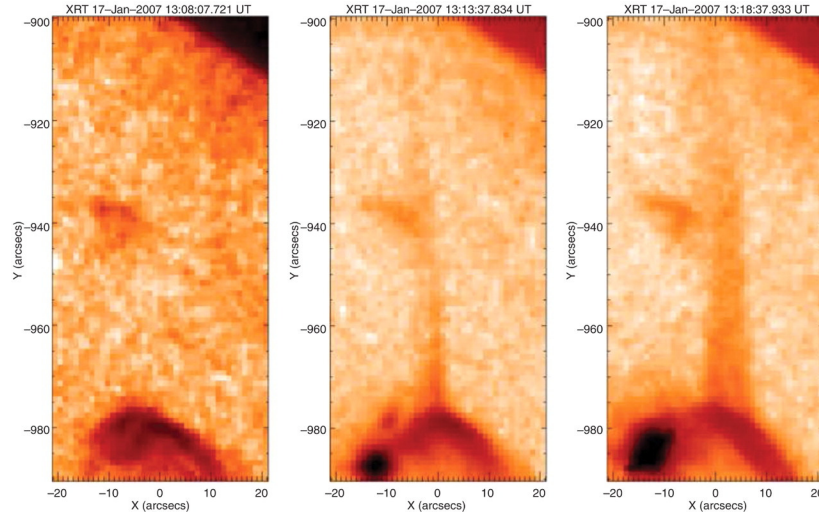
Propagating kink waves in soft X-ray coronal jets

The work in this Chapter is also published in Vasheghani Farahani et al. [2009].

2.1 Introduction

Hot jets are often observed in the solar corona in the soft X-ray band as transient, collimated features with apparent high-velocity outflows in the direction of collimation [Shibata et al., 1992; Alexander and Fletcher, 1999]. Statistical analysis of jets observed with Yohkoh/SXT [e.g., Shimojo et al., 1996] revealed that most jets are associated with flaring energy releases, mainly small flares and microflares. The typical observed lengths of hot jets, defined as the distance from base to where its intensity drops below some certain value, are in the range of between a few tens and several hundred thousand km, and their diameters are one to two orders of magnitude smaller. The typical aspect ratio of length to width was measured to be about ten. The lifetime is typically in the range from several minutes to an hour. About half of the observed jets showed a constant width, and about a third had a width decreasing with height.

The observed flow speeds are several hundred km/s, reaching in some cases about a thousand km/s. The estimate of the speed is affected by the projection effect, and by the obvious difficulties connected with the measurement of a physical speed with an imaging instrument. The majority of jets are situated over regions of mixed polarity. Shibata et al. [1992] suggested that hot jets are associated with reconnection



J. W. Cirtain et al., Science 318, 1580 -1582 (2007)



Published by AAAS

Figure 2.1: Hinode XRT false-colour images of three stages of a jet's evolution [Cirtain et al., 2007]

outflows. Numerical MHD modelling [Yokoyama and Shibata, 1995] showed that an anemone jet could result from the interaction of an emerging magnetic flux with a vertical or oblique background magnetic field. Figure 2.1 shows three snapshots of an X-ray coronal jet observed by Hinode/XRT, the features and advantages of Hinode/XRT has been discussed in section 1.7.

The theoretical model of MHD waves guided by a plasma structure of steady flow was developed by Roberts [1987], Goossens et al. [1992] and Terra-Homem et al. [2003] for the cylindrical geometry and by Nakariakov and Roberts [1995a] for the slab geometry. The main new feature introduced by the flow was the modification of the dispersion relations and wave-flow interaction effects associated with negative energy [Joarder et al., 1997]. The latter can cause instabilities at steady flow speeds well below the KHI threshold, which occurs when the flow-speed shear exceeds the

Alfvén speed by a factor of about two [Ruderman et al., 1996].

Note that the concept of negative energy waves is related to the context of backward waves, Riutova [1988] showed that in the existence of fast flows, negative energy waves come into play. Cairns [1979] stated that negative energy waves could reduce the energy of the system if excited. Nakariakov and Roberts [1995a] and Nakariakov et al. [1996] made a clear study on backward waves for various modes in the solar atmosphere. They took into account the effect of internal and external flows and mentioned that, whenever the difference between the flows inside and outside a structure is more than the phase speed of a mode travelling in the opposite direction for the same wave number without a flow, backward waves are of negative energy [Riutova, 1988]. Meaning, increase in the amplitude of the wave decreases the total energy of the steady flow and wave. In other words dissipation could cause over-stability [Joarder et al., 1997].

In this Chapter we adapt the theoretical model for MHD waves guided by a plasma cylinder with a steady flow in interpreting the transverse waves observed by Cirtain et al. [2007] in soft X-ray coronal jets. Cirtain et al. [2007] observed and studied the fine structure of the jets, revealing the presence of transverse (kink) oscillations, which were periodic displacements in the jet axis with a period of about 200 s and a displacement amplitude of about 4000 km. The latter value is half of the given value for the peak-to-peak magnitude. The question arises about the nature of these waves.

The aim in this Chapter is to answer this question by forward modelling of transverse oscillations of a soft X-ray jet directed from an off-limb coronal loop seen by Hinode/XRT. We do not consider the jet formation or collimation, but restrict ourselves to the analysis of linear MHD perturbations of the observed plasma configuration. We demonstrate by expansions of the dispersion relation in the long wave-length limit that the observed properties of waves are consistent with guided, fast magnetoacoustic, kink waves. The basic concepts and properties and observations of kink waves were discussed in section 1.4 and subsection 1.6.1.

2.2 Model and equilibrium conditions

We consider a hot jet as a uniform cylinder of radius a which was discussed in section 1.4 with the equilibrium, internal, magnetic field $B_0\hat{\mathbf{z}}$ parallel to the axis of the jet. Outside the cylinder, the magnetic field is $B_e\hat{\mathbf{z}}$. The gas pressure and density within

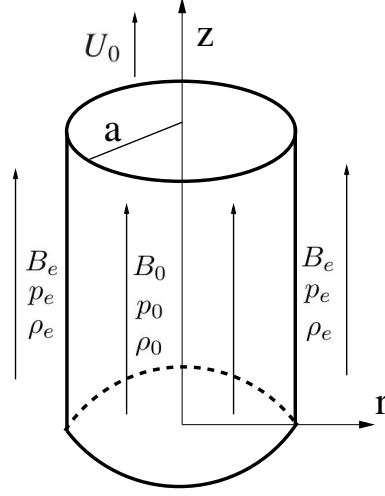


Figure 2.2: The sketch of a magnetised cylindrical flux tube with radius a , density ρ_0 , and gas pressure p_0 with a flow U_0 parallel to the z axis, embedded in a magnetised medium with density ρ_e and gas pressure p_e . Both magnetic fields inside and outside the tube are parallel to the z -direction.

the cylinder are p_0 and ρ_0 , respectively, and outside the cylinder, they are p_e and ρ_e , respectively.

Total pressure balance implies that,

$$p_0 + B_0^2/2\mu = p_e + B_e^2/2\mu, \quad (2.1)$$

where μ is the magnetic permeability. Hence, the densities ρ_0 and ρ_e are related by

$$\frac{\rho_e}{\rho_0} = \frac{2C_{s0}^2 + \gamma C_{A0}^2}{2C_{se}^2 + \gamma C_{Ae}^2}, \quad (2.2)$$

with

$$C_{s0} = (\gamma p_0/\rho_0)^{1/2}, \quad C_{A0} = B_0/\sqrt{\mu\rho_0} \quad (2.3)$$

and

$$C_{se} = (\gamma p_e/\rho_e)^{1/2}, \quad C_{Ae} = B_e/\sqrt{\mu\rho_e} \quad (2.4)$$

where C_{s0} , C_{se} are the sound speeds inside and outside the cylinder, respectively. C_{A0} , C_{Ae} are the Alfvén speeds inside and outside the cylinder, respectively, and γ is the ratio of the specific heats.

Inside the cylinder, there is a field-aligned steady flow with $\vec{V} = U_0\hat{z}$. Outside the

jet, there is no steady flow, $U_e = 0$. In both regions, the plasma- β is taken to be below unity. So our MHD equations here are as mentioned in section 1.4 but with addition of terms with the equilibrium steady flow U_0 , which is not absent in this model.

2.3 Dispersion relations

We consider linear kink perturbations to the steady-flow equilibrium, of azimuthal wave number $m = 1$ because they are the only ones perturbing the jet axis. Following Goossens et al. [1992], the general dispersion relation linking the frequency ω to the longitudinal wave number k of an $m = 1$ mode is

$$\frac{\rho_0}{\rho_e} \frac{(k^2 C_{A0}^2 - \Omega_0^2)}{(k^2 C_{Ae}^2 - \omega^2)} \frac{m_e}{n_0} \frac{K_1'(m_e a)}{K_1(m_e a)} = \frac{J_1'(n_0 a)}{J_1(n_0 a)}, \quad (2.5)$$

where $\Omega_0 = \omega - U_0 k$ is the Doppler-shifted frequency,

$$n_0^2 = -\frac{(k^2 C_{s0}^2 - \Omega_0^2)(k^2 C_{A0}^2 - \Omega_0^2)}{(C_{s0}^2 + C_{A0}^2)(C_{T0}^2 k^2 - \Omega_0^2)}, \quad C_{T0}^2 = \frac{C_{s0}^2 C_{A0}^2}{C_{s0}^2 + C_{A0}^2}, \quad (2.6)$$

and

$$m_e^2 = \frac{(k^2 C_{se}^2 - \omega^2)(k^2 C_{Ae}^2 - \omega^2)}{(C_{se}^2 + C_{Ae}^2)(C_{Te}^2 k^2 - \omega^2)}, \quad C_{Te}^2 = \frac{C_{se}^2 C_{Ae}^2}{C_{se}^2 + C_{Ae}^2}. \quad (2.7)$$

where C_{T0} and C_{Te} are the inside and outside tube speeds, respectively. Equation (2.5) is a transcendental implicit algebraic equation that does not have exact analytical solutions. Since the wavelengths of transverse perturbations observed by Cirtain et al. [2007] are significantly longer than the radius a of the jet, it is sufficient to consider the limiting case of long wave-lengths $|k|a \ll 1$. From equation (2.5), the phase and group speeds can be approximated by the explicit expressions:

$$\omega/k \approx v_G + \alpha k^2 a^2 \ln(|k|a), \quad (2.8)$$

$$d\omega/dk \approx v_G + 3\alpha k^2 a^2 \ln(|k|a), \quad (2.9)$$

where

$$v_G = \frac{\rho_0 U_0}{\rho_0 + \rho_e} + v_{cm}, \quad (2.10)$$

$$\alpha = -\frac{1}{2} \frac{\rho_0(C_{A0}^2 - (v_G - U_0)^2)(C_{Ae}^2 - v_G^2)}{(\rho_0 + \rho_e) C_{Ae}^2 v_{cm}}, \quad (2.11)$$

$$v_{cm} = \sqrt{C_k^2 - \frac{\rho_0 \rho_e}{(\rho_0 + \rho_e)^2} U_0^2}, \quad C_k = \sqrt{\frac{\rho_0 C_{A0}^2 + \rho_e C_{Ae}^2}{\rho_0 + \rho_e}}. \quad (2.12)$$

For $k = 0$, equation (2.8) reduces to:

$$\omega/k \approx v_G, \quad (2.13)$$

which is the result found by Goossens et al. [1992]. For $U_0 = 0$, equation (2.8) becomes

$$\frac{\omega}{k} = C_k \left\{ 1 - \frac{\rho_0 \rho_e (C_{Ae}^2 - C_{A0}^2)(C_{Ae}^2 - C_k^2)}{2(\rho_0 + \rho_e)^2 C_{Ae}^2 C_k^2} k^2 a^2 K_0(|k|a) \right\}, \quad (2.14)$$

which coincides with the expression given in Edwin and Roberts [1983], but here instead of the modified second-order Bessel function, we use the logarithmic expression as its asymptotic equivalent,

$$\frac{\omega}{k} = C_k \left\{ 1 + \frac{\rho_0 \rho_e (C_{Ae}^2 - C_{A0}^2)(C_{Ae}^2 - C_k^2)}{2(\rho_0 + \rho_e)^2 C_{Ae}^2 C_k^2} k^2 a^2 \ln(|k|a) \right\}. \quad (2.15)$$

Using the observational fact that the jet is significantly denser than the background plasma [Culhane et al., 2007], $\rho_e/\rho_0 \ll 1$, we can further simplify equations (2.8)-(2.12) to

$$v_G \approx U_0 + C_{A0} \sqrt{1 + (B_e/B_0)^2}, \quad \alpha \approx \frac{C_{A0}}{2} \frac{(B_e/B_0)^2}{\sqrt{1 + (B_e/B_0)^2}}. \quad (2.16)$$

In Figure 2.3, the dependence of the phase and group speeds on the wave number is shown, which is calculated numerically with the use of the full dispersion relation of equation (2.5), and analytically with the use of asymptotic expressions in equations (2.8)-(2.12) and (2.16). All three approaches show satisfactory consistency. Both asymptotic expressions are independent of the sound speeds inside and outside the jet. This is consistent with the conclusion of Edwin and Roberts [1983] that the kink wave phase speed depends very weakly upon the value of the sound speed, provided $C_{s0} < C_{A0}$.

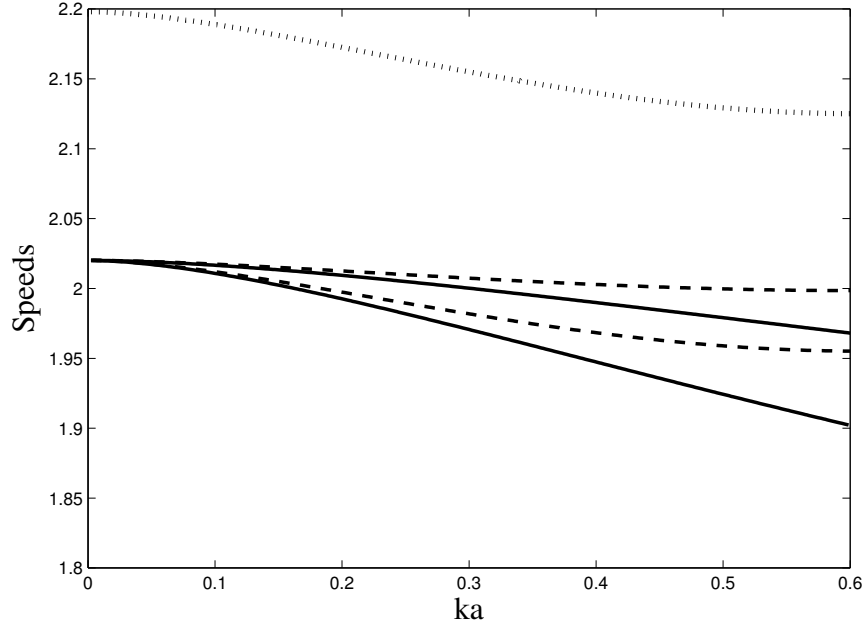


Figure 2.3: Dependence of the phase and group speeds of the kink mode upon the wave number. The speeds are normalised to the Alfvén speed inside the jet, and the wave number to the reciprocal of the jet radius. The solid lines correspond to the numerical solution of the exact dispersion relation, the upper and lower being the phase and group speeds, respectively. The dashed lines correspond to the asymptotic expressions utilising the limit $ka \rightarrow 0$, where the higher and lower curve are the phase and group speeds, respectively. The dotted line shows the asymptotic expression with both $ka \rightarrow 0$ and $\rho_e/\rho_0 \rightarrow 0$. In the calculations, $U_0 = 580$ km/s, $C_{Ae} = 2400$ km/s, $C_{A0} = 800$ km/s, $C_{s0} = 360$ km/s, $C_{se} = 120$ km/s, and $\rho_e/\rho_0 = 0.13$.

2.4 Expressions for the perturbations of the physical parameters

Linear perturbations of macroscopic physical parameters in the kink wave are expressed in terms of the divergence of the plasma velocity perturbation in the zero- β limit,

$$\begin{aligned}
\rho &= -\frac{\rho_{\{0,e\}}}{\Omega} \Delta(r) \sin \Theta, \\
B_z &= -\frac{B_{\{0,e\}}}{\Omega} \Delta(r) \sin \Theta, \\
v_\theta &= \frac{C_A^2}{(\Omega^2 - k^2 C_A^2) r} \Delta(r) \sin \Theta, \\
B_\theta &= -\frac{k B_{\{0,e\}} C_A^2}{(\Omega^2 - k^2 C_A^2) \Omega r} \Delta(r) \sin \Theta, \\
v_r &= \frac{C_A^2}{(k^2 C_A^2 - \Omega^2)} \frac{d}{dr} \Delta(r) \cos \Theta, \\
B_r &= -\frac{C_A^2 k B_{\{0,e\}}}{(k^2 C_A^2 - \Omega^2) \Omega} \frac{d}{dr} \Delta(r) \cos \Theta,
\end{aligned} \tag{2.17}$$

where $\Theta = \omega t + \theta - kz$, and

$$\Delta(r) = A_0 J_1(n_0 r), \quad r < a \tag{2.18}$$

inside the jet, and

$$\Delta(r) = \frac{A_0 J_1(n_0 a) K_1(m_e r)}{K_1(m_e a)}, \quad r > a \tag{2.19}$$

outside the jet, where A_0 is the amplitude of the perturbations. Note that the z component of the velocity perturbations is zero in the zero- β limit.

The transverse perturbations in the kink wave are *essentially* compressible, since they perturb the plasma density and the divergence of the velocity. The relations in equation (2.17) together with the dispersion relations provide a complete description of transverse perturbations caused by a linear kink wave guided by a field-aligned plasma jet. It can be used in the forward modelling of the observational manifestation of this phenomenon.

The emission intensity recorded by XRT is proportional to the integration of the

plasma density squared along the line-of-sight:

$$I_0 = \int_0^z K(T, n_e) n_e^2(z') dz', \quad (2.20)$$

where $K(T, n_e)$ is the contribution function [Aschwanden, 2005]. This expression is used in the forward modelling of the observation of kink waves on jets with XRT. First, a 4D (spatial 3D and time) data cube of the plasma density in the oscillating jet is created. Specifying the line-of-sight, we obtain a time sequence of 2D images (snapshots), showing the distribution of intensity to be observed. Some random variations in the intensity were added to represent e.g., the electronic noise and other processes missing in the model. The jet radius was 5 pixels, which should correspond to a jet of radius 3.6 Mm observed with Hinode/XRT.

In Figure 2.4, we show results for the forward modelling of an off-limb coronal loop with a dense vertical jet, as it would be seen with Hinode/XRT, with the jet experiencing transverse oscillations described by equation (2.17). Different snapshots correspond to different phases of the oscillation. The snapshots agree well with the observational results of Cirtain et al. [2007].

A standard approach to the analysis of kink waves is the method of a time-distance plot. Figure 2.5 shows a time-distance plot of the oscillation constructed with the use of the model developed in this Chapter. A one-pixel-wide slit across the oscillating jet is selected, and the intensity distribution along the slit is determined in each snapshot. The measure of intensity along the slit is plotted as a column. By stacking the columns from sequential snapshots along the horizontal axis of the plot, a representation of the intensity variation in distance and time is created.

2.5 Estimation of the damping time of kink waves in jets due to resonant absorption

If there is a variation in the Alfvén or flow speed across the jet, the kink perturbations are subject to resonant absorption. From basic physics we know that when ever the frequency of an incident wave entering a medium equals the natural frequency of the medium, resonance appears. For instance, this phenomena is responsible for the absorption of ultra-violet waves by glass. Since the frequency of ultra-violet waves is close to the natural frequency of oscillations in glass, resonance appears, resulting in absorption of ultra violet waves by glass.

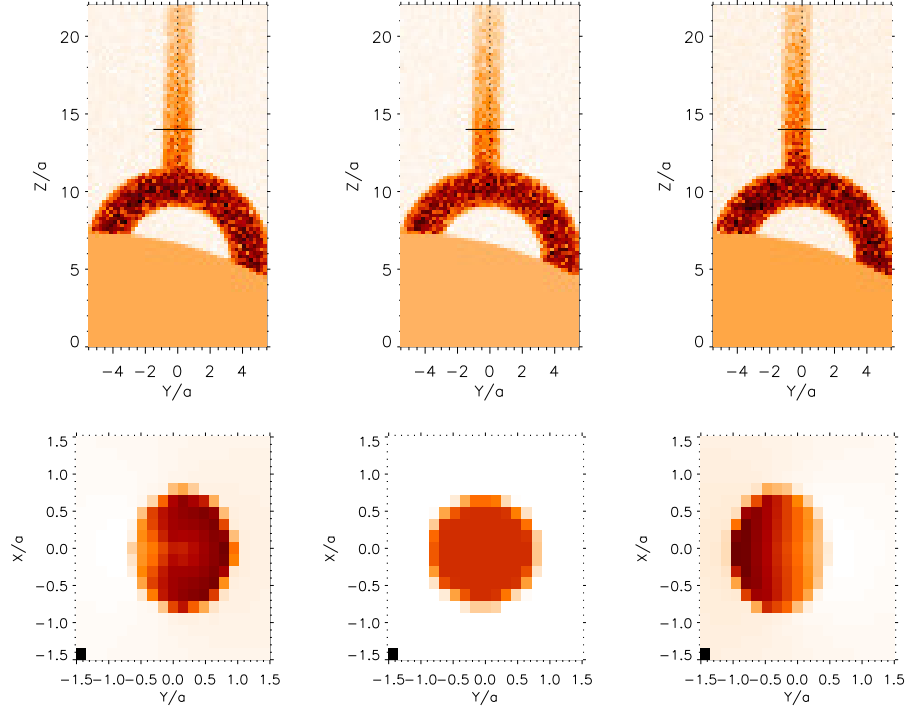


Figure 2.4: Forward modelling of transverse oscillations of a soft X-ray jet directed from an off-limb coronal loop seen by Hinode/XRT (with the pixel size about 727 km, the inverse colour table is used). The region in the bottom of the top row Figures shows the solar disk. The jet is the vertically positioned linear feature directed from the loop. The top row shows snapshots of the side view of an oscillating jet at times $t = 0$, $t = 0.125P$, and $t = 0.25P$, where P is the period of the oscillations. The jet oscillates in the plane perpendicular to the line-of-sight. The perturbation of the jet corresponds to the analytical solution of linearised MHD. The bottom row shows the density distribution over the jet cross-section at the location of the black slit indicated in the corresponding top panels. The jet radius is 3.6 Mm, and the oscillation displacement amplitude is 1.5 Mm, and other parameters as in Figure 2.3.

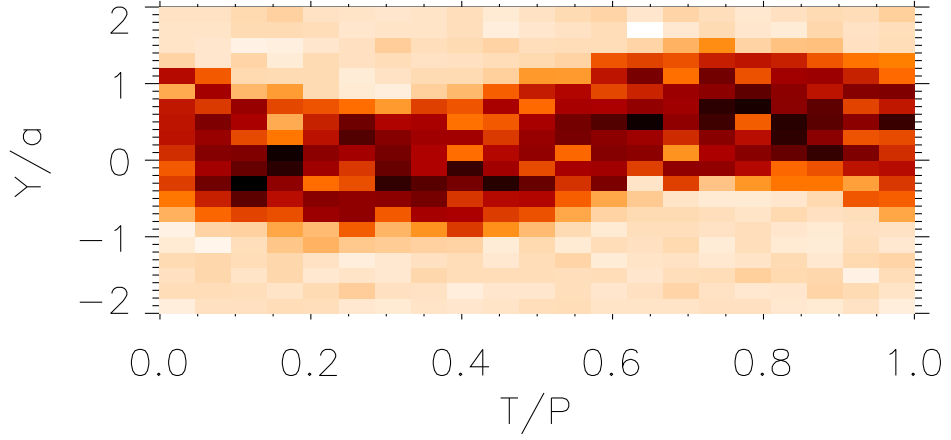


Figure 2.5: Time-distance plot of the oscillating jet, as it would be seen by Hinode/XRT (with the pixel size about 727 km, the inverse colour table is used). The slit position is shown in Figure 2.4. The spatial axis is normalised to the loop radius, and the time axis is normalised to the oscillation period. The perturbation of the jet corresponds to the analytical solution of the linearised MHD. The parameters of the simulation are the same as in Figure 2.4.

In MHD waves, if for example a fast magnetoacoustic wave in a jet is incident to the local Alfvén wave, in case the frequency of the magnetoacoustic wave equals the frequency of the Alfvén wave, we experience mode conversion due to resonance. Due to the fact of phase mixing of the Alfvén waves, rapid dissipation comes in to play which is called resonant absorption.

To calculate the damping of the oscillation, we use equation (76) from Goossens et al. [1992],

$$\gamma_{damp} = \frac{\rho_0^2(\Omega_0^2 - \omega_{A0}^2)^2}{2(\rho_0 + \rho_e)\omega_{cm}} \frac{\text{Sign}\Omega}{\rho(r_A)\Delta} \frac{m\pi}{r_A}, \quad (2.21)$$

with

$$\Delta = \frac{\omega_{Ae}^2 - \omega_{A0}^2}{2\delta}, \quad (2.22)$$

where

$$\omega_{A0} = C_A k, \quad \omega_{Ae} = C_{Ae} k, \quad (2.23)$$

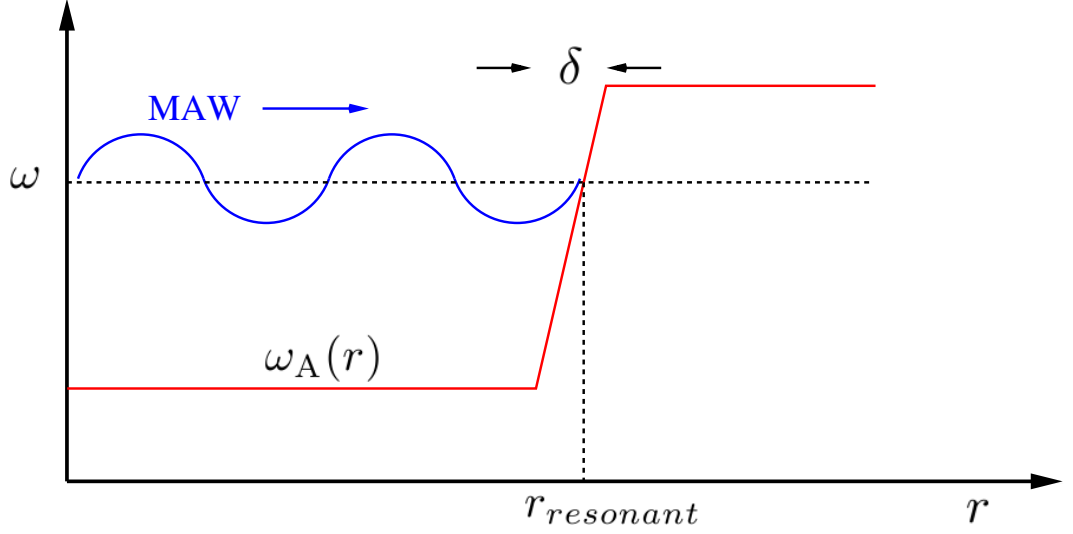


Figure 2.6: A global magnetoacoustic wave (blue lines) incident to a local Alfvén wave (red lines) on a flux tube surface. The slope is showing the resonant layer with thickness δ , and wherever the frequency of the fast magnetoacoustic wave is equal to the frequency of the Alfvén wave, we experience resonant absorption.

and δ is the thickness of the transition layer and r_A is the distance of the resonant layer from the jet axis. The transition layer is a layer between two media with different magnetic fields and density. These differences cause the Alfvén wave to have different frequencies in the two medium separated by the transition layer (see Figure 2.6).

If $\rho(r_A) = \rho_0$ and a being the tube radius, we would have:

$$\gamma_{damp} = \frac{(\Omega_0^2 - \omega_{A0}^2)^2}{2(1 + \rho_e/\rho_0)\omega_{cm}} \frac{\pi}{a} \frac{2\delta}{\omega_{Ae}^2 - \omega_{A0}^2}. \quad (2.24)$$

To estimate the damping time t_{damp} of the kink oscillations in a jet, taking the normalised parameters used in Figures 2.3 and 2.4 we obtain:

$$\frac{\gamma_{damp}}{\omega_{A0}} = \frac{(((2 - 0.725)^2 - 1^2)^2) k^3}{2(1 + 0.13)(1.365) k} \frac{\pi}{a} \frac{2\delta}{(3^2 - 1^2) k^2}, \quad (2.25)$$

which gives

$$\frac{\gamma_{damp}}{\omega_{A0}} = 0.099 \frac{\delta}{a}. \quad (2.26)$$

The damping time would be the inverse of the damping,

$$t_{damp} = \frac{1}{\gamma_{damp}}, \quad (2.27)$$

substituting equation (2.26) in (2.27), we obtain:

$$t_{damp} = \frac{10}{\omega_{A0}} \frac{a}{\delta}, \quad (2.28)$$

which gives the expression for the damping time in terms of the tube radius and the wave number. For the period of oscillations we know:

$$P = \frac{1}{f} = \frac{2\pi}{\omega}. \quad (2.29)$$

The ratio of the damping time to the period of oscillations would be easily obtained by dividing equation (2.28) by (2.29):

$$\frac{t_{damp}}{P} = \frac{10}{\pi} \approx 3, \quad (2.30)$$

where the ratio of ω/ω_{A0} has been taken 2. In addition, if we would like to see the dependence of the damping time on the geometry of the tube using observed data, we can take 800 km for the inside Alfvén speed and 200 seconds for the period and from Figure 2.3 we see the phase speed is about twice the inside Alfvén speed meaning we should take the phase speed about 1600 km per second. we could write:

$$\gamma_{damp} = 79.679 \left(\frac{\text{km}}{\text{s}} \right) \times \frac{\delta}{a} k, \quad (2.31)$$

the wave length would be:

$$\lambda = \frac{\omega}{k} P = 1600 \times 200 = 320000 \text{ km}, \quad (2.32)$$

resulting in

$$\gamma_{damp} = 0.00156 \frac{\delta}{a} \text{ s}^{-1}, \quad (2.33)$$

giving the damping time:

$$t_{damp}/\text{s} \approx 640(a/\delta), \quad (2.34)$$

where

$$a/\delta > 1 \quad (2.35)$$

is the ratio of the jet radius a to the width δ of the resonant layer and the wave phase speed coincides with the local Alfvén speed. For the observed period of about 200 s, the damping time is several times longer than the wave period. Hence, in the field-of-view of just one wave-length, no decrease in the wave amplitude could be observed. This justifies the model developed.

2.6 Excitation of transverse waves in jets

The origin of the transverse oscillations of soft X-ray jets has not yet been understood. One possible candidate mechanism could be the Kelvin-Helmholtz instability [Ferrari et al., 1981]. For a plasma cylinder of the observed geometry with the typical values of the Alfvén speed ($C_{Ae} = 3C_{A0}$, which correspond to the density contrast $\rho_e/\rho_0 \cong 0.13$), the instability threshold value of the steady flow speed would be

$$C_k^2 - \frac{\rho_0 \rho_e U_0^2}{(\rho_0 + \rho_e)^2} > 0, \quad (2.36)$$

$$U_0^2 < \frac{\rho_0}{\rho_e} C_{A0}^2 + C_{Ae}^2 + C_{A0}^2 + \frac{\rho_e}{\rho_0} C_{Ae}^2, \quad (2.37)$$

We get:

$$U_0 < 4.47 C_{A0}. \quad (2.38)$$

This means the Kelvin-Helmholtz instability threshold is:

$$U_0 = 4.47 C_{A0}. \quad (2.39)$$

Since the observed values of the jet speeds do not exceed the Alfvén speed inside the jet, the instability threshold is not reached and this possibility should be excluded. Another option is related to negative energy wave instabilities. However, according to Joarder et al. [1997] in the considered situation, sub-Alfvénic flow speeds can lead to the instability of longitudinal modes only, which does not explain the generation of the transverse perturbations. Also, the periodicity could appear because of geometric dispersion [Roberts et al., 1984; Murawski and Roberts, 1994; Nakariakov et al., 2004a]. However, the typical wavelength generated by this mechanism would

be comparable to the jet diameter and hence we exclude this option too. Consequently, we deduce that the observed transverse waves are excited somewhere at the origin of the jet, possibly by oscillatory magnetic reconnection [Murray et al., 2009] where an outflow of one reconnecting site provides the inflow for the other reconnecting site and vice versa, and then propagate according to the dispersion and phase relations discussed above.

2.7 Discussions and conclusions

We have demonstrated that transverse waves observed in soft X-ray coronal jets [Cirtain et al., 2007] are adequately described in terms of fast magnetoacoustic kink ($m = 1$) modes of a straight magnetic cylinder embedded in a magnetic environment. It is shown that these waves are collective, since they are coherent perturbations of all magnetic surfaces inside the jet, and compressible, since the flow-perturbation divergence is finite. Phase and group speeds are determined by the density contrast of the jet, the flow speed, and the internal and external Alfvén speeds. Forward modelling performed with the use of theoretically determined phase relations was found to be consistent with the observational findings obtained with Hinode/XRT. The expressions used in this Chapter are written for the azimuthal mode number $m = 1$. However, a transverse displacement of the axis of the cylinder, such as the transverse motion of the jet, can, in general, have two opposite senses, $m = \pm 1$. The azimuthal modes $m = \pm 1$ manifest themselves as a cork-screwing motion travelling along the cylinder. The $m = +1$ mode has a right-hand twist, whereas the $m = -1$ mode has a left-hand twist. Physically, the plane-polarised wave can be constructed by superposition of the $m = +1$ mode with an $m = -1$ mode of an equal amplitude. An elliptical cork-screwing motion may be constructed by superposing $m = +1$ and $m = -1$ modes with unequal amplitudes.

However, it is impossible to distinguish observationally between a pure $m = \pm 1$ mode or a superposition of these modes. Most of the solar observation facilities (except for STEREO) observe only the plane of the sky displacements (imaging telescopes) or the line-of-sight velocities (spectrographs). As such, it is only possible to measure the projected motion of the jet. It is impossible to quantify the motion in the other direction and thus to assess the nature (pure or superposition) of the observed oscillation. For Figure 2.4 we have displayed the plane polarisation, but it

is indistinguishable from that of an $m = \pm 1$ mode.

The jets are observed at heights of up to 100 Mm, while for plasmas of temperature e.g., 10 MK, the density scale height is about 500 Mm. This comparison allows us to ignore the stratification. However, in a more detailed study, effects of stratification and longitudinal structuring should be considered. It is unclear how the wave evolves past the physical extent of the jet, which will depend on the transverse structuring that is not visible in the observations.

Observation of transverse waves guided by soft X-ray jets is interesting in terms of coronal seismology. According to equations (2.8) and (2.16), the phase speed of these waves is about:

$$\omega/k \approx v_G \approx U_0 + C_{A0} \sqrt{1 + (B_e/B_0)^2}, \quad (2.40)$$

which is determined by the flow speed and the Alfvén speed inside the jet.

Another constraint is given by the equilibrium condition (equation 2.2), which can be rewritten as:

$$\rho_e/\rho_0 \approx (6/5 + C_{A0}^2/C_{s0}^2)/(C_{Ae}^2/C_{s0}^2), \quad (2.41)$$

where we have assumed that the external β is very small and $\gamma = 5/3$. These expressions contain observables: the phase speed of transverse waves, the flow speed [Cirtain et al., 2007], the density-contrast ratio (which can be obtained from the emission-measure contrast) and the sound speed (which is connected with the temperature). The use of the observed values in the theoretical constraints allows us to estimate the internal and external Alfvén speeds, and the magnetic fields.

Chapter 3

Long wave-length torsional modes of coronal plasma structures

The work in this Chapter is also published in Vasheghani Farahani et al. [2010].
Note that in Chapters 3 and 4 the CGS unit has been used.

3.1 Introduction

In Chapter 2 the model of a cylindrical plasma structure embedded in a plasma of different properties was used to study the kink oscillation in a coronal jet. This model could be applied to several other astrophysical objects, in particular coronal loops and plumes in the solar corona. Such a structure is known to support a number of magnetohydrodynamic (MHD) modes of oscillation, which can be divided into several classes according to their observational manifestation. In low- β plasmas, typical for the solar corona, the modes of plasma cylinders are kink, sausage, longitudinal, ballooning and torsional [e.g. Edwin and Roberts, 1983; Nakariakov and Verwichte, 2005]. In Chapter 1 the properties of these modes were discussed in the case of a straight magnetic field parallel to the axis of the cylinder in detail. The first four modes are compressible (modified slow or fast magnetoacoustic waves), while torsional modes (also known as rotational modes) are the only truly incompressible perturbations of the plasma [e.g., Van Doorselaere et al., 2008b] and propagate at the Alfvén speed, and hence should be considered as Alfvén waves. Torsional modes

are propagating azimuthal (rotational) motions of the plasma, accompanied by the perturbations of the azimuthal component of the magnetic field. Also, torsional modes can be considered as an alternating electric current aligned with the axis of the cylinder. Strictly speaking, in a plasma cylinder with a straight magnetic field, torsional waves are not modes, as perturbations of neighbouring magnetic surfaces are independent of each other and hence do not constitute a collective phenomenon. However, if the Alfvén speed is sufficiently uniform across the plasma structure and if the perturbations of the neighbouring magnetic surfaces are excited in phase, torsional perturbations manifest themselves in observations as a quasi-collective mode-like perturbation. Thus, from the point of view of the interpretation of observed phenomena the term “torsional mode” in our opinion is sufficiently justified.

A useful tool for the analytical study of long-wavelength axisymmetric (torsional and longitudinal, and, perhaps, sausage) perturbations of magnetic flux tubes is the second order thin flux-tube approximation derived by Zhugzhda [1996]. This approximation generalises the classical thin flux tube theory of Roberts and Webb [1978], accounting for the flux tube rotation and twist, and also the variation of its cross-section. In particular, it allows to consider the effects of the long-wavelength dispersion, connected with the presence of the characteristic spatial scale, the tube diameter, on the wave propagation [Zhugzhda, 1996]. It has been pointed out that in twisted magnetic flux tubes, the torsional modes become compressible. Soliton solutions appears because of the combination of weakly dispersive and weakly non-linear corrections to the sausage wave propagation were found in Zhugzhda and Nakariakov [1999]. An intensive following-up discussion [Zhugzhda and Goossens, 2001; Zhugzhda, 2002; Ruderman, 2005; Zhugzhda, 2005] revealed the necessity to pay attention to the induced perturbations in the external medium. However, this is of course not necessary if the external medium is a vacuum, and the plasma confinement is fulfilled by the internal magnetic twist.

The aim of this Chapter is to study long-wavelength (in comparison with the transverse size of the plasma cylinder) axisymmetric torsional modes in twisted and rotating plasma structures surrounded by vacuum, developing the work of Zhugzhda [1996] and Zhugzhda and Nakariakov [1999]. The paper is organised as follows. In the next section we discuss the manifestation of torsional modes and in section 3.3 we discuss the model and the equilibrium. In section 3.4 we consider the general dispersion relation in several asymptotic cases. In section 3.5 we derive phase relations between the perturbed physical quantities and study the compressibility of

torsional waves. The results obtained are summarised in conclusions.

3.2 Manifestation of torsional modes in the corona

In solar coronal studies, torsional modes have attracted great attention for several important reasons. Tapping [1983] considered this mode for the interpretation of high quality oscillations of the microwave emission generated in flaring loops by the gyrosynchrotron mechanism. The modulation of the emission can be produced by the change of the angle between the magnetic field and the line of sight modelled by a torsional wave. Another possible interpretation of quasi-periodic pulsations in solar flares, in terms of the oscillations in an equivalent LCR-circuit [e.g. Khodachenko et al., 2009, and references therein], links the pulsations with the alternating electric current in a flaring loop. The alternating field-aligned current can be described in terms of torsional waves. Hence, the development of the LCR-circuit model requires the understanding of the torsional wave dynamics.

Another popular research avenue is the role of torsional modes in coronal heating and solar wind acceleration, based upon the ability of torsional waves to penetrate easily into the corona [e.g. Ruderman, 1999; Copil et al., 2008]. In particular, Moriyasu et al. [2004] and Antolin et al. [2008] paid special attention to nonlinear effects and shock formation. It was demonstrated numerically that the observed spiky intensity profiles due to impulsive energy releases could be obtained from nonlinear torsional waves. Recently, Fletcher and Hudson [2008] proposed that a flare-generated large-scale torsional wave could be responsible for the bulk acceleration of electrons to high energies. Copil et al. [2008] suggested that propagating torsional waves could produce localised heating in coronal plasma threads. Also, torsional modes have been intensively studied in the context of the astrophysical jet collimation [e.g. Bisnovatyi-Kogan, 2007], where the periodic alternate magnetic twist provides the force that counteracts the total pressure and the centrifugal forces.

Despite the huge interest in torsional modes, unequivocal observational evidence of their presence in solar coronal plasma structures is absent due to intrinsic difficulties in their detection. Promising methods of their detection are based upon the Doppler shift of coronal emission lines and the modulation of the gyrosynchrotron emission. Unfortunately, the lack of the necessary spatial resolution in solar coronal observations does not allow one to resolve simultaneously the periodically varying red and blue Doppler shifts in different parts of a plasma structure. Spatially un-

resolved torsional modes manifest themselves as periodic non-thermal broadening. Zaqarashvili [2003] interpreted the variation of non-thermal broadening of the coronal “green” line along a coronal loop, with the period about 6 min, as the global (standing) torsional mode. Grechnev et al. [2003] suggested that 6-s oscillations of the hard X-ray and microwave emission in a solar flare could be produced by a torsional oscillation of the flaring loop. In the chromosphere, possible detection of torsional perturbations with the periods between 126 s and 700 s and an amplitude of 23 km/s was recently reported by Jess et al. [2009].

Theoretical investigation of torsional modes of magnetic plasma structures has been concentrated on various aspects of the wave propagation. In a non-rotating plasma cylinder with a straight magnetic field, torsional perturbations which are independent of the azimuthal angle ($m = 0$, where m is the azimuthal wave number, see section 1.4) propagate at the Alfvén speed inside the cylinder and are incompressible and dispersionless [e.g. Edwin and Roberts, 1983]. Transverse non-uniformity of the Alfvén speed and/or field-aligned steady flow profile leads to phase mixing of torsional perturbations [e.g. Ryutova and Habbal, 1995]. The effects of longitudinal variation of the Alfvén speed on the resonant frequencies of standing torsional modes of corona loops has been investigated by Zaqarashvili and Murawski [2007]. However, effects of the magnetic field twisting and the plasma rotation on the torsional modes are still not understood. There is still no direct observational evidence of the magnetic twisting of coronal plasma structures. On the other hand, this is often seen in numerical simulations of magnetic flux emergence [e.g., see Hood et al., 2009, for a recent discussion]. In addition, rotation of coronal plasma structures has been seen, e.g., in macropicules [Pike and Mason, 1998] also known as solar tornados, and one can expect solar coronal hot jets to be rotating.

3.3 Model and equilibrium conditions

In this work, we consider a rotating straight cylinder of a uniform plasma (a straight magnetic flux tube) with a twisted magnetic field (see Figure 3.1). A similar (while non-rotating) model was used in the study of Erdélyi and Fedun [2007]. Our governing set of equations is the second order thin flux tube approximation of Zhugzhda [1996]. This model allows us to take into account the equilibrium twist and rotation. In its derivation, the Taylor expansion of the physical variables with respect to the

radial coordinate r was used

$$\begin{aligned}\rho &\approx \tilde{\rho}, \quad p \approx \tilde{p} + p_2 r^2, \quad v_r \approx Vr, \quad v_\varphi \approx \Omega r, \quad v_z \approx u, \\ B_r &\approx B_{r1}r, \quad B_\varphi \approx Jr, \quad B_z \approx \widetilde{B_z},\end{aligned}\tag{3.1}$$

where B_r , B_φ and B_z are the radial, azimuthal and longitudinal components of the magnetic field, v_r , v_φ and v_z are the radial, azimuthal and longitudinal components of the velocity, ρ is the mass density, p is the gas pressure, V is the radial derivative of the velocity, J and Ω are the zeroth-order values of the current density and vorticity, respectively. Note that the 1 and 2 indices in B_{r1} and p_2 indicate the first and second order derivatives of the variables with respect to r . The quantities with the overtilde are the zeroth order terms of the expansions and their overtilde will be omitted here after. The linear dependencies of the twist and rotation on the radial coordinate correspond to the uniform twist and rotation. Applying expansion (3.1) to the MHD equations for a uniform medium, the set of second order thin flux tube approximation equations is obtained

$$\begin{aligned}\frac{\partial \Omega}{\partial t} + u \frac{\partial \Omega}{\partial z} + 2V\Omega + \frac{J}{4\pi\rho} \frac{\partial B_z}{\partial z} - \frac{B_z}{4\pi\rho} \frac{\partial J}{\partial z} &= 0, \\ \rho \left(\frac{\partial u}{\partial t} + u \frac{\partial u}{\partial z} \right) + \frac{\partial p}{\partial z} &= 0, \\ \frac{\partial \rho}{\partial t} + \frac{\partial(\rho u)}{\partial z} + 2\rho V &= 0, \\ \frac{\partial J}{\partial t} + \frac{\partial(uJ)}{\partial z} - B_z \frac{\partial \Omega}{\partial z} + 2VJ &= 0, \\ \frac{\partial B_z}{\partial t} + u \frac{\partial B_z}{\partial z} + 2B_z V &= 0, \\ \left(\frac{\partial}{\partial t} + u \frac{\partial}{\partial z} \right) \frac{p}{\rho^\gamma} &= 0, \\ p + \frac{B_z^2}{8\pi} - \frac{A}{2\pi} \left[\rho \left(\frac{\partial V}{\partial t} + u \frac{\partial V}{\partial z} + V^2 - \Omega^2 \right) \right. \\ &\quad \left. + \frac{1}{4\pi} \left(J^2 - \frac{1}{4} \left(\frac{\partial B_z}{\partial z} \right)^2 + \frac{B_z}{2} \frac{\partial^2 B_z}{\partial z^2} \right) \right] = p_T^{\text{ext}}, \\ B_z A &= \text{const},\end{aligned}\tag{3.2}$$

where $A = \pi R^2$ is the cross-sectional area of the tube of radius R , and p_T^{ext} is the external total pressure. Note that in equation (3.2) the relation containing the internal and external pressure terms is obtained by combining the radial component

of the Euler equation with the pressure balance condition [Zhugzhda, 1996]. Here the external plasma is taken to be non-rotating and without the magnetic twist. The effect of the gravitational force is neglected. All considered physical parameters are independent of the azimuthal coordinate. As it was stressed in Zhugzhda [1996], in the case of a twisted and rotating magnetic flux tube the second order term p_2 in the radial Taylor expansion (3.1) needs to be taken into account because it depends on the first order magnetic twist J , and could not then be neglected. This is also why we need to take into account the second order approximation of the pressure balance at the tube boundary mentioned in equation (24) of Ferriz-Mas et al. [1989]. The equilibrium pressure balance condition is

$$p_0 + \frac{B_{z0}^2}{8\pi} + \frac{A_0}{2\pi}(\rho_0\Omega_0^2 - \frac{J_0^2}{4\pi}) = p_{T0}^{\text{ext}}, \quad (3.3)$$

where J_0 , Ω_0 , B_{z0} , and A_0 are the equilibrium twist, rotation, magnetic field in the z -direction and the cross-section of the cylinder, respectively; and p_{T0}^{ext} is the equilibrium external total pressure. The equilibrium cross-section is connected with the equilibrium radius of the cylinder, a , $A_0 = \pi a^2$. The twist of the external magnetic field and the rotation of the external plasma are neglected. In the case without rotation and twist, equation (3.3) reduces to the standard total pressure balance condition (1.25). It is interesting that in the absence of the external total pressure, $p_{T0}^{\text{ext}} = 0$, i.e. when the external medium is treated as a vacuum without strong magnetic field, there is a possibility for an equilibrium. In this case, the magnetic tension force connected with the twist J_0 can counteract the internal total pressure and the centrifugal forces. Making use of the conservation of magnetic flux $\Phi = B_z A$, we obtain the following relationship between the equilibrium parameters:

$$B_{z0}A_0 = \Phi, \quad J_0A_0 = J_{\text{total}}, \quad \Omega_0A_0 = \text{const}, \quad (3.4)$$

where the last expression comes from the conservation of angular momentum. Linearising the thin flux tube equations with respect to the equilibrium we obtain:

$$\frac{\partial \Omega}{\partial t} + 2V\Omega_0 + \frac{J_0}{4\pi\rho_0} \frac{\partial B_z}{\partial z} - \frac{B_{z0}}{4\pi\rho_0} \frac{\partial J}{\partial z} = 0, \quad (3.5)$$

$$\rho_0 \frac{\partial u}{\partial t} + \frac{\partial p}{\partial z} = 0, \quad (3.6)$$

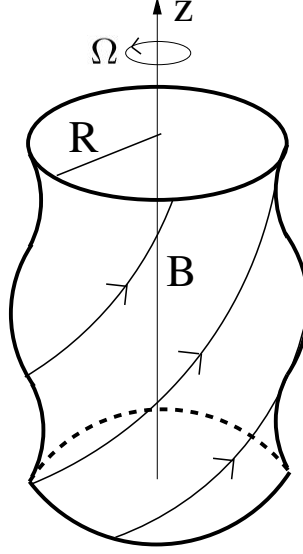


Figure 3.1: The sketch of a magnetised cylindrical flux tube with radius R , density ρ_0 , and gas pressure p_0 embedded in a non-magnetised medium. The cylinder has an equilibrium magnetic field parallel to the z axis B_{z0} , and an azimuthal magnetic field $B_{\varphi 0}$. Also the cylinder is rotating with the equilibrium angular speed Ω_0 .

$$\frac{\partial \rho}{\partial t} + \rho_0 \frac{\partial u}{\partial z} + 2\rho_0 V = 0, \quad (3.7)$$

$$\frac{\partial J}{\partial t} + J_0 \frac{\partial u}{\partial z} - B_{z0} \frac{\partial \Omega}{\partial z} + 2V J_0 = 0, \quad (3.8)$$

$$\frac{\partial B_z}{\partial t} + 2B_{z0} V = 0, \quad (3.9)$$

$$\frac{\partial p}{\partial t} - C_s^2 \frac{\partial \rho}{\partial t} = 0, \quad (3.10)$$

$$\begin{aligned} p + \frac{2B_{z0}B_z}{8\pi} - \frac{A_0 \rho_0}{2\pi} \frac{\partial V}{\partial t} + \frac{A_0 \Omega_0^2 \rho}{2\pi} + \frac{\rho_0 \Omega_0^2 A}{2\pi} \\ + \frac{A_0 \Omega_0 \rho_0 \Omega}{\pi} - \frac{J_0^2 A}{8\pi^2} - \frac{A_0 J_0 J}{4\pi^2} - \frac{A_0 B_{z0}}{16\pi^2} \frac{\partial^2 B_z}{\partial z^2} = p_T^{\text{ext}}. \end{aligned} \quad (3.11)$$

In general, the set of equations (3.5)-(3.10) should be supplemented by an equation describing the perturbation of the external total pressure p_T^{ext} (see Roberts and Webb [1979]) and radial velocity. The external and internal solutions are linked by the total pressure balance and the continuity of the transverse displacement boundary conditions applied at the cylinder boundary $r = a$. However, in the following con-

sideration, we restrict our attention to the plasma structures embedded in vacuum, and hence neglect the external pressure. Note that this is not a good assumption for coronal loops, but can be used for various jets, plumes and macrospicules.

3.4 Dispersion relations

Considering linear perturbations which are proportional to $\exp(i\omega t + ikz)$, one gets the dispersion relation:

$$\begin{aligned} & \frac{A_0}{4\pi(C_A^2 + C_s^2)} \left[\omega^6 + (2C_A^2\alpha^2 - 4\Omega_0^2 - k^2(2C_A^2 + C_s^2))\omega^4 \right. \\ & \quad + 4\Omega_0 k C_A^2 \alpha \omega^3 - 8\Omega_0 k^3 C_A^2 C_s^2 \alpha \omega \\ & \quad + (2(\Omega_0^2 C_s^2 + C_A^2 C_s^2 \alpha^2 - C_A^4 \alpha^2)k^2 + k^4 C_A^2 (2C_s^2 + C_A^2))\omega^2 \\ & \quad \left. + k^4 C_A^2 C_s^2 (2\Omega_0^2 + 2C_A^2 \alpha^2 - k^2 C_A^2) \right] \\ & \quad - (\omega^2 - k^2 C_A^2)(\omega^2 - k^2 C_T^2) = 0, \end{aligned} \quad (3.12)$$

where

$$\alpha = \frac{J_0}{B_{z0}}, \quad C_s^2 = \gamma \frac{p_0}{\rho_0}, \quad C_T^2 = \frac{C_A^2 C_s^2}{C_A^2 + C_s^2}. \quad (3.13)$$

The axial Alfvén speed is determined by the longitudinal component of the magnetic field, $C_A = B_{z0}/\sqrt{4\pi\rho_0}$. This 6-th order polynomial equation describes torsional, longitudinal and sausage perturbations in twisted and rotating magnetic flux tubes [Zhugzhda, 1996] in vacuum. In general, this equation does not have exact analytical solutions. In the following, we consider several useful limiting cases, which allow us to understand the dispersive properties of the modes.

3.4.1 Case $J_0 = 0$, $\Omega_0 = 0$

In the case of an untwisted ($J_0 = 0$) and non-rotating ($\Omega_0 = 0$) tube, the dispersion relation equation (3.12) reduces to

$$\begin{aligned} & \frac{A_0}{4\pi} (\omega^2 - C_A^2 k^2)^2 (\omega^2 - C_s^2 k^2) \\ & \quad - (C_A^2 + C_s^2) (\omega^2 - C_A^2 k^2) (\omega^2 - C_T^2 k^2) = 0. \end{aligned} \quad (3.14)$$

which describes three MHD modes. The familiar dispersion relation of the torsional modes readily separates (c.f. equation (1.35)),

$$\omega^2 = C_A^2 k^2. \quad (3.15)$$

The remaining bi-quadratic equation describes longitudinal and sausage modes,

$$\omega^2 = C_T^2 k^2 + \frac{A_0}{4\pi(C_A^2 + C_s^2)}(\omega^2 - C_A^2 k^2)(\omega^2 - C_s^2 k^2), \quad (3.16)$$

where the terms proportional to the tube cross-section A_0 are weak dispersion corrections, and in the long-wavelength limit the longitudinal scale of MHD perturbations is much bigger than its transverse scale, $A_0 k^2 \ll 1$. Assuming that

$$\omega^2 \approx C_T^2 k^2, \quad (3.17)$$

equation (3.16) becomes,

$$\omega^2 \approx C_T^2 k^2 \left(1 + \frac{A_0}{4\pi} \frac{C_T^2 k^2}{C_A^2 + C_s^2} \right). \quad (3.18)$$

Equation (3.18) coincides with equation (77) of Zhugzhda [1996] in case of an untwisted and non rotating flux tube. In the zero-order thin flux tube approximation [Roberts and Webb, 1978], this expression simplifies to the familiar dispersion relation for slow magnetoacoustic modes in the long-wavelength limit,

$$\omega^2 = C_T^2 k^2. \quad (3.19)$$

The concept and observations of the slow magnetoacoustic waves were discussed in section 1.4 and subsection 1.6.3.

Equation (3.18) describes the dispersive corrections connected with the finite tube radius effects. In addition, in a general case it is necessary to account for the dispersive effects connected with the external medium [see Zhugzhda and Goossens, 2001; Zhugzhda, 2002; Ruderman, 2005; Zhugzhda, 2005]. Another solution of equation (3.16) corresponds to sausage fast magnetoacoustic perturbations. Note that the concepts and observations of sausage modes in the solar atmosphere was discussed in section 1.4 and subsection 1.6.2. It can be easily seen in the zero- β limit, in which

the dispersion relation reduces to

$$\omega^2 - C_A^2 k^2 - \frac{C_A^2}{A_0/4\pi} = 0. \quad (3.20)$$

The last term of this equation is proportional to the reciprocal transverse wavelength in the situation when the rigid wall boundary conditions are applied. Hence in this case we have the dispersion relation that describes fast magnetoacoustic sausage waves in a plasma cylinder with a rigid wall. In the case of the soft boundary given by the balance of the total pressures inside and outside the tube, which is more typical for astrophysical applications, behaviour of the long-wavelength sausage mode is determined by the external medium [see, e.g. Pascoe et al., 2007].

3.4.2 Case $J_0 \neq 0$, $\Omega_0 = 0$

The case of a non-rotating twisted tube has been discussed in detail in Zhugzhda [1996]; Zhugzhda and Nakariakov [1999]. The dispersion relation is

$$-(C_A^2 + C_s^2 - \mathcal{K}C_A^2)(\omega^2 - C_+^2 k^2)(\omega^2 - C_-^2 k^2) + \frac{A_0}{4\pi}(\omega^2 - C_A^2 k^2)^2(\omega^2 - C_s^2 k^2) = 0, \quad (3.21)$$

where

$$C_{\pm}^2 = C_A^2 \frac{C_A^2 + 2C_s^2 + \mathcal{K}(C_s^2 - C_A^2) \pm \sqrt{\mathcal{S}}}{2(C_A^2 + C_s^2) - 2C_A^2 \mathcal{K}}, \quad (3.22)$$

and

$$\begin{aligned} \mathcal{S} &= C_A^4 + 2\mathcal{K}(3C_A^2 C_s^2 + 4C_s^4 - C_A^4) + \mathcal{K}^2(C_s^4 - 6C_s^2 C_A^2 + C_A^4), \\ \mathcal{K} &= \frac{J_0^2 A_0}{2\pi B_{z0}^2} = \frac{A_0 \alpha^2}{2\pi}. \end{aligned} \quad (3.23)$$

Equation (3.21) could be written in an explicit version,

$$\omega^2 \approx C_{\pm}^2 k^2 \pm \frac{A_0}{4\pi} \frac{(C_{\pm}^2 - C_A^2)^2 (C_{\pm}^2 - C_s^2)}{C_A^2 \sqrt{\mathcal{S}}} k^4. \quad (3.24)$$

The second term on the right hand side of equation (3.24) is the dispersive correction term. Equation (3.22) indicates the modification of the propagation speeds of the longitudinal (with the negative sign) and torsional (with the positive sign) waves by the equilibrium magnetic twist. Note that equation (3.24) indicates that the

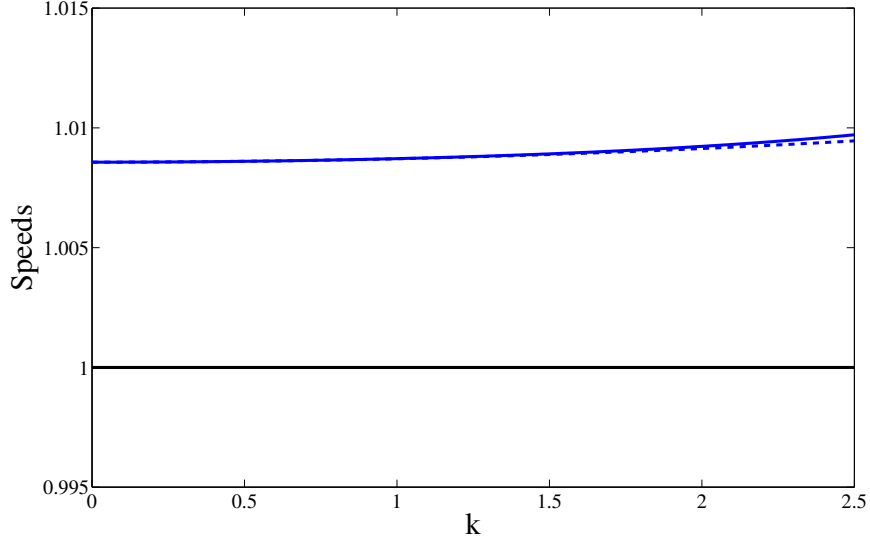


Figure 3.2: Dependence of the phase speeds of the torsional wave upon the wave number for $\beta = 0.1$. The speeds are normalised to the Alfvén speed, and the wave number is dimensionless which is $(\bar{k}^2 = k^2 A_0 / 4\pi)$ where we have dropped the overline. The solid lines correspond to the numerical solution of the exact dispersion relations, and the dashed lines correspond to the analytical approximations. The black curves are for the case where we have no equilibrium twist ($\mathcal{K} = 0$) and no rotation ($\mathcal{R} = 0$), and the blue curves show the effects of the equilibrium twist with $\mathcal{K} = 0.08$, and no rotation ($\mathcal{R} = 0$).

equilibrium twist modifies the wave speeds even in the limit $k = 0$. Also, mind a misprint in equation (19) of Zhugzhda and Nakariakov [1999]. In Figure 3.2 the dependence of the phase speeds on the wave number is shown. The solid blue line curve is obtained numerically using the exact dispersion relation (3.12), and the solid dashed line is obtained from the explicit approximation for the phase speed of the torsional wave (3.24). Figure 3.2 is showing the modification of the Alfvén speed to the fast magnetoacoustic speed by the equilibrium twist. Also it shows how good the approximation works, since the curves diverge at $k > 1$.

3.4.3 Case $\Omega_0 \neq 0$, $J_0 \neq 0$, zero- β limit

Consider the equilibrium with both twist and rotation to be non-zero ($\Omega_0 \neq 0$, $J_0 \neq 0$). A useful simplification can be obtained in the zero- β limit. In this case, disper-

sion relation (3.12) reduces to

$$(C_A^2 + 2\mathcal{R}C_A^2 - \mathcal{K}C_A^2)(\omega - C_+^{(+)}k)(\omega - C_+^{(-)}k) = \frac{A_0}{4\pi}(\omega^2 - C_A^2k^2)^2, \quad (3.25)$$

where

$$C_+^{(\pm)} = C_A \frac{\sqrt{\mathcal{K}\mathcal{R}} \pm \sqrt{\mathcal{Q}}}{1 + 2\mathcal{R} - \mathcal{K}}, \quad (3.26)$$

$$\mathcal{R} = \frac{A_0\Omega_0^2}{2\pi C_A^2} \quad (3.27)$$

and

$$\mathcal{Q} = 1 - \mathcal{K}\mathcal{R} + \mathcal{K}^2 - 2\mathcal{K} + 2\mathcal{R}. \quad (3.28)$$

Taking that the dispersion is weak, we obtain

$$\omega \approx C_+^{(\pm)}k \pm \frac{A_0}{8\pi C_A^3} \frac{(C_+^2 - C_A^2)^2}{\sqrt{\mathcal{Q}}} k^3. \quad (3.29)$$

Equation (3.29) generalises equation (81) of Zhugzhda [1996] (corrected for a misprint). Thus, the equilibrium twist and rotation modify the propagation speeds in the $k = 0$ limit.

In Figure 3.3 the dependence of the phase speeds on the wave number is shown. The solid blue line curve is obtained numerically using the exact dispersion relation (3.12), and the solid dashed line is obtained from the explicit approximation for the phase speed of the torsional wave (3.29). Figure 3.3 is showing the modification of the Alfvén speed to the fast magnetoacoustic speed by the equilibrium twist and rotation. Also it shows how good the approximation works, since the curves diverge at $k > 1$.

Equation (3.29) shows that the torsional waves propagate in opposite directions along the tube at different speeds. The difference in the speeds is governed by the term $\sqrt{\mathcal{K}\mathcal{R}}C_A$. This is similar to the case of untwisted non-rotating tubes with equilibrium field-aligned steady flows, when the asymmetry is caused by the Doppler shift [e.g. Nakariakov et al., 1996; Vasheghani Farahani et al., 2009]. In equation (3.29) the equilibrium steady flow is in the direction perpendicular to the direction of the wave propagation, but locally the Alfvénic perturbations propagate along the twisted magnetic field either downstream or upstream of the flow. Hence, in the considered case, the speed asymmetry is caused by the Doppler shift, too.

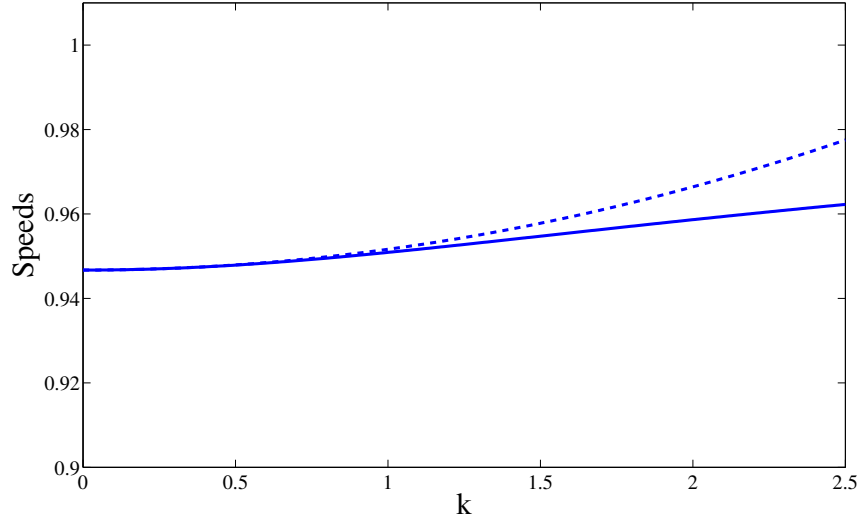


Figure 3.3: Dependence of the phase speeds of the torsional wave upon the wave number in the case where the equilibrium twist and rotation have been taken into account. The speeds are normalised to the Alfvén speed, and the wave number ($\bar{k}^2 = k^2 A_0 / 4\pi$) is dimensionless, where we have dropped the overline. The solid line corresponds to the numerical solution of the exact dispersion relation, and the dashed line correspond to the analytical approximation in the zero-plasma pressure limit ($\beta \rightarrow 0$). The normalised equilibrium twist and rotation parameters have been taken to be ($\mathcal{K} = 0.08$), and ($\mathcal{R} = 0.18$).

3.4.4 Standing oscillations of an infinite tube

Consider the $k = 0$ limit. In this case, dispersion relation (3.12) reduces to:

$$\frac{A_0}{4\pi(C_A^2 + C_s^2)}[\omega^6 + 2C_A^2\alpha^2\omega^4 - 4\Omega_0^2\omega^4] = \omega^4 \quad (3.30)$$

Equation (3.30) has two solutions, one is $\omega^4 = 0$, which corresponds to the longitudinal and torsional perturbations, and the other is

$$\omega^2 = \frac{4\pi(C_s^2 + C_A^2)}{A_0} - \frac{J_0^2}{2\pi\rho_0} + 4\Omega_0^2, \quad (3.31)$$

which is the sausage oscillation of a twisted and rotating magnetic cylinder in a vacuum. The frequency of the sausage oscillations depends upon the ratio of the fast magnetoacoustic speed to the radius of the tube, as well as upon the twist and the rotation.

A sufficiently twisted magnetic flux tube is subject to instability. Equation (3.31) describes the threshold of the sausage ($m = 0$) instability, $\omega^2 = 0$. In particular, in the zero- β non-rotating plasma equation (3.31) would be simplified to

$$\frac{4\pi C_A^2}{A_0} = \frac{J_0^2}{2\pi\rho_0} = \frac{B_{\varphi 0}^2}{2\pi a^2\rho_0} \quad (3.32)$$

where we have used

$$J_0 = \frac{B_{\varphi 0}}{a}, \quad (3.33)$$

finally we get

$$B_{z0}^2 = B_{\varphi 0}^2/2. \quad (3.34)$$

Equation (3.34) is the threshold of the sausage instability, meaning the stability condition is

$$B_{z0}^2 > B_{\varphi 0}^2/2, \quad (3.35)$$

which coincides with the expression obtained by other methods [e.g. Miyamoto, 2005].

3.5 Compressibility of the torsional mode

In an untwisted, non-rotating tube, the equations describing linear perturbations of the twist and rotation, equations (3.5) and (3.8) and governing the torsional mode, are decoupled from the rest of the linearised MHD equations. Thus, the torsional modes are incompressible and can be considered as true Alfvén waves in contrast with other modes. In the case of a twisted ($J_0 \neq 0$) and rotating ($\Omega_0 \neq 0$) tube, equations (3.5) and (3.8) are not independent of the other linear perturbations anymore. Thus, in this case, torsional perturbations become compressible: they perturb the plasma density and the absolute value of the magnetic field, induce longitudinal flows and perturb the tube cross-sectional area. The latter leads to the coupling of the torsional motions with the external medium, if it is not a vacuum. Consider the compressible perturbations in the torsional modes of a twisted ($J_0 \neq 0$) and rotating ($\Omega_0 \neq 0$) tube. We assume that the perturbations of the twist in the torsional wave are in the form

$$J = J_a \exp i(\omega t + kz), \quad (3.36)$$

where J_a is the amplitude of the twist perturbation, ω and k are related by equation (3.12).

Substituting expression (3.36) to equations (3.5)-(3.10) we obtain the following relations between the compressible variables with the amplitude of the torsional wave:

$$\begin{aligned} \left(\frac{\rho_a}{\rho_0}\right) &= \alpha_\rho J_a, \quad \left(\frac{V_a}{V_{ph}k}\right) = -i\alpha_V J_a, \quad \left(\frac{B_{za}}{B_{z0}}\right) = \alpha_{Bz} J_a, \\ \left(\frac{A_a}{A_0}\right) &= \alpha_A J_a, \quad \frac{u_a}{C_A} = \alpha_u J_a, \end{aligned} \quad (3.37)$$

where

$$\begin{aligned} \alpha_V &= \frac{1}{2} \left[1 - \left(\frac{C_A^2}{C_+^2} \right) \beta \right] \alpha_\rho, \quad \alpha_{Bz} = \left[1 - \left(\frac{C_A^2}{C_+^2} \right) \beta \right] \alpha_\rho, \\ \alpha_A &= - \left[1 - \left(\frac{C_A^2}{C_+^2} \right) \beta \right] \alpha_\rho, \quad \alpha_u = \left(\frac{C_A}{C_+} \right) \beta \alpha_\rho, \end{aligned}$$

and

$$\alpha_\rho = B_{z0} \sqrt{\frac{2\pi}{A_0}} \left(\sqrt{\mathcal{K}} - \frac{\pi C_A}{C_+} \sqrt{\mathcal{R}} \right) \times$$

$$\left\{ \rho_0 \left(1 - \left(\frac{C_A^2}{C_+^2} \right) \beta \right) \left[\frac{4\pi^2 C_+^2}{A_0 ((C_+^2/C_A^2) - \beta)} (\beta + \mathcal{R}) \right. \right. \\ \left. \left. + \left(\frac{4\pi^2 C_A^2}{A_0} \right) (1 + \mathcal{K}) - \pi k^2 (C_+^2 - C_A^2) \right. \right. \\ \left. \left. + \left(\frac{4\pi^2 C_A^2 \sqrt{\mathcal{R}}}{A_0 C_+} \right) (\sqrt{\mathcal{R}} C_+ - 2\sqrt{\mathcal{K}} C_A) \right] \right\}^{-1},$$

where u_a , ρ_a , B_a are amplitudes of perturbations of the z -component of flow, density, and magnetic field, respectively, A_a is the amplitude of the perturbation of the cross-section, V_a is the amplitude of the radial velocity; and V_{ph} is the phase speed of the torsional wave, given by equation(3.12). The coefficients α_u , α_ρ , α_V , α_B , and α_A are parameters, which depend on the difference between the phase speed of the torsional wave V_{ph} and the longitudinal Alfvén speed C_A . Clearly, in the untwisted and non-rotating limit $V_{\text{ph}} = C_A$, and the torsional wave becomes incompressible and independent of the external medium. We would also like to point out that V_a in equation (3.37) has the dimension s^{-1} (see equation (3.1)). The induced compressibility is associated with the departure of the perturbation from magnetic surfaces, as V_a is not zero. Hence, in this case the torsional wave cannot be considered as the true Alfvén wave and is rather a fast magnetoacoustic wave. More rigorously, in the case of a twisted and/or rotating tube, Alfvén torsional modes are linearly coupled with essentially compressible sausage and longitudinal modes. Consider the compressibility of the torsional waves in the zero- β limit ($\beta = 0$). Expressions (3.37) become

$$\left(\frac{\rho_a}{\rho_0} \right) = \alpha_\rho J_a, \quad \left(\frac{V_a}{V_{\text{ph}} k} \right) = -i\alpha_V J_a, \quad \left(\frac{B_{za}}{B_{z0}} \right) = \alpha_{Bz} J_a, \\ \left(\frac{A_a}{A_0} \right) = \alpha_A J_a, \quad u_a = 0, \quad (3.38)$$

where

$$\alpha_\rho = B_{z0} \sqrt{\frac{2\pi}{A_0}} \left(\sqrt{\mathcal{K}} - \frac{\pi C_A}{C_+} \sqrt{\mathcal{R}} \right) \times \\ \left\{ \rho_0 \left[\left(\frac{4\pi^2 C_A^2}{A_0} \right) (1 + \mathcal{K}) - \pi k^2 (C_+^2 - C_A^2) \right. \right. \\ \left. \left. + \left(\frac{8\pi^2 C_A^2 \sqrt{\mathcal{R}}}{A_0 C_+} \right) (\sqrt{\mathcal{R}} C_+ - \sqrt{\mathcal{K}} C_A) \right] \right\}^{-1}, \quad (3.39)$$

and

$$\alpha_{B_z} = \alpha_\rho, \quad \alpha_A = -\alpha_\rho, \quad \alpha_V = \alpha_\rho/2, \quad (3.40)$$

with

$$C_+^2 = C_A^2 \left(1 - 2\mathcal{R} + 2\sqrt{\mathcal{R}\mathcal{K}}\right). \quad (3.41)$$

For a non-rotating tube in the zero- β limit we obtain

$$\alpha_\rho = B_{z0} \sqrt{\frac{2\pi}{A_0}} \left(\sqrt{\mathcal{K}}\right) \times \left\{ \rho_0 \left[\left(\frac{4\pi^2 C_A^2}{A_0} \right) (1 + \mathcal{K}) - \pi k^2 (C_+^2 - C_A^2) \right] \right\}^{-1}. \quad (3.42)$$

Also, in this case the phase speed of the torsional mode reduces to the Alfvén speed C_A (see equation (3.41)). Hence

$$\alpha_\rho = B_{z0} \sqrt{\frac{2\pi\mathcal{K}}{A_0}} \left\{ \rho_0 \left[\left(\frac{4\pi^2 C_A^2}{A_0} \right) (1 + \mathcal{K}) \right] \right\}^{-1}, \quad (3.43)$$

or

$$\alpha_\rho = \frac{2J_0 A_0}{8\pi^2 \rho_0 C_A^2 + J_0^2 A_0}. \quad (3.44)$$

The equilibrium condition (3.3) in case of zero- β and zero rotation would be

$$\frac{B_{z0}^2}{8\pi} = \frac{A_0 J_0^2}{8\pi^2}, \quad (3.45)$$

which gives $B_{z0} = B_{\varphi 0}$, so equation (3.43) can be simplified to

$$\alpha_\rho = \frac{2a}{3B_{z0}}, \quad (3.46)$$

and the ratio of the density perturbation amplitude to the equilibrium density is written as:

$$\frac{\rho_a}{\rho_0} = \frac{2}{3} \frac{B_{\varphi a}}{B_{z0}}. \quad (3.47)$$

Equation (3.43) is consistent with the straight magnetic field limit, when the twist J_0 goes to zero, we get

$$\alpha_\rho = 0, \quad (3.48)$$

meaning the torsional mode becomes incompressible. In Figure 3.4 the parameters α_ρ is shown as a function of the twist \mathcal{K} and rotation \mathcal{R} parameters. According to (3.37), in the zero- β limit the torsional oscillations do not induce plasma flows along the tube. The induced variations of the plasma density are in phase with the variations of the twist and the absolute value of the magnetic field, and in anti-phase with the variations of the loop radius. These phase relations should be taken into account in the estimation of observational manifestation of torsional waves in twisted and possibly rotating plasma structures, e.g. in the gyrosynchrotron emission by the fashion similar to applied by Tapping [1983] to torsional modes and Nakariakov and Melnikov [2006] to longitudinal modes of straight non-rotating flux tubes. Also, these relations should be used in forward modelling of torsional waves observed with spectrometers.

3.6 Conclusions

We considered torsional axisymmetric ($m = 0$) long-wavelength MHD modes of a cylindrical plasma structure with the use of the second order thin flux tube approximation. The analysis was restricted to the case when the effect of the external medium was ignored. In this case, the equilibrium force balance is fulfilled by the balance of the total pressure and the centrifugal forces and the magnetic tension force. Such a model can describe various plasma structures in the corona of the Sun, e.g. coronal jets and plumes, as well as segments of coronal loops and filaments. A more general consideration accounting for the effect of the external medium, which is definitely more cumbersome and hence excluded from this paper, will be published elsewhere. According to the Kruskal–Shafranov theory, a twisted plasma column is unstable to sufficiently long-wavelength kink ($m = 1$) perturbations. However, in the case of jets, development of the instability takes some time and hence it will be seen at some distance downstream from the origin of the jet. Hence, it is possible to consider the propagation of torsional waves in jets which are kink-unstable, provided the waves are excited somewhere near the jet’s origin.

The general dispersion relation, linking frequencies of the MHD modes with their

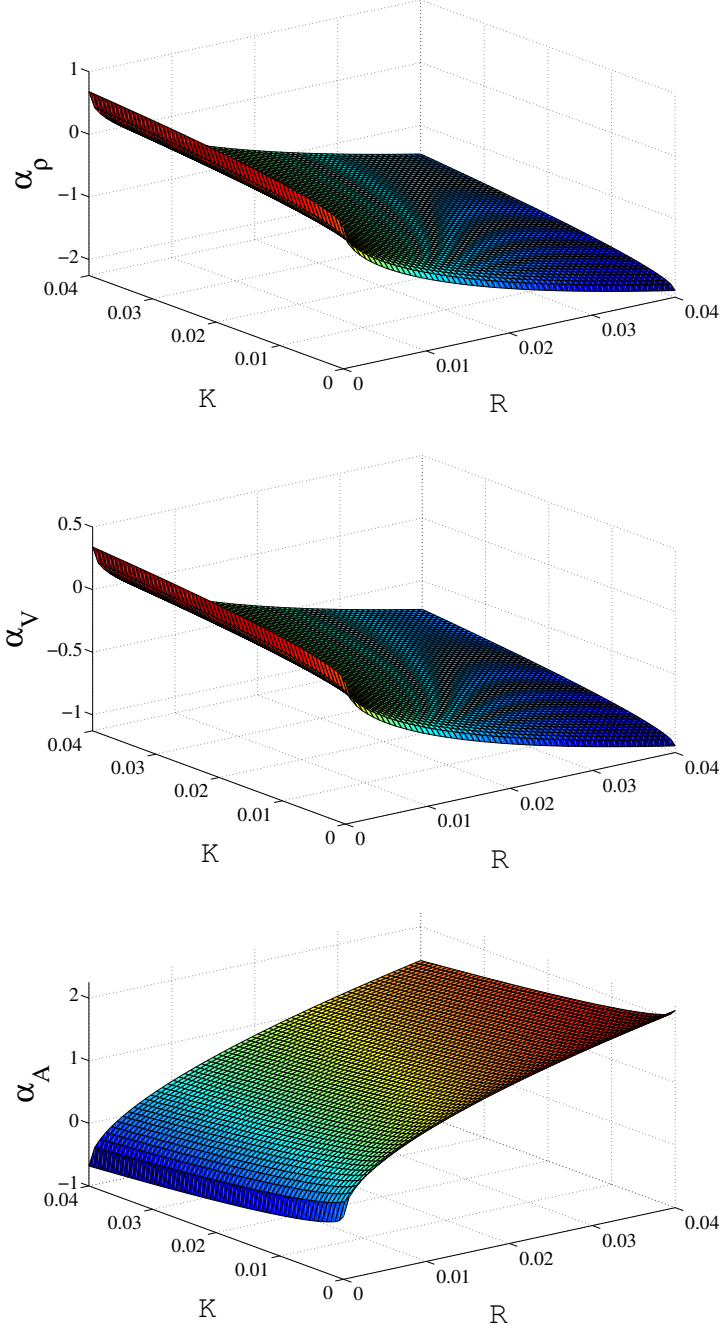


Figure 3.4: Dependence of the compressibility parameters α_ρ (top), α_V (middle), and α_A (bottom) which measures (a/B_{z0}) , upon the dimensionless equilibrium twist and rotation parameters. Representing the twist \mathcal{K} and rotation \mathcal{R} , in the zero- β limit. The wave number is taken to be ($k = 0$) and the z component of the equilibrium magnetic field is taken to be ($B_{z0} = 1$) with the Alfvén speed ($C_A = 1$).

wave numbers and parameters of the medium (the Alfvén and sound speeds, rotation and twist) is a sixth order polynomial. It describes all three MHD modes of the $m = 0$ symmetry: the torsional, sausage fast magnetoacoustic and longitudinal (slow magnetoacoustic) modes. In the untwisted non-rotating flux tube, sausage and longitudinal modes are dispersive, with the dispersion proportional to the ratio of the equilibrium radius of the tube to the wavelength. We would like to stress that in the untwisted limit the proper treatment of these waves requires consideration of the external medium, while in the twisted case considered here the equilibrium does not necessarily require the presence of the external plasma. In any case, both sausage and longitudinal modes are compressible and hence magnetoacoustic. In the untwisted non-rotating case, the torsional mode is dispersionless, and hence is the true Alfvén wave.

Equilibrium twist and rotation of the tube modify the torsional mode making it dispersive. Assuming the dispersion being weak, we derived asymptotic dispersion relations for the phase speeds of the modes. Interestingly, the phase speeds of the torsional waves propagating in the opposite directions along the tube have different absolute values, which is connected with the local Doppler shift.

In twisted magnetic flux tubes torsional waves become compressible, perturbing the plasma density, the absolute value of the magnetic field, and the tube cross-section. The induced variations of the plasma density and the absolute value of the magnetic field are in phase with the variations of the twist in the torsional wave, and in anti-phase with the variations of the loop radius. The compressibility vanishes in the limit when the equilibrium twist goes to zero, as it should be in the familiar case of the straight magnetic field.

Using the observations by Cirtain et al. [2007] for hot coronal jets, one could take the jet density and the magnetic field (along the jet axis) at equilibrium as $3 \times 10^8 \text{ cm}^{-3}$ and 10 G respectively, which for the Alfvén speed we would have

$$C_A = \left(\frac{B_0^2}{\mu \rho_0} \right)^{1/2} \approx 1200 \text{ km/s}, \quad (3.49)$$

and the sound speed could be estimated from

$$C_s = \left(\frac{2\gamma kT}{m_p} \right)^{1/2} \approx 370 \text{ km/s}, \quad (3.50)$$

where $\gamma = 5/3$ is the adiabatic constant, $k \approx 1.38 \times 10^{-23} \text{ m}^2\text{kg s}^{-2}\text{K}^{-1}$ is the Boltzmann constant, and $m_p \approx 1.67 \times 10^{-27} \text{ kg}$ is the proton mass, and T the coronal temperature is taken about $5 \times 10^6 \text{ MK}$. Having the values for the Alfvén speed between $1000 - 1200 \text{ km/s}$ and the sound speed about 370 km/s , β could be obtained as

$$\beta = \frac{2}{\gamma} \frac{C_s^2}{C_A^2} \approx 0.16, \quad (3.51)$$

Hence, the plasma can be treated as low- β . According to equation (3.47), a torsional wave of the relative amplitude 10 percent will be accompanied by a perturbation of about 7 percent. Our results provide theoretical basis for the search for torsional waves in coronal plasma structures, and, in particular, for the forward modelling of the EUV, soft X-ray and microwave observables.

Chapter 4

Nonlinear long-wave length torsional Alfvén waves

The work in this Chapter is also published in Vasheghani Farahani et al. [2011]

4.1 Introduction

Alfvén waves are often considered as the primary candidate for the acceleration of solar (e.g. Cranmer [2009]) and stellar (e.g. Charbonneau and MacGregor [1995]; Suzuki [2007]) winds and coronal heating (e.g. Ofman [2005]). Also, Alfvén waves are also considered in core-collapse supernova explosions [Suzuki et al., 2008]. However, observational evidence of Alfvén waves in astrophysical plasmas still remains indirect, e.g. as a possible interpretation of non-thermal broadening of coronal emission lines (e.g. Banerjee et al. [2009]) in coronal holes.

In non-uniform plasma structures, Alfvén waves are situated on magnetic surfaces. In the field-aligned structured coronal plasmas, Alfvén waves can be present in the form of torsional modes [see discussion in Van Doorsselaere et al., 2008a,b]. Torsional waves are intensively studied theoretically in the context of coronal heating [e.g. Antolin et al., 2008; Copil et al., 2008; Antolin and Shibata, 2010], coronal seismology [Zaqarashvili and Murawski, 2007; Verth et al., 2010] and particle acceleration in solar flares [Fletcher and Hudson, 2008].

There is some indirect evidence of torsional standing modes [Zaqarashvili, 2003] and propagating waves [Banerjee et al., 2009] in spectroscopic data, and also in mi-

crowave emission [Tapping, 1983; Grechnev et al., 2003]. Recently, torsional waves were suggested for the interpretation of propagating disturbances observed in the solar wind [Gosling et al., 2010].

The torsional Alfvén wave was studied in Chapter 3, in this Chapter we study compressible perturbations induced by long-wavelength weakly-nonlinear torsional waves which are essentially non-plane. One of the forces which is due to nonlinearity and is of crucial importance in our study here is the ponderomotive force.

4.2 Nature of the MHD ponderomotive force

The ponderomotive force is a feature of inhomogeneous oscillating electromagnetic fields. It is a nonlinear force which acts on a charged particle and tends it towards regions with weaker average fields. The nature and aspects of this force in MHD waves with examples of its applications are described in this Chapter.

The ponderomotive force is an alternative for the Lorentz force for studying the acceleration of charged particles by electromagnetic force. Simply because applying the Lorentz force to problems with even very little complexities, for example dynamical systems, may result in non-analytical solutions. Instead, if we average over the oscillation period (of oscillating electromagnetic fields) we obtain the ponderomotive forces which look more complicated since they are nonlinear compared to the Lorentz force which is linear, but the dynamics become simpler since they are approximated (see Lundin and Guglielmi [2006]).

For example, a charged particle moving in an oscillating electric field and a homogeneous magnetic field which are normal to each other, obeys a trajectory with eccentricity $\sqrt{1 - \omega^2/\Omega^2}$, where Ω is the gyroperiod frequency of the particle, ω is the frequency of the electric oscillations and $\Omega \gg \omega$. In physics, the effective magnetic moment of a charged particle could be obtained by averaging over the electric oscillating period. The effective interaction of the magnetic moment of a charged particle comes into play when the magnetic field is inhomogeneous. Hence, the average acceleration of the charged particle along the magnetic field is obtained by the ponderomotive force

$$F_{\parallel} = -\frac{mc^2}{2} \left(\frac{E}{B} \right)^2 \nabla_{\parallel} \ln B, \quad (4.1)$$

where m is the mass of the charged particle. Hence, the electromagnetic waves oscillate the charged particle along the magnetic field lines giving it an average acceleration (e.g. Lundin and Guglielmi [2006]).

Likewise, the introduction of a ponderomotive force in MHD allows one to study nonlinear flows, e.g. induced by MHD waves of finite amplitude. In the following, the manifestation of the ponderomotive force in MHD is demonstrated. Consider a uniform plasma with the equilibrium magnetic field B_0 in the x -direction, and the plane Alfvén waves polarised in the z -direction. Take in to account the Cartesian geometry (x, y, z) , with no dependencies of the physical parameters on the y and z coordinates ($\partial/\partial y = 0, \partial/\partial z = 0$) where the longitudinal direction is x . Ideal MHD equations in the weakly nonlinear regime in the low- β limit for typical coronal conditions are used, see equation (1.16)-(1.19). We obtain

$$\frac{\partial \rho}{\partial t} + \rho_0 \frac{\partial v_x}{\partial x} = -\frac{\partial}{\partial x}(\rho v_x), \quad (4.2)$$

$$\rho_0 \frac{\partial v_x}{\partial t} = -\frac{1}{2\mu} \frac{\partial B_z^2}{\partial x} - \rho \frac{\partial v_x}{\partial t} - \rho_0 v_x \frac{\partial v_x}{\partial x} - \rho v_x \frac{\partial v_z}{\partial x}, \quad (4.3)$$

$$\rho_0 \frac{\partial v_z}{\partial t} - \frac{B_0}{\mu} \frac{\partial B_z}{\partial x} = -\rho \frac{\partial v_z}{\partial t} - \rho_0 v_x \frac{\partial v_z}{\partial x} - \rho v_x \frac{\partial v_z}{\partial x}, \quad (4.4)$$

$$\frac{\partial B_x}{\partial t} = 0, \quad (4.5)$$

$$\frac{\partial B_z}{\partial t} - B_0 \frac{\partial v_z}{\partial x} = -\frac{\partial}{\partial x}(v_z B_z). \quad (4.6)$$

Where the nonlinear terms have been taken to the RHS of each equation ($B_z = B_{z1} + \epsilon B_{z2} + \dots$). If only linear terms are taken into account, equations for the perturbations of v_z and B_z decouple, and the Alfvén wave equation is obtained

$$\left[\frac{\partial^2}{\partial t^2} - C_A^2 \frac{\partial^2}{\partial x^2} \right] B_{z1} = 0, \quad (4.7)$$

with the d'Alembert solution describing two waves travelling in opposite directions,

$$B_{z1} = aB_0[f(x + C_A t) + g(x - C_A t)], \quad (4.8)$$

where f and g are arbitrary functions which are twice differentiable. If expression (4.8) is substituted in the equation for the perturbations of the longitudinal flow (equation 4.3), we obtain a force

$$\frac{1}{2\mu_0} \frac{\partial B_{z1}^2}{\partial x} = \frac{1}{2} \rho_0 a^2 C_A^2 \times \frac{\partial}{\partial x} \left[f^2(x + C_A t) + g^2(x - C_A t) + 2f(x + C_A t)g(x - C_A t) \right]. \quad (4.9)$$

This expression describes a ponderomotive force associated with the plane Alfvén wave (see Verwichte et al. [1999]). It could be noticed from equation (4.9) that the ponderomotive force is directed along the longitudinal magnetic field. Hence, this force would induce flows and density perturbations in the longitudinal direction. An important effect on MHD waves by the ponderomotive force is related to the third term on the RHS of equation (4.9) which is the cross-ponderomotive force. This force is responsible for the locally large density perturbations in time since there is no force to counteract its induced flows and density perturbations (see Verwichte et al. [1999] for details). However, the cross-ponderomotive force appears only in the situations when the Alfvén wave is either standing, or there are two Alfvén waves propagating in opposite directions, or one considers an initial stage of the evolution of an initially static Alfvénic pulse.

Rankin et al. [1994] performed a theoretical and numerical study on the ponderomotive force connected with magnetospheric standing MHD waves. In their analytical study they showed that the ponderomotive force generates higher harmonics of the fundamental waves and creates a secularly growing frequency for the perturbation of physical parameters. They showed that shear Alfvén waves couple nonlinearly with the slow magnetoacoustic wave in the low- β regime creating large amplitude shear Alfvén waves. In a similar study Tikhonchuk et al. [1995] considered the effect of the ponderomotive force on the evolution of the shear Alfvén wave in a cold plasma and concluded that the ponderomotive force causes steepening of the plasma density and the shear Alfvén wave.

Litwin and Rosner [1998] showed that the ponderomotive force associated with Alfvén waves upwardly propagating from the solar surface in coronal plasma structures can be significant to counter-act the gravitational force, and hence increase the density scale height. This result was applied to the explanation of the observed effect of “over-dense” cool coronal loops, discovered with the Coronal Diagnostic

Spectrometer (CDS) onboard SoHO . The effect is the observed enhancement in the density scale height in cool coronal loops by a factor of two, deduced from the soft X-ray emission measure. This effect was recently confirmed by the method of coronal seismology Van Doorselaere et al. [2008c].

Another model, proposed by Shukla and Bingham [2004] showed that the MHD ponderomotive force causes density enhancements which act as waveguides for the transmission of localised Alfvén waves from the photosphere to the corona.

Terradas and Ofman [2004] studied the nonlinear effects of standing MHD kink waves on the density perturbations in coronal loops and showed that the ponderomotive force creates flows along the loops and enhances mass on the loop apex.

4.3 The Cohen-Kulsrud equation

One of the key ingredients of the theoretical modelling of Alfvén waves in solar and stellar atmospheres is the concept of the nonlinear cascade. It is needed to explain the transfer of wave energy from the low-frequency injection range (that is 1-3 mHz, the typical times of the granulation motion and of 5-min oscillations, in the solar atmosphere) to the high-frequency dissipation range. In one-dimensional models, the nonlinear cascade is connected with nonlinear generation of higher harmonics, and hence steepening of the waves, causing the onset of nonlinear dissipation or of non-MHD dissipative processes. Spectrally, it is accompanied by the transfer of energy across the spectrum, from the energy injection range up to the dissipative range. In a uniform plasma, this process is analytically described by a weakly-nonlinear evolutionary equation, known as the Cohen–Kulsrud equation [Cohen and Kulsrud, 1974]

$$\frac{\partial B_1}{\partial t} = -\frac{1}{2} \frac{\partial}{\partial x} (u_2 B_1) = -\frac{1}{4} \frac{C_A}{(1-\beta) B_0^2} \frac{\partial}{\partial x} \left((B_1^2 - \langle B_1^2 \rangle) B_1 \right), \quad (4.10)$$

where u and B_0 are the x components of the velocity and magnetic field perturbed by the wave respectively and the index 1 and 2 represents the first and second order terms. The cubically-nonlinear term in this equation accounts for the nonlinear self-interaction of linearly or elliptically polarised, plane Alfvén waves via the wave-induced perturbation of the local Alfvén speed. These perturbations are often referred to as the nonlinearly-induced compressible motions in Alfvén waves. In contrast with the parallel magnetoacoustic waves (e.g., slow waves in the low- β

plasma of the solar corona), these perturbations exist even in the zero- β regime. Circularly polarised plane Alfvén waves are not subject to this effect.

4.4 Nonlinear flows induced by Alfvén waves

The compressible flows induced by nonlinear Alfvén waves have been intensively studied in the context of solar wind acceleration [e.g. Ofman and Davila, 1998]. A modified Cohen-Kulsrud equation describing spherical Alfvén waves in a stratified atmosphere with a radial magnetic field was derived in Nakariakov et al. [2000b] in application to coronal holes. Their analytical results are consistent with numerical MHD modelling performed in Torkelsson and Boynton [1998].

More advanced one-dimensional models for nonlinear Alfvén waves in solar and stellar atmospheres in open-field regions include up-flows, super-radial magnetic field geometry, non-adiabatic effects and various dissipation mechanisms [Suzuki, 2004; Suzuki and Inutsuka, 2005; Suzuki, 2007, 2008]. Secularly growing compressible perturbations, induced by standing Alfvén waves, have been considered in the context of coronal loop hydrostatics by Litwin and Rosner [1998], and in connection with magnetospheric field-line resonances by Tikhonchuk et al. [1995]. Secular compressible effects associated with travelling in opposite directions Alfvén waves were found in Verwichte et al. [1999]. All those studies were carried out in terms of a shear Alfvén wave model.

One-dimensional models mentioned above are based upon the assumption that the waves are plane. For long-period Alfvén waves, with periods of the order of the typical time scales of atmospheric dynamics, this condition is not fulfilled. For example, for a wave period of 10 minutes and an Alfvén speed of 1 Mm/s, the longitudinal wavelength is 600 Mm. In a plane wave, the transverse wavelength should be much larger than the longitudinal wavelength. Hence, for the generation of a plane Alfvén wave of period 10-minute period, the wave driver should be of the size exceeding the solar diameter. Also there should be no transverse structuring of the plasma in the Alfvén speed, otherwise the wavefront is distorted, and the wave becomes non-planar [e.g. Botha et al., 2000]. Thus, the study of the initial stage of the nonlinear cascade in the corona requires consideration of non-planar Alfvén waves.

4.5 Compressible flows induced by torsional waves

We are interested in torsional waves of wavelength much longer than the diameter of the wave-guiding magnetic flux tube with cylindrical coordinates (r, φ, z) . In an untwisted and non-rotating tube with the equilibrium magnetic field B_{z0} , mass density ρ_0 , and circular cross-section area A_0 , linear torsional waves are twisting azimuthal motions v_φ accompanied by the appearance of the azimuthal component of the magnetic field B_φ . At the axis of the flux-tube, both quantities vanish, and hence cannot be described by the first order thin magnetic flux theory of Roberts and Webb [1978], while they appear in the second-order thin flux-tube approximation of Zhugzhda [1996], see Chapter 3. Linear torsional waves are governed by the equations for the quantities $\Omega = v_\varphi/r$ and $J = B_\varphi/r$, which in the thin flux tube approximation correspond to the vorticity and electric current density, respectively,

$$\frac{\partial \Omega}{\partial t} - \frac{B_{z0}}{4\pi\rho_0} \frac{\partial J}{\partial z} = 0, \quad (4.11)$$

$$\frac{\partial J}{\partial t} - B_{z0} \frac{\partial \Omega}{\partial z} = 0, \quad (4.12)$$

where r is the radial coordinate. Also it is worth mentioning that in the magnetic cylinder, a torsional wave could exist on any cylindrical shell (magnetic surface), having an arbitrary dependence on r , provided v_φ and B_φ are zero on the axis of the cylinder. In the thin flux tube approximation, those dependencies are approximated by linear functions.

Equations (4.11) and (4.12) are readily combined in the wave equation,

$$\left[\frac{\partial^2}{\partial t^2} - C_A^2 \frac{\partial^2}{\partial z^2} \right] J = 0, \quad (4.13)$$

where $C_A = B_{z0}/\sqrt{4\pi\rho_0}$ is the Alfvén speed, see Chapter 3. In the linear regime, these motions are decoupled from compressible motions. The latter are described by the variables u and V , the longitudinal and radial components of the velocity, respectively, ρ the mass density, B_z the longitudinal component of the magnetic field, p the gas pressure and A the perturbation of the cross-sectional area of the flux tube. A long-wavelength torsional wave of a finite amplitude induces compressible motions by three forces: the centrifugal force connected with the azimuthal rotation of the plasma, the magnetic tension force caused by the magnetic field curvature,

and the ponderomotive force that is connected with the longitudinal gradients of the magnetic pressure perturbation in the torsional wave. The first two forces are absent from the plane wave theory of Alfvén waves and appear because of plasma structuring. These forces can modify the flux-tube cross-sectional area, hence inducing compressible plasma motions in the longitudinal and radial directions. In the second-order thin flux-tube approximation, these effects are taken into account in the transverse force-balance equation. The ponderomotive force causes the nonlinear self-interaction of Alfvén waves in the Cohen–Kulsrud equation formalism. We consider a weakly-nonlinear torsional wave and restrict our attention to the linear terms of the compressible variables, described by the equations

$$p + \frac{1}{4\pi} B_{z0} B_z - \frac{A_0 \rho_0}{2\pi} \frac{\partial V}{\partial t} - \frac{A_0 B_{z0}}{16\pi^2} \frac{\partial^2 B_z}{\partial z^2} = p_T^{\text{ext}} + \frac{A_0 J^2}{8\pi^2} - \frac{A_0 \rho_0 \Omega^2}{2\pi}, \quad (4.14)$$

$$\rho_0 \frac{\partial u}{\partial t} + \frac{\partial p}{\partial z} = -\frac{1}{4\pi} J R^2 \frac{\partial J}{\partial z}, \quad (4.15)$$

where p_T^{ext} is the total pressure in the external medium, and $R = \sqrt{A_0/\pi}$ is the flux-tube radius. The nonlinear terms associated with the torsional wave are on the right hand side. In equation (4.15) the term responsible for the ponderomotive force appears after accounting for the higher-order terms in the thin flux-tube expansion. Note that equation (4.15) shows that the longitudinal velocity perturbation is not zero when $\beta = 0$, while in the linear case (Chapters 2 and 3) the longitudinal velocity perturbation was zero.

The compressible variables are expressed through the longitudinal component of the magnetic field perturbation B_z , with the use of the linear expressions

$$\frac{\partial \rho}{\partial t} + \rho_0 \frac{\partial u}{\partial z} + 2\rho_0 V = 0, \quad (4.16)$$

$$\frac{\partial B_z}{\partial t} + 2B_{z0} V = 0, \quad (4.17)$$

$$\frac{\partial p}{\partial t} - C_s^2 \frac{\partial \rho}{\partial t} = 0, \quad (4.18)$$

where C_s is the sound speed. Equations (4.16)-(4.18) are readily combined in a driven wave equation for the density perturbation,

$$(C_s^2 + C_A^2)\mathcal{D}_T\rho + \frac{A_0}{4\pi}\mathcal{D}_s\mathcal{D}_A\rho = \frac{\partial^2 p_T^{\text{ext}}}{\partial t^2} + \frac{A_0}{2\pi}\frac{\partial^2}{\partial t^2}\left(\frac{J^2}{4\pi} - \rho_0\Omega^2\right) + \frac{R^2 C_A^2}{4\pi}\frac{\partial}{\partial z}\left(J\frac{\partial J}{\partial z}\right) + \frac{A_0 R^2}{16\pi^2}\mathcal{D}_A\frac{\partial}{\partial z}\left(J\frac{\partial J}{\partial z}\right), \quad (4.19)$$

where

$$\mathcal{D}_{T,s,A} = \frac{\partial^2}{\partial t^2} - C_{T,s,A}^2 \frac{\partial^2}{\partial z^2}, \quad \text{and} \quad C_T^2 = \frac{C_A^2 C_s^2}{C_A^2 + C_s^2}. \quad (4.20)$$

The last term on the right hand side of equation (4.19) can be neglected in comparison with the other terms, as it is proportional to $A_0/\lambda^2 \ll 1$, where λ is the longitudinal wavelength. The second term on the left hand side, responsible for wave dispersion, can be neglected too. Equation (4.19) describes the excitation of compressible motions by weakly nonlinear, long-wavelength torsional waves in a thin magnetic flux tube. In the following we ignore the perturbation of the total pressure in the external medium, p_T^{ext} , concentrating on the compressible flows inside the flux-tube.

$$(C_s^2 + C_A^2)\mathcal{D}_T\rho = \frac{A_0}{2\pi}\frac{\partial^2}{\partial t^2}\left(\frac{J^2}{4\pi} - \rho_0\Omega^2\right) + \frac{R^2 C_A^2}{4\pi}\frac{\partial}{\partial z}\left(J\frac{\partial J}{\partial z}\right), \quad (4.21)$$

also, the back-reaction of the induced compressible flows on the torsional waves through the modification of the local Alfvén speed and the flux-tube diameter is not considered. The latter assumption is justified by the consideration of the quadratically nonlinear terms only, while the consideration of the Alfvén wave self-interaction appears when the cubic nonlinearity is taken into account.

The first term on the right hand side of equation (4.21) has two terms associated with the nonlinear torsional wave, which have opposite signs. Hence, their combined effect on the compressible flows depends upon the phase relations between the twist and the rotation of the plasma in the torsional waves. Consider separately the cases of propagating and standing waves.

4.6 Propagating torsional waves

We take a propagating solution of equation (4.21),

$$J = j_a \cos(\omega t - kz), \quad (4.22)$$

where j_a is the amplitude of the magnetic twist, and ω and k are the frequency and the wavenumber, respectively, for which $\omega = \pm C_A k$. We use equation (4.11) to express the associated rotation of the flux-tube as

$$\Omega = -\frac{j_a}{(4\pi\rho_0)^{1/2}} \cos(\omega t - kz). \quad (4.23)$$

For such a solution, the first term on the right-hand side of equation (4.21) vanishes:

$$\frac{J^2}{4\pi} - \rho_0 \Omega^2 = \left(\frac{j_a^2}{4\pi} - \rho_0 \frac{(-j_a)^2}{4\pi\rho_0} \right) \cos^2(\omega t - kz) = 0. \quad (4.24)$$

This means that the effects of nonlinear magnetic twist and plasma rotation in the travelling wave cancel out each other, and do not add new effects to the nonlinear compressibility of propagating torsional waves. Thus, the induced compressible motions are described by the equation

$$(C_s^2 + C_A^2) \mathcal{D}_T \rho = -\frac{R^2 C_A^2}{4\pi} k^2 j_a^2 \cos[2(\omega t - kz)]. \quad (4.25)$$

with the driven solution

$$\rho = \frac{R^2 j_a^2}{16\pi C_A^2} \cos[2(\omega t - kz)]. \quad (4.26)$$

Thus, we obtain that the right hand side of equation (4.26) is independent of the value of the sound speed. Compare equation (4.26) with the case without transverse structuring, i.e. with plane shear Alfvén waves. Consider waves propagating in the z -direction, taking

$$\frac{\partial}{\partial x} = 0, \quad \text{and} \quad \frac{\partial}{\partial y} = 0. \quad (4.27)$$

Restrict our attention to the linearly polarised Alfvén waves, v_y and B_y . Following the formalism developed in Nakariakov et al. [2000a], we obtain the equivalent of

equation (4.21)

$$\mathcal{D}_s \rho = \frac{1}{4\pi} \frac{\partial}{\partial z} B_y \frac{\partial B_y}{\partial z}. \quad (4.28)$$

Taking

$$B_y = B_{ya} \cos(\omega t - kz), \quad (4.29)$$

we get

$$\mathcal{D}_s \rho = -\frac{1}{4\pi} B_{ya}^2 k^2 \cos(2\omega t - 2kz), \quad (4.30)$$

with the solution

$$\rho = \frac{B_{ya}^2 k^2}{16\pi(\omega^2 - C_A^2 k^2 \beta)} \cos(2\omega t - 2kz), \quad (4.31)$$

where $\beta = C_s^2/C_A^2$. With

$$j_a \approx B_{\varphi a}/R, \quad (4.32)$$

we observe that the right hand side terms in equations (4.26) and (4.31) are of the similar order. However, there is an important difference between solutions (4.26) and (4.31) is that in the case of torsional waves, there is no possibility for a resonance of the Alfvén waves with the sound wave. Note that in the zero- β limit, both solutions coincide. This could be illustrated in Figure 4.1 where for typical coronal conditions the Alfvén, sound, and tube speeds are plotted in respect to the distance from the Sun. For $C_s = 220$ km/s and $\beta = 0.07$ and the initial Alfvén speed equal to 800 km/s, it could be seen that the sound speed has resonance with the Alfvén speed in about 20 solar radius, but the tube speed never approaches the Alfvén speed and is always smaller.

Above, we found that the centrifugal and the magnetic tension forces are exactly cancelling each other in a long-wavelength propagating torsional wave. It is worth checking whether this effect is an artifact of the long-wavelength approximation. Consider the full MHD equations (see section 1.4), considering axisymmetric perturbations ($m = 0$). Equations (1.28) and (1.31) reduce to

$$\mu \rho_o \frac{\partial v_\varphi}{\partial t} = \frac{B_0}{r} \frac{\partial}{\partial z} (r B_\varphi), \quad (4.33)$$

$$\frac{\partial B_\varphi}{\partial t} = \frac{\partial}{\partial z} (B_0 v_\varphi), \quad (4.34)$$

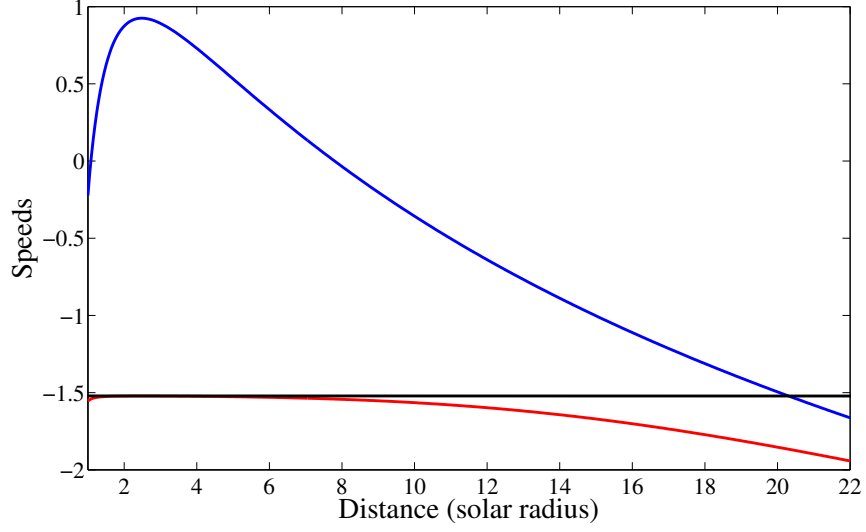


Figure 4.1: The logarithmic dependence of the Alfvén speed (blue curve), sound speed (black curve), and the tube speed (red curve) on the distance from the solar surface. The curves have been plotted using equation (23) of Nakariakov et al. [2000b]. The sound speed for typical coronal conditions would be about 0.22 Mm/s with $\beta = 0.07$ and C_A initially 0.8 Mm/s. It could be seen that the sound speed eventually crosses the Alfvén speed which could cause resonance, but the tube speed is always slower than the Alfvén speed.

linking v_φ and B_φ . Combining equations (4.33) and (4.34) we obtain the wave equation

$$\frac{\partial^2 B_\varphi}{\partial t^2} - C_A^2 \frac{\partial^2 B_\varphi}{\partial z^2} = 0. \quad (4.35)$$

By taking

$$B_\varphi = R j_a \cos(\omega t - kz), \quad (4.36)$$

and $\omega = C_A k$, the phase relation between the variables v_φ and B_φ could be found from equation (4.33) or (4.34)

$$v_\varphi = -\frac{B_{\varphi a}}{\sqrt{4\pi\rho_0}} \cos(\omega t - kz). \quad (4.37)$$

The centrifugal and magnetic tension forces per volume are

$$F_{centrifugal} = \frac{\rho_0 v_\varphi^2}{R}, \quad F_{tension} = \frac{B_\varphi^2}{4\pi R}. \quad (4.38)$$

From equation (4.37) the magnetic tension force per volume could be obtained in terms of v_φ

$$F_{tension} = \frac{\rho_0 v_\varphi^2}{R}. \quad (4.39)$$

Equations (4.38) and (4.39) show that the forces are also equal when using the full MHD model, which justifies the results obtained for the long-wavelength torsional waves in the second order thin flux tube approximation.

4.7 Standing torsional waves

We consider standing torsional waves that can exist in closed magnetic structures, e.g. coronal loops with $k = \pi/L$ where L is the loop length

$$\begin{aligned} J &= 2j_a \cos(\omega t) \cos(kz), \\ \Omega &= -2 \frac{j_a}{(4\pi\rho_0)^{1/2}} \sin(\omega t) \sin(kz), \end{aligned} \quad (4.40)$$

where the phase relations between the perturbed magnetic twist and the vorticity are obtained from equations (4.11) and (4.12). Substituting equations (4.40) in equation (4.21), and neglecting dispersive effects, higher order terms and the perturbations of the external medium, we obtain

$$\begin{aligned} (C_s^2 + C_A^2) \mathcal{D}_T \rho &= -\frac{R^2 C_A^2}{2\pi} j_a^2 k^2 (1 + \cos(2\omega t)) \cos(2kz) \\ &\quad - \frac{A_0 j_a^2 \omega^2}{\pi^2} \cos(2\omega t). \end{aligned} \quad (4.41)$$

The first term on the right hand side represents the ponderomotive effect, and the second term contains the magnetic tension and centrifugal effects. In the finite- β case with the constraint $\beta \ll 1$ the solution for equation (4.41) is

$$\rho = -\frac{R^2 j_a^2}{8\pi C_s^2 (1 + \beta)} (1 - \cos(2C_s k t)) \cos(2kz)$$

$$+ \left(\frac{R^2}{4\pi C_A^2(1+\beta)} + \frac{R^2 \cos(2kz)}{8\pi C_A^2} \right) \times j_a^2 \cos(2\omega t), \quad (4.42)$$

where $\omega = C_A k$. Equation (4.42) is similar to equation (13) of Tikhonchuk et al. [1995] obtained for shear Alfvén waves. In the zero plasma- β limit, equation (4.42) simplifies to

$$\rho = -\frac{R^2(\omega t)^2}{4\pi C_A^2} j_a^2 \cos(2kz) + \left(\frac{R^2}{4\pi C_A^2} + \frac{R^2}{8\pi C_A^2} \cos(2kz) \right) j_a^2 \cos(2\omega t). \quad (4.43)$$

Equation (4.43) is an analogue of equation (4) of Tikhonchuk et al. [1995]. In Figure 4.2 the ratio of the density perturbations to the equilibrium density has been plotted against the dimensionless time scale $\bar{t} = C_A k t$, where we have omitted the overline in Figure 4.2. Also the ratio $B_{\varphi a}/B_{z0}$ has been taken equal to 0.1. From equation (4.43) we obtain the black curve which is for the case $\beta = 0$, and from equation (4.42) we obtain the coloured curves where the red, green, and blue curves correspond to the values 0.01, 0.1 and 0.5 of the plasma- β . It could be seen that as the plasma- β increases, the oscillatory behaviour of the density ratio is more pronounced.

According to equation (4.42), standing torsional waves induce growing compressible perturbations, similarly to standing shear Alfvén waves [Tikhonchuk et al., 1995; Verwichte et al., 1999; Litwin and Rosner, 1998] and standing kink modes of coronal loops [Terradas and Ofman, 2004]. The growth is connected with the ponderomotive term on the right hand side of equation (4.41). Finite- β effects cause saturation of the compressible perturbation. Using the results obtained for shear Alfvén waves, we obtain that the highest value of the density perturbation,

$$\frac{\rho}{\rho_0} = \frac{R^2 j_a^2}{4\pi \rho_0} \frac{1}{C_s^2(1 + C_s^2/C_A^2)}, \quad (4.44)$$

is reached at the time

$$t_{max} \simeq \frac{L}{2C_s}, \quad (4.45)$$

where L is the loop length.

Also, in the case of standing waves, the centrifugal and magnetic tension terms do not cancel each other, and produce compressible perturbations oscillating at the double frequency of the torsional wave. However, those terms do not cause the secular growth of compressible perturbations.

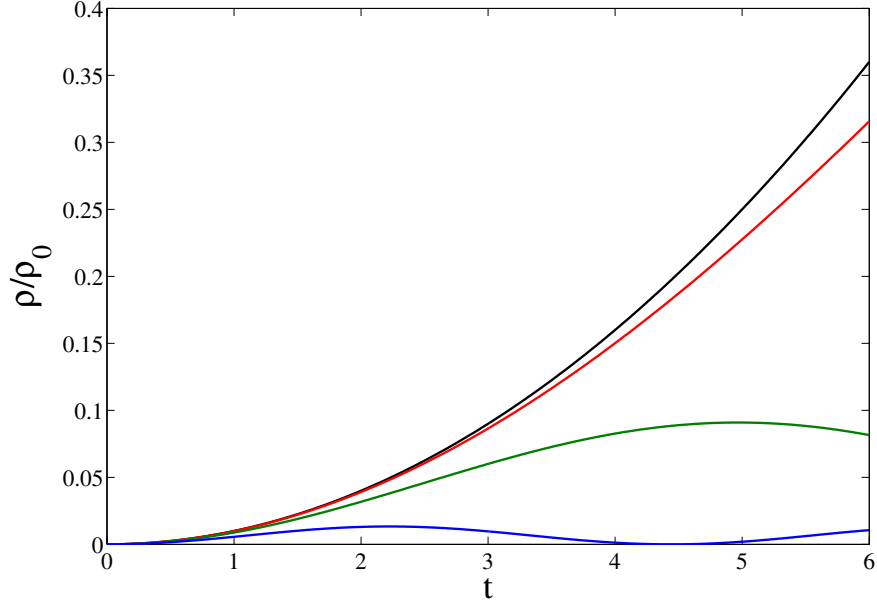


Figure 4.2: Dependence of the ratio of density perturbations to the equilibrium density against the dimensionless characteristic time scale $\bar{t} = C_A k t$ where we have omitted the overline in the figure. The black curve is plotted using expression (4.43), showing the secular growth of the density perturbation. The red, green and blue curves have been plotted using expression (4.42) for different values of the plasma- β , 0.01, 0.1, and 0.5 respectively. Note that the ratio of the azimuthal magnetic field amplitude in respect to the equilibrium longitudinal magnetic field $B_{\varphi a}/B_{z0}$ has been taken equal to 0.1.

4.8 Conclusions

We considered compressible perturbations induced in straight untwisted and non-rotating magnetic flux tubes by weakly-nonlinear long-wavelength torsional waves. We can summarise our findings as follows: Long-wavelength torsional waves induce compressible perturbations by the ponderomotive, centrifugal and magnetic twist forces. The perturbations have double the frequency of the inducing torsional wave. The efficiency of the excitation depends upon the spatial (standing and propagating) structure of the inducing torsional wave.

The efficiency of the generation of compressible perturbations by long-wavelength torsional waves is independent of the plasma- β (see equation (4.26)). This result is different from the excitation of compressible perturbations by plane shear Alfvén

waves, in which case the efficiency grows when the Alfvén and sound speeds approach each other. The difference is connected with the fact that the tube speed is always lower than the Alfvén speed. The relative amplitude of the induced density perturbation is

$$\frac{\rho}{\rho_0} = \frac{B_\varphi^2}{4B_{z0}^2}, \quad (4.46)$$

where B_φ is the perturbation of the magnetic field at the boundary of the flux tube. There are two kinds of compressible perturbations induced by standing torsional waves: the perturbations which grow with the time scale

$$t \propto \frac{1}{2C_s k}, \quad (4.47)$$

where k is the longitudinal wave number of the torsional wave, and the perturbations oscillating at the double frequency of the driving torsional mode. The growing density perturbations saturate at the level inversely proportional to the sound speed. Thus we conclude that nonlinear compressible effects which accompany standing weakly-nonlinear long-wavelength torsional waves are similar to those derived for plane shear Alfvén waves. For propagating waves, the efficiency of the nonlinear generation of compressible perturbations does not grow with the plasma- β . This effect should be taken into account in one-dimensional models of the solar and stellar wind acceleration by Alfvén waves.

Chapter 5

Fast magnetoacoustic waves approaching an X-point

The work in this Chapter is also published in M. Gruszecki, S. Vasheghani Farahani, V.M. Nakariakov, T.D. Arber [2011]

5.1 Introduction

In subsection 1.6.5 the concept of magnetic reconnection and its relevance to solar coronal physics was mentioned. In this Chapter our aim is to study analytically and numerically (using the Lare2D code), the dynamics of fast magnetoacoustic waves approaching a magnetic reconnection site which is modelled as a magnetic null-point (x-point) without the guiding field. In a null-point, magnetic field lines change direction as getting close to the middle cross, never crossing it (see Figure 5.1). The lines that create the cross are called separatrices which divide the plane into four regions. Since there is no magnetic fields on the null-point in the absence of the guiding field, the Alfvén speed approaches zero at exactly on the null-point. Coronal magnetic fields, extrapolated from photospheric magnetograms show the possible existence of magnetic null-point-structures [Brown and Priest, 2001]. Detailed discussion of structures of magnetic field in solar corona could be found in e.g. Brown and Priest [2001] and Longcope [2005].

The aim of this Chapter is to investigate the generation of shocks in fast magnetoacoustic waves with various initial amplitudes and width, as they approaching the magnetic null-point in order to study the possibility of the triggering of solar

flares by fast magnetoacoustic waves. This can be achieved by the deposition of the anomalous resistivity (see subsection 1.6.5) in the nearest vicinity of the null-point by the current density spike generated by the wave.

From the point of view of the fast magnetoacoustic wave, the vicinity of a magnetic null-point is a potential well, as the fast magnetoacoustic speed usually decreases towards the null-point. Hence, inwardly, with respect to the null-point, propagating fast waves experience the amplitude growth because of their focusing and because of the nonuniformity of the fast speed, as the energy should conserve. The amplitude growth leads to various nonlinear effects which cause the wave steepening and fast shock formation. If the wave shocks at some large distance from the null-point it cannot form a current spike near the null-point, and hence cannot trigger reconnection. We shall study this phenomenon in detail.

5.2 Analytical and numerical models of magnetic null-point dynamics

Various models for the magnetic null-point dynamics have been put forward, and here we summarise the most widely accepted models. Craig and McClymont [1991] considered the magnetoacoustic $m = 0$ (where m is the azimuthal wave number) mode disturbing an equilibrium null-point. They took into account the magnetic diffusivity and showed that the decay of the $m = 0$ mode oscillations on the null-point is limited by the dissipation time scale of the fundamental mode with no dependency on the number of radial nodes. The magnetic reconnection was found to show oscillatory dynamics. It was deduced that oscillatory reconnection is caused by the dissipation of free magnetic energy. In addition, waves in the neighbourhood of a 2D null point have been investigated by Craig and Watson [1992]. They considered the radial propagation of the $m = 0$ mode in the zero- β regime and stated that reconnection could only take place if the disturbances are purely radial. Also, they confirmed that the reconnection is oscillatory and fast, with a logarithmic dependency on magnetic resistivity η .

McLaughlin and Hood [2004] in a 2D study in the zero- β regime, studied the behaviour of a single fast magnetoacoustic wave-pulse approaching a null point. They showed that the wave-pulse never exactly gets to the null point in this model, since the Alfvén wave loses speed getting closer to the null-point. Due to refraction [Nakariakov and Roberts, 1995b], the wave-pulse bends around the null-point cre-

ating a density spike normal to the null-point plane in both directions. Later, McLaughlin and Hood [2006] extended their model to the finite- β regime and noticed coupling between slow and fast magnetoacoustic waves and mode conversion at locations where the sound and Alfvén speed get close to each other. Note that similar effects were studied by Zhugzhda and Dzhalilov [1982] and Cally [2001] in the context of wave energy transport in an isothermal magneto-atmosphere.

Longcope and Priest [2007] studied the resistive dissipation of a 2D current sheet above the null-point due to anomalous resistivity (see subsection 1.6.5). They used Cartesian geometry to describe a planar equilibrium magnetic field for the null-point and a two dimensional current sheet which is placed in the equilibrium magnetic field. They deduced that due to the disruption of the current sheet by diffusion, fast magnetoacoustic waves could be launched by null-point reconnection. Note that the dynamics of fast magnetoacoustic waves is our interest in this Chapter.

In a very recent study McLaughlin et al. [2009] by taking into account nonlinear effects, observed both fast and slow magnetoacoustic shocks. Their study extended their previous investigations, considering the developed stage of the wave evolution. The distance of the shock generation of the fast magnetoacoustic wave in respect to the null-point and its dependence on the initial conditions of the pulse is studied in this Chapter.

5.3 Theoretical analysis

5.3.1 Model and equilibrium conditions

Ideal MHD equations for typical coronal conditions in the low- β regime are taken in to account using the cylindrical coordinate system (r, φ, z) , see equations (1.16)-(1.19), taking $\gamma = 5/3$ as the ratio of specific heats. Our choice of equilibrium is (Craig & McClymont 1991)

$$\mathbf{B}_0 = (B_0 \frac{r}{L} \sin 2\varphi, B_0 \frac{r}{L} \cos 2\varphi, 0), \quad (5.1)$$

where L is a characteristic length scale, r is the radial distance from the null-point and φ is the azimuthal angle (Figure 5.1). Also we consider the gas pressure, density, and temperature to be constant around the null point.

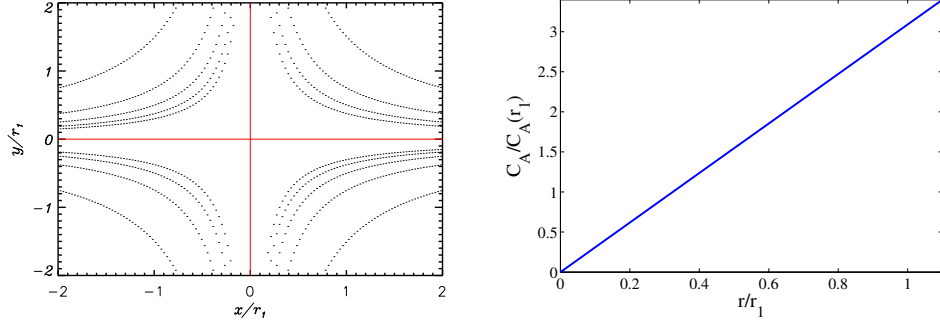


Figure 5.1: The null-point configuration showing the equilibrium magnetic field lines (curved lines) and the separatrices (red lines) which separate the configuration into four quarters (left panel). The Alfvén speed dependence on the distance to the null-point (right panel). The parameters are normalised by the distance of the initial pulse to the null-point (r_1).

In this equilibrium, the radial dependence of the Alfvén speed is

$$C_A(r) = \frac{B_0 r}{\sqrt{\mu \rho_0} L}. \quad (5.2)$$

Linearising the MHD equations with respect to the equilibrium and considering no azimuthal dependency ($\partial/\partial\varphi = 0$) and also no dependency on the z coordinate ($\partial/\partial z = 0$), that is the coordinate perpendicular to the plane of the null-point, we obtain:

$$\mu \rho_0 \frac{\partial v_r}{\partial t} = -\frac{B_0 \cos 2\varphi}{L} \frac{\partial (r B_\varphi)}{\partial r}, \quad (5.3)$$

$$\mu \rho_0 \frac{\partial v_\varphi}{\partial t} = \frac{B_0 \sin 2\varphi}{L} \frac{\partial (r B_r)}{\partial r}, \quad (5.4)$$

$$\mu \rho_0 \frac{\partial v_z}{\partial t} = +\frac{B_0 r \sin 2\varphi}{L} \frac{\partial B_z}{\partial r}, \quad (5.5)$$

$$\frac{\partial B_r}{\partial t} = 0, \quad (5.6)$$

$$\frac{\partial B_\varphi}{\partial t} = \frac{B_0}{L} \frac{\partial (v_\varphi r \sin 2\varphi)}{\partial r} - \frac{B_0}{L} \frac{\partial (v_r r \cos 2\varphi)}{\partial r}, \quad (5.7)$$

$$\frac{\partial B_z}{\partial t} = \frac{B_0}{r} \frac{\sin 2\varphi}{L} \frac{\partial (v_z r^2)}{\partial r}, \quad (5.8)$$

$$\frac{\partial \rho}{\partial t} + \frac{1}{r} \frac{\partial (r \rho_0 v_r)}{\partial r} = 0. \quad (5.9)$$

Combining equations (5.4) and (5.7) we obtain:

$$\frac{\partial^2 B_\varphi}{\partial t^2} = \frac{C_{A0}^2}{L^2} \frac{\partial}{\partial r} \left(r \frac{\partial}{\partial r} (r B_\varphi) \right), \quad (5.10)$$

where C_{A0} is the background Alfvén speed with no dependency on r . Note that when the radial distance of the wave r is equal to the characteristic length L , we have

$$C_{A0} = C_A(r). \quad (5.11)$$

By assuming

$$\bar{r} = \frac{r}{L}, \bar{B}_\varphi = \frac{B_\varphi}{B_0}, \bar{t} = \frac{t C_{A0}}{L}; \quad (5.12)$$

we have the normalised form of equation (5.10) as:

$$\frac{\partial^2 B_\varphi}{\partial \bar{t}^2} = \frac{\partial}{\partial \bar{r}} \left(\bar{r} \frac{\partial}{\partial \bar{r}} (\bar{r} B_\varphi) \right), \quad (5.13)$$

where we have omitted the overline. The solution for the perturbations of the azimuthal magnetic field is:

$$B_\varphi = \frac{1}{r} (F(t - \ln r) + Q(t + \ln r)), \quad (5.14)$$

where functions F and Q describe the shape of the inwardly and outwardly propagating waves, respectively [Craig and McClymont, 1991]. Since we are considering the magnetoacoustic wave propagating towards the null-point we are only interested in the first term of expression (5.14) which shows the incoming wave. Since we work in the zero- β approximation, this model is valid at some distance from the null-point only, far from the radius of β being unity. It is seen that the perturbations of the magnetic field propagates independently of the polar angle φ . Combining equations (5.3) and (5.14) and normalising the radial velocity as $\bar{v}_r = v_r / C_{A0}$ where we again

omit the overtilde, the solution for the normalised radial velocity in the inwardly propagating wave is

$$v_r = \frac{\cos 2\varphi}{r} F(t - \ln r). \quad (5.15)$$

Later in this Chapter in subsection 5.4.4, this solution is compared with the nonlinear numerical plots for different wave amplitudes, showing its time evolution as the wave approaches the null-point.

5.3.2 Nonlinear approach

Consider weakly nonlinear fast waves approaching the null-point. Restricting ourselves to the analysis of the quadratically nonlinear effects only, we obtain

$$\begin{aligned} \frac{\partial^2 B_\varphi}{\partial t^2} - \frac{C_A^2}{L^2} \frac{\partial}{\partial r} \left(r \frac{\partial}{\partial r} (r B_\varphi) \right) = \\ \frac{\partial}{\partial t} N_5 + \frac{B_0}{\mu \rho_0 L} \sin(2\varphi) \frac{\partial}{\partial r} (r N_2) - \frac{B_0}{\mu \rho_0 L} \cos(2\varphi) \frac{\partial}{\partial r} (r N_1), \end{aligned} \quad (5.16)$$

where the quadratic nonlinear terms N_1 , N_2 , and N_5 have been added to the RHS of equations (5.3), (5.4). and (5.7) respectively. The expressions for the nonlinear terms are

$$N_1 = -\mu \rho \frac{\partial}{\partial t} v_r - \frac{B_\varphi}{r} \frac{\partial}{\partial r} (r B_\varphi) - \mu \rho_0 v_r \frac{\partial}{\partial r} v_r + \mu \rho_0 \frac{v_\varphi^2}{r}, \quad (5.17)$$

$$N_2 = -\mu \rho \frac{\partial}{\partial t} v_\varphi - \mu \rho_0 v_r \frac{\partial}{\partial r} v_\varphi - \mu \rho_0 \frac{v_r v_\varphi}{r}, \quad (5.18)$$

$$N_5 = -\frac{\partial}{\partial r} (v_r B_\varphi). \quad (5.19)$$

We change the frame of reference using the linear solution (equation (5.14))

$$\frac{t C_A}{L} - \ln \left(\frac{r}{L} \right) = \xi, \quad \tau = \epsilon t, \quad (5.20)$$

where ϵ is a small parameter which represents the smallness of the nonlinear terms in equation (5.16), meaning that τ is slow time. Equation (5.16) in the new frame

of reference is

$$\frac{\partial B_\varphi}{\partial \tau} - \frac{3 \cos(2\varphi)}{2 L \sqrt{\mu \rho_0}} \exp(\xi) B_\varphi \frac{\partial B_\varphi}{\partial \xi} = 0. \quad (5.21)$$

Equation (5.21) is similar to equation (52) of Nakariakov et al. [2000a] which is a Burgers type equation without the dissipative term. The dependence on the polar angle φ shows that the nonlinear effects affect different polar-angle segments of the inwardly propagating fast pulse differently. The strongest nonlinear effects appear for the polar angles where the pulse propagates across the magnetic field. The quadratically nonlinear terms vanish when the wave propagates along the separatrices, where the wave vector is parallel to the magnetic field, as in this case the fast wave degenerates into the Alfvén wave which is not subject to quadratic nonlinearity and the cubically nonlinear terms should be taken into account. But, most importantly, the dependence of the nonlinear coefficient on the azimuthal angle in equation (5.21) makes the further analytical approach impossible. Since, equation (5.21) was derived under the assumption that the perturbations of the physical parameters are independent of the angle ($\partial/\partial\varphi = 0$). However, equation (5.21) gives an important qualitative information about the azimuthal dependence of the fast wave evolution, which can be used for the understanding of numerical results. This encourages us to treat the problem numerically, in the following we choose to solve numerically the full set of MHD equations which is more robust, rather than the approximated equation (5.21). The study in the next section is based on the numerical study of the ideal MHD equations.

5.4 Numerical study

5.4.1 Numerical methods

The MHD equations (1.16)-(1.19) are solved numerically using the Lagrangian-remap code, Lare2d [Arber et al., 2001]. Lare2d operates by taking a Lagrangian predictor-corrector time step, after each Lagrangian step all variables are conservatively re-mapped back onto the original Eulerian grid using Van Leer gradient limiters. The code was designed for the simulation of nonlinear dynamics of low- β plasmas with steep gradients and hence, suits the problem of interest very well.

The magnetic field \mathbf{B} is defined on cell faces and is updated with a constrained transport to keep $\nabla \cdot \mathbf{B} = 0$ to machine precision. In our studies we simulate the plasma

Table 5.1: Parameters of the initial numerical equilibrium. The values are for typical coronal conditions.

ρ_0 [kg/m ³]	B_0 [T]	T_0 [K]	C_s [Mm/s]	C_A [Mm/s]	β
10^{-12}	10^{-3}	$6 \cdot 10^5$	0.129	0.892	0.025

dynamics in a domain $(0, 10) \times (0, 10)$ Mm covered by 3000×3000 grid points. We performed grid convergence studies to check the numerical results. Zero gradient boundary conditions have been set for all simulations, which allows a propagating perturbation signal leave freely, without reflection.

5.4.2 Initial setup

Our configuration is a simple 2D null-point model with a fast magnetoacoustic pulse on the (x, y) plane initialised at some distance from the null-point. Our choice of the equilibrium magnetic field is

$$\mathbf{B} = B_0[x/L, -y/L, 0], \quad (5.22)$$

c.f. equation (5.1), where B_0 is strength of the magnetic field and L is a characteristic length scale for magnetic field variations. Configuration of the magnetic field lines is illustrated in Figure 5.1. The initial fast magnetoacoustic pulse is circular as in McLaughlin et al. [2009] and is initiated in the region $r_1 < \sqrt{x^2 + y^2} < r_1 + r_0$:

$$V_x = A_0 \sin \left(\pi \frac{\sqrt{x^2 + y^2} - r_1}{r_0} \right) \frac{B_y}{B_x^2 + B_y^2}, \quad (5.23)$$

$$V_y = -A_0 \sin \left(\pi \frac{\sqrt{x^2 + y^2} - r_1}{r_0} \right) \frac{B_x}{B_x^2 + B_y^2}, \quad (5.24)$$

where the amplitude has been taken $A_0 = 10^3$ m/s, with $r_1 = 5$ Mm and $r_0 = 1$ Mm. The specific quantitative values of the initial equilibrium are taken to be consistent with the typical parameters of the solar coronal plasma (see Table 5.1).

5.4.3 Phase relations in magnetoacoustic modes

It is instructive to consider fast magnetoacoustic waves propagating in a uniform medium penetrated by a straight and uniform magnetic field. Consider the equilibrium magnetic field in the z -direction B_{z0} and a plane wave propagating in the x -direction with no dependencies on other components ($\partial/\partial y = 0, \partial/\partial z = 0$) in the zero- β limit. Hence the linearised MHD equations around the equilibrium are

$$\frac{\partial}{\partial t} B_x = 0, \quad \frac{\partial}{\partial t} B_y = 0, \quad \rho_0 \frac{\partial}{\partial t} v_y = 0, \quad \rho_0 \frac{\partial}{\partial t} v_z = 0, \quad (5.25)$$

$$\begin{aligned} \frac{\partial}{\partial t} B_z &= -B_{z0} \frac{\partial}{\partial x} v_x, \\ \rho_0 \frac{\partial}{\partial t} v_x &= -\frac{1}{\mu} B_{z0} \frac{\partial}{\partial x} B_z, \\ \frac{\partial}{\partial t} \rho &= -\rho_0 \frac{\partial}{\partial x} v_x, \end{aligned} \quad (5.26)$$

applying the Fourier decomposition ($\partial/\partial x = ik, \partial/\partial t = i\omega$) of the expressions in equation (5.26), we obtain

$$\frac{B_z}{B_{z0}} = \frac{\rho}{\rho_0}, \quad (5.27)$$

and

$$\frac{B_z}{B_{z0}} = -\frac{\omega}{k} \frac{v_x}{C_{A0}^2}. \quad (5.28)$$

Equations (5.27) and (5.28) are the relations between the perturbations of different physical quantities, which show that the perturbations are related to each other by the phase speed (which in the considered case is just C_{A0}). Hence the direction of the wave propagation would affect the phase relations between the perturbations of the physical parameters like density and velocity. To illustrate this, it is worth reproducing the results of McLaughlin et al. [2009], where a fast magnetoacoustic pulse runs toward the null-point. The results of the simulation are shown in Figure 5.2. The top left and middle panels show the v_x and v_y profiles respectively, and the top right panel shows the initial density perturbation which is blank in $t = 0$ s. The arrows show the direction of the initial velocity profile, and the blue and red colours indicate the negative and positive signs, respectively. The opposite signs

of the perturbations are showing their effects in the bottom row, each panel shows the ingoing and outgoing pulses at $t = 8$ s where the radial shape of the pulse and density perturbation has been deformed to an elliptical shape by the nonlinearity.

This could also be explained in the linear regime by Figure 5.2 and equations

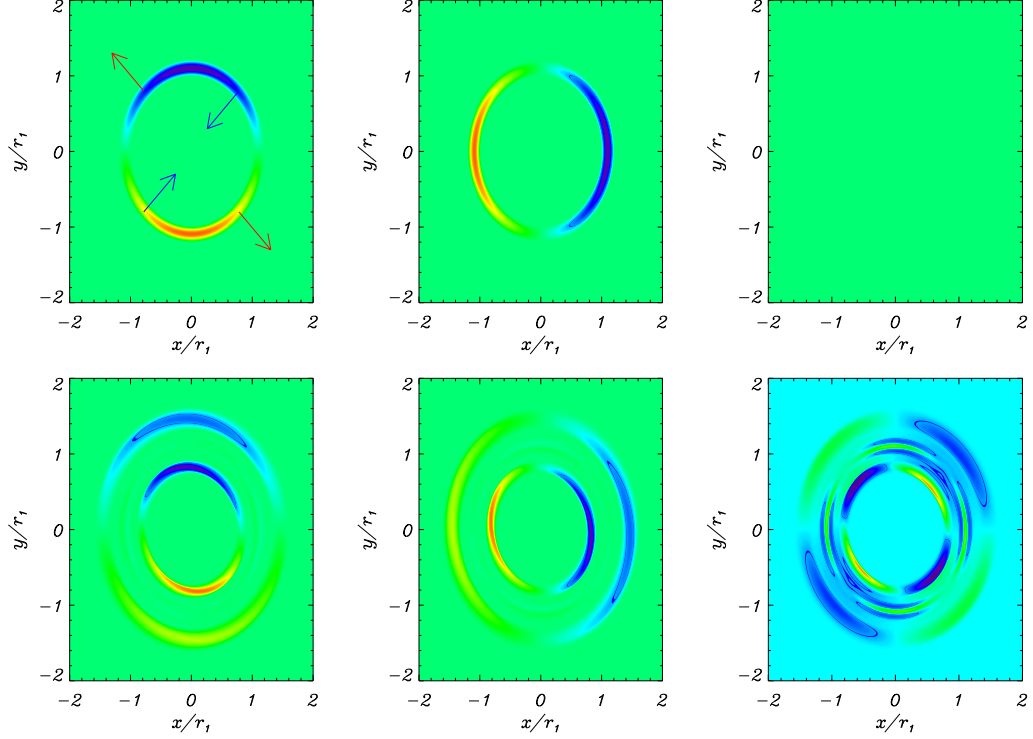


Figure 5.2: Top row, contours of the parameters v_x , v_y , and ρ at $t = 0$ and bottom row, the corresponding parameters at $t = 0.8$ s. The arrows on the top left figure show the initial velocity profile. The red and blue colours in the figures indicate positive and negative signs respectively. In the bottom row the ingoing and outgoing pulses could be seen.

5.27 and 5.28; from the first two top panels of Figure 5.2 it could be noticed that the direction of the velocity perturbation is outward for the second and fourth quarters and inward for the first and third quarters. From the phase relations obtained in equations (5.27) and (5.28) which shows the dependency of the density perturbation on the direction of the velocity through the magnetic field perturbation, the density perturbation is anti-phase in quarters 1 and 3 compared to quarters 2 and 4. Hence we experience the antisymmetry of the density perturbation seen in Figure 5.2 and McLaughlin et al. [2009]. This antisymmetry explains the backward and

front overturn of different segments of the wave-top seen in McLaughlin et al. [2009]. Hence, the density perturbation has azimuthal dependency and is not propagating with the azimuthal wave number $m = 0$, meaning that the perturbation of the radial speed would also depend on the angle and is not an $m = 0$ mode, but an $m = 2$ mode.

5.4.4 Parametric studies

We performed a series of numerical experiments, in order to study the generation of fast magnetoacoustic shocks in the vicinity of a null-point. Figure 5.3 demonstrates the consistency of the numerical results, as they reproduce the analytical solution given by equation (5.15). Also, it shows the departure of the nonlinear results from the linear solution, as the wave amplitude grows. This means that the pulse speed towards the null-point is proportional to the wave initial amplitude, with higher amplitude pulses having higher speeds.

Figure 5.4 shows contour plots of velocity at four different instants of time. We

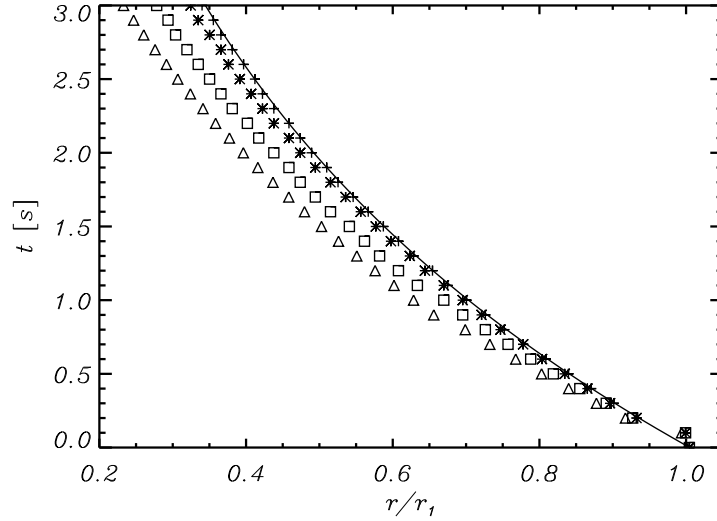


Figure 5.3: Comparison of numerical results simulating incoming fast magnetoacoustic waves of different amplitude with the analytical solution equation (5.15). Solid line (points) corresponds to analytical (numerical) solution. Amplitude of initial pulse was A_0 for triangles, $0.5A_0$ for squares $0.1A_0$ for stars and $0.01A_0$ for crosses. The spatial coordinate is measured in units of r_1 .

show only the region $(x > 0, y > 0)$ of the simulation. The white curve shows the position of the linear solution. It is clearly visible and was illustrated in subsection 5.4.3 that the pulse begins to change from circular to an elliptical shape, due to the dependence of the nonlinear coefficient upon the azimuthal angle.

Figure 5.5 displays the radial velocity of the pulse

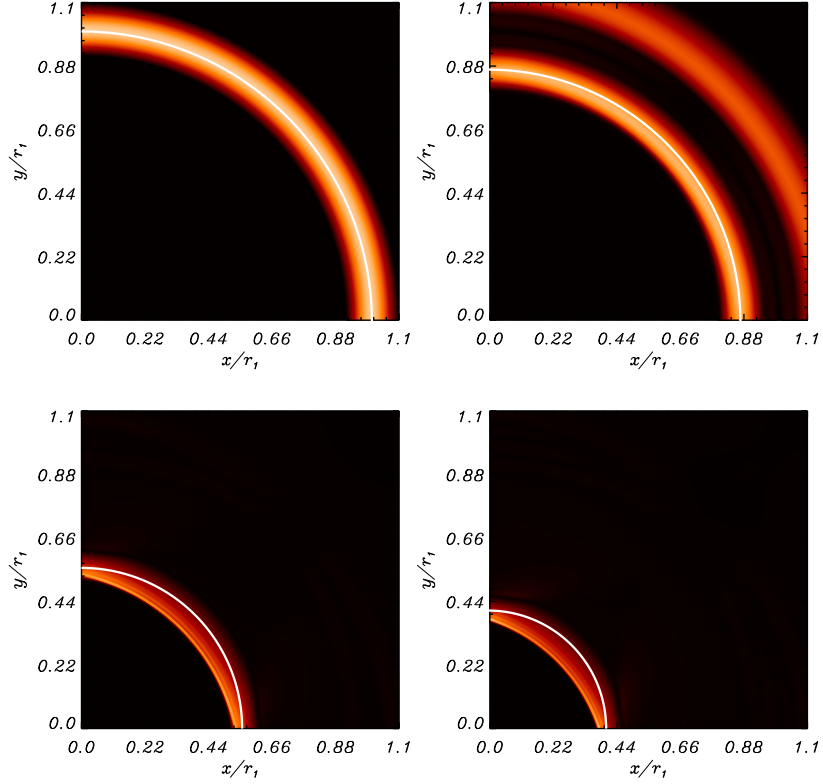


Figure 5.4: Two dimensional plots of the radial velocity $V_r = \sqrt{V_x^2 + V_y^2}$ at $t=0$ s (top left panel), $t=0.4$ s, (top right panel), $t=1.6$ s, (bottom left panel), and $t=2.4$ s (bottom right panel). White curves show the linear solution. The spatial coordinates are measured in units of r_1 that is the initial position of the fast wave-pulse.

$$V_r = \sqrt{V_x^2 + V_y^2} \quad (5.29)$$

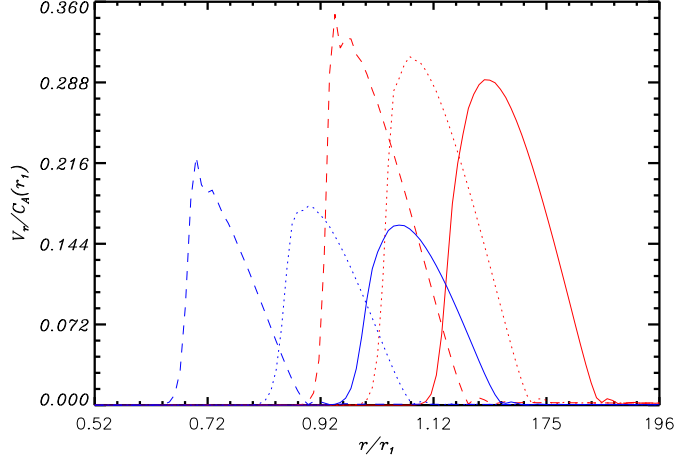


Figure 5.5: Perturbations of the radial velocity in the inwardly propagating pulse, $V_r = \sqrt{V_x^2 + V_y^2}$ as a function of the radial position r . Different colours correspond to two different initial amplitudes of the pulse. Different lines correspond to different times: $t = 0.4$ s (solid red line), $t=0.6$ s (dotted red line), $t=0.8$ s (dashed red line), $t=0.7$ s (solid blue line), $t=1.0$ s (dotted blue line), and $t=1.4$ s (dashed blue line) respectively. The radial coordinate is measured in units of r_1 .

versus the radius r at three instants of time. The blue and red profiles correspond to two different amplitudes. It is clearly visible that the higher amplitude pulse “overtakes” - forms the shock - faster than the smaller amplitude pulse. In addition, the radial velocity is accompanied by current density spikes [McLaughlin and Hood, 2004] as the wave amplitude increases in time, which gives rise for anomalous resistivity (see subsection 1.6.5). This is shown in the three snapshots of Figure 5.6.

In order to estimate the position of the shock formation we calculated the derivative of velocity. When the radial derivative of the velocity exceeds the threshold value (about 100), we assume that shock appears. We observe that the gradient in a narrow pulse is higher than for a wider pulse, thus the shock should create faster.

Figure 5.7 illustrates the dependence of the shock formation distance from the null-point on the initial width and amplitude of the pulse. The left panel shows the shock generation for different amplitudes of the initial pulse for all other parameters

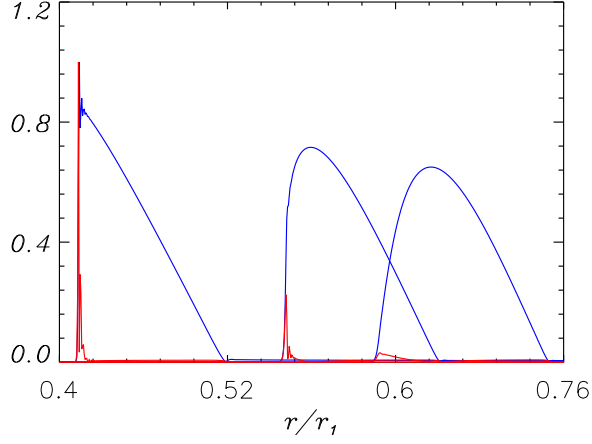


Figure 5.6: Perturbations of the radial velocity in the inwardly propagating pulse, $V_r = \sqrt{V_x^2 + V_y^2}$ as a function of the radial position r . The spikes (red spikes) correspond to the current density j and the blue curves correspond to v_r at times $t = 0.4$ s, $t = 0.7$ s, $t = 1.4$ s. The parameters are normalised by the maximum values of v_r and t at $t = 1.4$ s, and the radial coordinate is measured in units of r_1 .

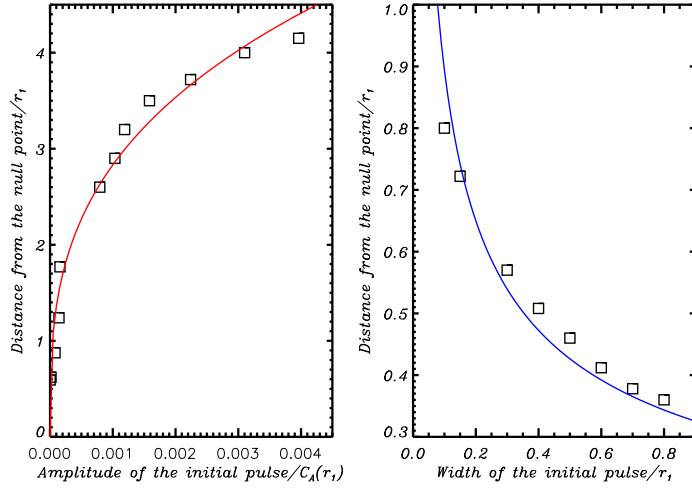


Figure 5.7: Distance from the null-point to the position of the fast shock formation as a function of the amplitude of initial pulse (left panel) and width of initial pulse (right panel). We fit two curves into the points, red curve $25.82x^{0.32}$ and blue curve $0.31x^{-0.46}$. Spatial coordinates and amplitude are measured in units of r_1 and Alfvén speed $C_A(r_1)$.

of the run fixed. The right panel shows the shock generation in respect to the initial width of the pulse. The spatial coordinates are normalised by the initial distance of the pulse from the null-point r_1 , and the velocity amplitude is normalised by the local Alfvén speed. It could be seen that higher amplitude pulses generate shocks further away from the null-point, while pulses with larger width form the shock closer to the null-point.

5.5 Summary and discussion

We have performed an analytical study accompanied by numerical simulations of the behaviour of a fast magnetoacoustic pulse as approaching a null-point. Using ideal MHD equations in the zero- β regime (hence, at some sufficiently large distance from the radius $\beta = 1$), we developed a 1D analytical model of an initially radially symmetric fast pulse in the weakly nonlinear regime. We showed the expression for the radial velocity of the fast magnetoacoustic pulse and obtained that the evolution of the pulse leads to the departure from the azimuthally symmetric $m = 0$ mode, but is rather of the symmetry of the $m = 2$ mode. Consideration of the excitation conditions and of the phase relations in the numerical experiments of McLaughlin et al. [2009] supported that observation. Numerical simulations confirmed the azimuthal dependency of the fast magnetoacoustic pulse for a quarter of a circle justifying our analytical explanation for the $m = 2$ mode. Also in our simulations we showed that small amplitudes pulses coincide with the linear analytical solution of Craig and McClymont [1991]. In addition, it was shown that waves of higher initial amplitudes propagate faster.

Moreover, our numerical studies of a fast wave evolution in the vicinity of a magnetic null-point showed that not only the initial amplitude is responsible for the time that the pulse overturns, but also the initial width of the pulse is responsible. Thus, initially lower amplitude and broader fast wave-pulses form fast shocks - “overturn” - closer to the null-point. As the shock formation is accompanied by the generation of electric current density spikes, in the vicinity of the shock formation region we can expect onset of plasma micro-turbulence, and hence appearance of anomalous electrical resistivity.

Our finding has interesting implications to the problem of sympathetic flares (see subsection 1.6.5 and references therein). It was shown that as the amplitude of the

initial pulse increases the overturning takes place further away from the null-point and as the width of the pulse increases the overturning takes place at a closer distance to the null-point having more effect. In other words, only wider and small amplitude pulses can reach magnetic null-point before overturning and ignite magnetic reconnection. Narrower and high amplitude pulses overturn quicker and do not reach the null-point and hence cannot ignite magnetic reconnection. The shock is accompanied with a spike of current density; hence anomalous resistivity can be generated (subsection 1.6.5).

Without accounting for this effect, the physical picture of the phenomenon of sympathetic flares is incomplete. Indeed, for the effective ignition of a “daughter” flare by a “mother” flare, the triggering fast wave should be of the right initial amplitude and width. Hence, more powerful “mother” flares do not necessarily have higher probability to ignite a “daughter” flare. Similarly, the probability of the excitation of a “daughter” flare is not inversely proportional to the distance between the sites of the “mother” and “daughter” flares.

Chapter 6

Conclusions

In this thesis we performed a theoretical study of the dynamics of MHD waves in structured plasmas of the solar corona, and used the theoretical results for interpretation of recent solar observations, and prediction of new physical effects.

In Chapter 2 we demonstrated that transverse waves observed in soft X-ray solar coronal jets [Cirtain et al., 2007] are adequately described in terms of fast magnetoacoustic kink ($m = 1$) modes of a straight magnetic cylinder embedded in a magnetic environment. It was shown that these waves are collective, since they are coherent perturbations of all magnetic surfaces inside the jet, and compressible, since the flow-perturbation divergence is finite. Phase and group speeds were determined by the density contrast of the jet, the flow speed, and the internal and external Alfvén speeds. Forward modelling performed with the use of theoretically determined phase relations was found to be consistent with the observational findings obtained with Hinode/XRT.

The expressions written in Chapter 2 were obtained for the azimuthal mode number $m = 1$. However, we pointed out that a transverse displacement of the axis of the cylinder, such as the transverse motion of the jet, can, in general, have two opposite senses, $m = \pm 1$. The azimuthal modes $m = \pm 1$ manifest themselves as a cork-screwing motion travelling along the cylinder. However, it is impossible to distinguish observationally between a pure $m = \pm 1$ mode or a superposition of these modes. As such, it is only possible to measure the projected motion of the jet. It is impossible to quantify the motion in the other direction and thus to assess the nature (pure or superposition) of the observed oscillation.

If there is a variation in the Alfvén or flow speed across the jet, the kink perturba-

tions are subject to resonant absorption. The damping time of the kink oscillations in a jet for typical coronal parameters was estimated to be several times longer than the wave period which is consistent with observations. It is unclear how the wave evolves past the physical extent of the jet, which will depend on the transverse structuring that is not visible in the observations.

It was shown in Chapter 2 that although the origin of transverse oscillations of soft X-ray jets could possibly be due to the Kelvin-Helmholtz instability, but it is not consistent with the observations. For a plasma structure of the observed geometry with the typical values of the Alfvén speed and the density contrast, the instability threshold value of the steady flow speed is a few times greater than the internal Alfvén speed. Since the observed values of the jet speeds do not exceed the Alfvén speed inside the jet, the instability threshold is not reached and this possibility should be excluded.

Also, in Chapter 2 we pointed out that the other candidate for the origin of transverse oscillations, which is related to negative energy wave instabilities is also not the case. According to Joarder et al. [1997] in the considered situation, sub-Alfvénic flow speeds can lead to the instability of longitudinal modes only, which does not explain the generation of the transverse perturbations. Also, the periodicity could appear because of geometric dispersion [Roberts et al., 1984; Murawski and Roberts, 1994]. However, the typical wavelength generated by this mechanism would be comparable to the jet diameter and hence we exclude this option too. Consequently, we deduced that the observed transverse waves are excited somewhere at the origin of the jet, possibly by oscillatory magnetic reconnection [Murray et al., 2009], and then propagate according to the dispersion and phase relations discussed in Chapter 2.

Observation of transverse waves guided by soft X-ray jets is interesting for coronal seismology. Since, the phase speed of the waves obtained in Chapter 2 were in terms of the flow speed and the Alfvén speed inside the jet. Also the density ratio of the internal and external medium showed that there is a constraint given by the equilibrium condition, where we have assumed that the external β is very small and $\gamma = 5/3$. These expressions contain observables: the phase speed of transverse waves, the flow speed [Cirtain et al., 2007], the density-contrast ratio (which can be obtained from the emission-measure contrast) and the sound speed (which is connected with the temperature). The use of the observed values in the theoretical constraints allows us to estimate the internal and external Alfvén speeds, and the

magnetic fields.

In Chapter 3, torsional axisymmetric ($m=0$) long-wavelength MHD modes of a cylindrical plasma structure were studied with the use of the second-order thin flux tube approximation. The approximation and model could be used to describe various plasma structures in the corona of the Sun, e.g. coronal jets and plumes, as well as segments of coronal loops and filaments.

The general dispersion relation obtained in Chapter 3 is a sixth order polynomial which describes all three MHD modes of the $m = 0$ symmetry: the torsional, sausage fast magnetoacoustic and longitudinal (slow magnetoacoustic) modes. In the untwisted non-rotating flux tube, sausage and longitudinal modes are dispersive. We stressed that in the untwisted limit the proper treatment of these waves requires consideration of the external medium, while in the twisted case considered here the equilibrium does not necessarily require the presence of the external plasma. In any case, both sausage and longitudinal modes are compressible and hence magnetoacoustic. In the untwisted non-rotating case, the torsional mode is dispersionless, and hence is the true Alfvén wave.

It was shown that the equilibrium twist and rotation of the tube modifies the torsional mode making it dispersive. Assuming the dispersion being weak, we derived asymptotic dispersion relations for the phase speeds of the modes. Interestingly, it was shown that the phase speeds of the torsional waves propagating in the opposite directions along the tube have different absolute values, which is connected with the local Doppler shift. In twisted magnetic flux tubes torsional waves become compressible, perturbing the plasma density, the absolute value of the magnetic field, and the tube cross-section. The induced variations of the plasma density and the absolute value of the magnetic field are in phase with the variations of the twist in the torsional wave, and in anti-phase with the variations of the loop radius. The compressibility vanishes in the limit when the equilibrium twist goes to zero, as it should be in the familiar case of the straight magnetic field.

Using the observations by Cirtain et al. [2007] for physical parameters in hot coronal jets, we see that the corona could be taken as a cold plasma region and according to equation (3.47), a torsional wave of the relative amplitude 10 percent will be accompanied by a density perturbation of about 7 percent. Our results in Chapter 3 provides theoretical basis for the search for torsional waves in coronal plasma structures, and, in particular, for the forward modelling of the EUV, soft X-ray and microwave observables.

In straight untwisted and non-rotating magnetic flux tubes, long-wavelength torsional waves could induce compressible perturbations by the ponderomotive, centrifugal and magnetic twist forces. The perturbations have double the frequency of the inducing torsional wave. The efficiency of the excitation depends upon the spatial (standing and propagating) structure of the inducing torsional wave. The efficiency of the generation of compressible perturbations by long-wavelength torsional waves is independent of the plasma- β . This result is different from the excitation of compressible perturbations by plane shear Alfvén waves, in which case the efficiency grows when the Alfvén and sound speeds approach each other. The discrepancy is connected with the fact that the tube speed, which is the speed of the longitudinal mode in a flux tube, is always lower than the Alfvén speed. The relative amplitude of the induced density perturbation was obtained in Chapter 4.

In addition, in Chapter 4 it was shown that there are two kinds of compressible perturbations induced by standing torsional waves: the perturbations which grow with the time scale $1/(2C_s k)$, where k is the longitudinal wave number of the torsional wave, and the perturbations oscillating at the double frequency of the driving torsional mode. The growing density perturbations saturate at the level inversely proportional to the sound speed.

Thus we conclude that nonlinear compressible effects which accompany standing weakly-nonlinear long-wavelength torsional waves are similar to those derived for plane shear Alfvén waves. For propagating waves, the efficiency of the nonlinear generation of compressible perturbations does not grow with the plasma- β . This effect should be taken into account in one-dimensional models of the solar and stellar wind acceleration by Alfvén waves.

In Chapter 5 it was shown that although the amplitude of the initial fast magnetoacoustic pulse propagating towards a magnetic null-point, affects the shock formation position, but the width of the initial pulse needs to be considered too. It was shown that as the initial width of the pulse gets larger the pulse manages to get closer to the null-point and could cause ignition of magnetic reconnection. The results of Chapter 5 could be important for sympathetic flares, as having a stronger pulse does not mean the effects would be greater. It was shown that large amplitude pulses never get closer to the null-point and overturn very quickly compared to lower amplitude pulses. Hence, waves with lower amplitudes and larger width could overturn closer to the null-point, and seed there the anomalous resistivity, which can trigger fast reconnection. In nature this phenomena could be observed in a tsunami which

it has much more effects than an ordinary wave since the wavelength of the tsunami is much larger than the wavelength of an ordinary storm wave.

Bibliography

- M. Abramowitz, I. A. Stegun, and R. H. Romer. Handbook of Mathematical Functions with Formulas, Graphs, and Mathematical Tables. *American Journal of Physics*, 56:958–958, October 1988. doi: 10.1119/1.15378.
- D. Alexander and L. Fletcher. High-resolution Observations of Plasma Jets in the Solar Corona. *Sol. Phys.*, 190:167–184, December 1999. doi: 10.1023/A:1005213826793.
- P. Antolin and K. Shibata. The Role Of Torsional Alfvén Waves in Coronal Heating. *ApJ*, 712:494–510, March 2010. doi: 10.1088/0004-637X/712/1/494.
- P. Antolin, K. Shibata, T. Kudoh, D. Shiota, and D. Brooks. Predicting Observational Signatures of Coronal Heating by Alfvén Waves and Nanoflares. *ApJ*, 688: 669–682, November 2008. doi: 10.1086/591998.
- T. D. Arber, A. W. Longbottom, C. L. Gerrard, and A. M. Milne. A Staggered Grid, Lagrangian-Eulerian Remap Code for 3-D MHD Simulations. *Journal of Computational Physics*, 171:151–181, July 2001. doi: 10.1006/jcph.2001.6780.
- A. Asai, M. Shimojo, H. Isobe, T. Morimoto, T. Yokoyama, K. Shibasaki, and H. Nakajima. Periodic Acceleration of Electrons in the 1998 November 10 Solar Flare. *ApJ*, 562:L103–L106, November 2001. doi: 10.1086/338052.
- M. J. Aschwanden. *Physics of the Solar Corona. An Introduction with Problems and Solutions (2nd edition)*. December 2005.
- M. J. Aschwanden, L. Fletcher, C. J. Schrijver, and D. Alexander. Coronal Loop Oscillations Observed with the Transition Region and Coronal Explorer. *ApJ*, 520:880–894, August 1999.

- D. Banerjee, D. Pérez-Suárez, and J. G. Doyle. Signatures of Alfvén waves in the polar coronal holes as seen by EIS/Hinode. *A&A*, 501:L15–L18, July 2009. doi: 10.1051/0004-6361/200912242.
- G. S. Bisnovatyi-Kogan. Dynamic confinement of jets by magnetotorsional oscillations. *MNRAS*, 376:457–464, March 2007. doi: 10.1111/j.1365-2966.2007.11452.x.
- G. J. J. Botha, T. D. Arber, V. M. Nakariakov, and F. P. Keenan. A developed stage of Alfvén wave phase mixing. *A&A*, 363:1186–1194, November 2000.
- T. J. M. Boyd and J. J. Sanderson. *The Physics of Plasmas*. February 2003.
- D. S. Brown and E. R. Priest. The topological behaviour of 3D null points in the Sun’s corona. *A&A*, 367:339–346, February 2001. doi: 10.1051/0004-6361:20010016.
- J. Büchner. Astrophysical reconnection and collisionless dissipation. *Plasma Physics and Controlled Fusion*, 49:325–+, December 2007. doi: 10.1088/0741-3335/49/12B/S30.
- J. Büchner and N. Elkina. Vlasov Code Simulation of Anomalous Resistivity. *Space Sci. Rev.*, 121:237–252, November 2005. doi: 10.1007/s11214-006-6542-6.
- J. Büchner and N. Elkina. Anomalous resistivity of current-driven isothermal plasmas due to phase space structuring. *Physics of Plasmas*, 13(8):082304–+, August 2006. doi: 10.1063/1.2209611.
- R. A. Cairns. The role of negative energy waves in some instabilities of parallel flows. *Journal of Fluid Mechanics*, 92:1–14, May 1979.
- P. S. Cally. Note on an Exact Solution for Magnetoatmospheric Waves. *ApJ*, 548:473–481, February 2001. doi: 10.1086/318675.
- P. Charbonneau and K. B. MacGregor. Stellar Winds with Non-WKB Alfvén Waves. II. Wind Models for Cool, Evolved Stars. *ApJ*, 454:901–+, December 1995. doi: 10.1086/176543.
- J. W. Cirtain, L. Golub, L. Lundquist, A. van Ballegooijen, A. Savcheva, M. Shimojo, E. DeLuca, S. Tsuneta, T. Sakao, K. Reeves, M. Weber, R. Kano, N. Narukage, and K. Shibasaki. Evidence for Alfvén Waves in Solar X-ray Jets. *Science*, 318:1580–, December 2007.

- R. H. Cohen and R. M. Kulsrud. Nonlinear evolution of parallel-propagating hydromagnetic waves. *Physics of Fluids*, 17:2215–2225, December 1974. doi: 10.1063/1.1694695.
- F. C. Cooper, V. M. Nakariakov, and D. R. Williams. Short period fast waves in solar coronal loops. *A&A*, 409:325–330, October 2003.
- P. Copil, Y. Voitenko, and M. Goossens. Torsional Alfvén waves in small scale density threads of the solar corona. *A&A*, 478:921–927, February 2008. doi: 10.1051/0004-6361:20078481.
- I. J. Craig and P. G. Watson. Fast dynamic reconnection at X-type neutral points. *ApJ*, 393:385–395, July 1992. doi: 10.1086/171512.
- I. J. D. Craig and A. N. McClymont. Dynamic magnetic reconnection at an X-type neutral point. *ApJ*, 371:L41–L44, April 1991. doi: 10.1086/185997.
- S. R. Cranmer. Coronal Holes. *Living Reviews in Solar Physics*, 6:3–+, September 2009.
- S. R. Cranmer and A. A. van Ballegoijen. On the Generation, Propagation, and Reflection of Alfvén Waves from the Solar Photosphere to the Distant Heliosphere. *ApJS*, 156:265–293, February 2005. doi: 10.1086/426507.
- L. Culhane, L. K. Harra, D. Baker, L. van Driel-Gesztelyi, J. Sun, G. A. Doschek, D. H. Brooks, L. L. Lundquist, S. Kamio, P. R. Young, and A. H. Hansteen. Hinode EUV Study of Jets in the Sun’s South Polar Corona. *PASJ*, 59:751–+, November 2007.
- I. de Moortel. Longitudinal Waves in Coronal Loops. *Space Sci. Rev.*, 149:65–81, December 2009. doi: 10.1007/s11214-009-9526-5.
- I. De Moortel, J. Ireland, R. W. Walsh, and A. W. Hood. Longitudinal intensity oscillations in coronal loops observed with TRACE I. Overview of Measured Parameters. *Sol. Phys.*, 209:61–88, September 2002. doi: 10.1023/A:1020956421063.
- B. De Pontieu, S. W. McIntosh, M. Carlsson, V. H. Hansteen, T. D. Tarbell, C. J. Schrijver, A. M. Title, R. A. Shine, S. Tsuneta, Y. Katsukawa, K. Ichimoto, Y. Suematsu, T. Shimizu, and S. Nagata. Chromospheric Alfvénic Waves Strong

- Enough to Power the Solar Wind. *Science*, 318:1574–, December 2007. doi: 10.1126/science.1151747.
- P. M. Edwin and B. Roberts. Wave propagation in a magnetic cylinder. *Sol. Phys.*, 88:179–191, October 1983.
- R. Erdélyi and V. Fedun. Linear MHD Sausage Waves in Compressible Magnetically Twisted Flux Tubes. *Sol. Phys.*, 246:101–118, November 2007. doi: 10.1007/s11207-007-9022-6.
- A. Ferrari, E. Trussoni, and L. Zaninetti. Magnetohydrodynamic Kelvin-Helmholtz instabilities in astrophysics. II Cylindrical boundary layer in vortex sheet approximation. *MNRAS*, 196:1051–1066, September 1981.
- A. Ferriz-Mas, M. Schuessler, and V. Anton. Dynamics of magnetic flux concentrations - The second-order thin flux tube approximation. *A&A*, 210:425–432, February 1989.
- L. Fletcher and H. S. Hudson. Impulsive Phase Flare Energy Transport by Large-Scale Alfvén Waves and the Electron Acceleration Problem. *ApJ*, 675:1645–1655, March 2008. doi: 10.1086/527044.
- C. Foullon, E. Verwichte, V. M. Nakariakov, and L. Fletcher. X-ray quasi-periodic pulsations in solar flares as magnetohydrodynamic oscillations. *A&A*, 440:L59–L62, September 2005. doi: 10.1051/0004-6361:200500169.
- L. Golub, E. Deluca, G. Austin, J. Bookbinder, D. Caldwell, P. Cheimets, J. Cirtain, M. Cosmo, P. Reid, A. Sette, M. Weber, T. Sakao, R. Kano, K. Shibasaki, H. Hara, S. Tsuneta, K. Kumagai, T. Tamura, M. Shimojo, J. McCracken, J. Carpenter, H. Haight, R. Siler, E. Wright, J. Tucker, H. Rutledge, M. Barbera, G. Peres, and S. Varisco. The X-Ray Telescope (XRT) for the Hinode Mission. *Sol. Phys.*, 243: 63–86, June 2007.
- M. Goossens, editor. *An introduction to plasma astrophysics and magnetohydrodynamics*, volume 294 of *Astrophysics and Space Science Library*, October 2003.
- M. Goossens, J. V. Hollweg, and T. Sakurai. Resonant behaviour of MHD waves on magnetic flux tubes. III - Effect of equilibrium flow. *Sol. Phys.*, 138:233–255, April 1992.

- J. T. Gosling, W.-L. Teh, and S. Eriksson. A Torsional Alfvén Wave Embedded Within a Small Magnetic Flux Rope in the Solar Wind. *ApJ*, 719:L36–L40, August 2010. doi: 10.1088/2041-8205/719/1/L36.
- V. V. Grechnev, S. M. White, and M. R. Kundu. Quasi-periodic Pulsations in a Solar Microwave Burst. *ApJ*, 588:1163–1175, May 2003. doi: 10.1086/374315.
- R. A. Harrison. Solar soft X-ray pulsations. *A&A*, 182:337–347, August 1987.
- J. Heyvaerts and E. R. Priest. Coronal heating by phase-mixed shear Alfvén waves. *A&A*, 117:220–234, January 1983.
- A. W. Hood, V. Archontis, K. Galsgaard, and F. Moreno-Insertis. The emergence of toroidal flux tubes from beneath the solar photosphere. *A&A*, 503:999–1011, September 2009. doi: 10.1051/0004-6361/200912189.
- A. R. Inglis, T. Van Doorselaere, C. S. Brady, and V. M. Nakariakov. Characteristics of magnetoacoustic sausage modes. *A&A*, 503:569–575, August 2009. doi: 10.1051/0004-6361/200912088.
- D. B. Jess, M. Mathioudakis, R. Erdélyi, P. J. Crockett, F. P. Keenan, and D. J. Christian. Alfvén Waves in the Lower Solar Atmosphere. *Science*, 323:1582–, March 2009. doi: 10.1126/science.1168680.
- P. S. Joarder, V. M. Nakariakov, and B. Roberts. A Manifestation of Negative Energy Waves in the Solar Atmosphere. *Sol. Phys.*, 176:285–297, December 1997.
- K. Kai and A. Takayanagi. Interferometer Observation of Pulsating Sources Associated with a Type IV Solar Radio Burst. *Sol. Phys.*, 29:461–475, April 1973. doi: 10.1007/BF00150826.
- M. L. Khodachenko, V. V. Zaitsev, A. G. Kislyakov, and A. V. Stepanov. Equivalent Electric Circuit Models of Coronal Magnetic Loops and Related Oscillatory Phenomena on the Sun. *Space Science Reviews*, 149:83–117, December 2009. doi: 10.1007/s11214-009-9538-1.
- B. Kliem, M. Karlický, and A. O. Benz. Solar flare radio pulsations as a signature of dynamic magnetic reconnection. *A&A*, 360:715–728, August 2000.
- S. Koutchmy, I. D. Zhugzhda, and V. Locans. Short period coronal oscillations - Observation and interpretation. *A&A*, 120:185–191, April 1983.

- N. P. M. Kuin and P. C. H. Martens. On the thermal stability of hot coronal loops - The coupling between chromosphere and corona. *A&A*, 108:L1–L4, April 1982.
- C. Litwin and R. Rosner. Coronal Scale-Height Enhancement by Magnetohydrodynamic Waves. *ApJ*, 506:L143–L146, October 1998. doi: 10.1086/311656.
- D. W. Longcope. Topological Methods for the Analysis of Solar Magnetic Fields. *Living Reviews in Solar Physics*, 2:7–+, November 2005.
- D. W. Longcope and E. R. Priest. Fast magnetosonic waves launched by transient, current sheet reconnection. *Physics of Plasmas*, 14(12):122905–+, December 2007. doi: 10.1063/1.2823023.
- R. Lundin and A. Guglielmi. Ponderomotive Forces in Cosmos. *Space Sci. Rev.*, 127:1–116, December 2006. doi: 10.1007/s11214-006-8314-8.
- J. A. McLaughlin and A. W. Hood. MHD wave propagation in the neighbourhood of a two-dimensional null point. *A&A*, 420:1129–1140, June 2004. doi: 10.1051/0004-6361:20035900.
- J. A. McLaughlin and A. W. Hood. Magnetohydrodynamics wave propagation in the neighbourhood of two dipoles. *A&A*, 452:603–613, June 2006. doi: 10.1051/0004-6361:20054575.
- J. A. McLaughlin, I. De Moortel, A. W. Hood, and C. S. Brady. Nonlinear fast magnetoacoustic wave propagation in the neighbourhood of a 2D magnetic X-point: oscillatory reconnection. *A&A*, 493:227–240, January 2009. doi: 10.1051/0004-6361:200810465.
- K. Miyamoto. *Fundamentals of Plasma Physics and Controlled Fusion*. Springer, 2005.
- Y.-J. Moon, G. S. Choe, Y. D. Park, H. Wang, P. T. Gallagher, J. Chae, H. S. Yun, and P. R. Goode. Statistical Evidence for Sympathetic Flares. *ApJ*, 574:434–439, July 2002. doi: 10.1086/340945.
- S. Moriyasu, T. Kudoh, T. Yokoyama, and K. Shibata. The Nonlinear Alfvén Wave Model for Solar Coronal Heating and Nanoflares. *ApJ*, 601:L107–L110, January 2004. doi: 10.1086/381779.

- D. A. N. Müller, H. Peter, and V. H. Hansteen. Dynamics of solar coronal loops. II. Catastrophic cooling and high-speed downflows. *A&A*, 424:289–300, September 2004. doi: 10.1051/0004-6361:20040403.
- K. Murawski and B. Roberts. Time signatures of impulsively generated waves in a coronal plasma. *Sol. Phys.*, 151:305–317, May 1994. doi: 10.1007/BF00679077.
- M. J. Murray, L. van Driel-Gesztelyi, and D. Baker. Simulations of emerging flux in a coronal hole: oscillatory reconnection. *A&A*, 494:329–337, January 2009. doi: 10.1051/0004-6361:200810406.
- V. M. Nakariakov and V. F. Melnikov. Modulation of gyrosynchrotron emission in solar and stellar flares by slow magnetoacoustic oscillations. *A&A*, 446:1151–1156, February 2006. doi: 10.1051/0004-6361:20053944.
- V. M. Nakariakov and V. F. Melnikov. Quasi-Periodic Pulsations in Solar Flares. *Space Science Reviews*, pages 55–+, May 2009. doi: 10.1007/s11214-009-9536-3.
- V. M. Nakariakov and B. Roberts. Magnetosonic Waves in Structured Atmospheres with Steady Flows, I. *Sol. Phys.*, 159:213–228, July 1995a. doi: 10.1007/BF00686530.
- V. M. Nakariakov and B. Roberts. On Fast Magnetosonic Coronal Pulsations. *Sol. Phys.*, 159:399–402, July 1995b. doi: 10.1007/BF00686541.
- V. M. Nakariakov and E. Verwichte. Coronal Waves and Oscillations. *Living Reviews in Solar Physics*, 2:3–+, July 2005.
- V. M. Nakariakov, B. Roberts, and G. Mann. MHD modes of solar wind flow tubes. *A&A*, 311:311–316, July 1996.
- V. M. Nakariakov, L. Ofman, E. E. Deluca, B. Roberts, and J. M. Davila. TRACE observation of damped coronal loop oscillations: Implications for coronal heating. *Science*, 285:862–864, August 1999.
- V. M. Nakariakov, C. A. Mendoza-Briceño, and M. H. Ibáñez S. Magnetoacoustic Waves of Small Amplitude in Optically Thin Quasi-isentropic Plasmas. *ApJ*, 528:767–775, January 2000a. doi: 10.1086/308195.
- V. M. Nakariakov, L. Ofman, and T. D. Arber. Nonlinear dissipative spherical Alfvén waves in solar coronal holes. *A&A*, 353:741–748, January 2000b.

- V. M. Nakariakov, E. Verwichte, D. Berghmans, and E. Robbrecht. Slow magnetoacoustic waves in coronal loops. *A&A*, 362:1151–1157, October 2000c.
- V. M. Nakariakov, V. F. Melnikov, and V. E. Reznikova. Global sausage modes of coronal loops. *A&A*, 412:L7–L10, December 2003. doi: 10.1051/0004-6361:20031660.
- V. M. Nakariakov, T. D. Arber, C. E. Ault, A. C. Katsiyannis, D. R. Williams, and F. P. Keenan. Time signatures of impulsively generated coronal fast wave trains. *MNRAS*, 349:705–709, April 2004a. doi: 10.1111/j.1365-2966.2004.07537.x.
- V. M. Nakariakov, D. Tsiklauri, A. Kelly, T. D. Arber, and M. J. Aschwanden. Acoustic oscillations in solar and stellar flaring loops. *A&A*, 414:L25–L28, January 2004b. doi: 10.1051/0004-6361:20031738.
- V. M. Nakariakov, C. Foullon, E. Verwichte, and N. P. Young. Quasi-periodic modulation of solar and stellar flaring emission by magnetohydrodynamic oscillations in a nearby loop. *A&A*, 452:343–346, June 2006. doi: 10.1051/0004-6361:20054608.
- K. Nishida, M. Shimizu, D. Shiota, H. Takasaki, T. Magara, and K. Shibata. Numerical Examination of Plasmoid-Induced Reconnection Model for Solar Flares: The Relation between Plasmoid Velocity and Reconnection Rate. *ApJ*, 690:748–757, January 2009. doi: 10.1088/0004-637X/690/1/748.
- L. Ofman. Three-fluid model of the heating and acceleration of the fast solar wind. *Journal of Geophysical Research (Space Physics)*, 109:7102–+, July 2004. doi: 10.1029/2003JA010221.
- L. Ofman. MHD Waves and Heating in Coronal Holes. *Space Science Reviews*, 120:67–94, September 2005. doi: 10.1007/s11214-005-5098-1.
- L. Ofman. Wave Modeling of the Solar Wind. *Living Reviews in Solar Physics*, 7:4–+, October 2010.
- L. Ofman and J. M. Davila. Solar wind acceleration by large-amplitude nonlinear waves: Parametric study. *J. Geophys. Res.*, 103:23677–23690, October 1998. doi: 10.1029/98JA01996.
- L. Ofman and T. Wang. Hot Coronal Loop Oscillations Observed by SUMER: Slow Magnetosonic Wave Damping by Thermal Conduction. *ApJ*, 580:L85–L88, November 2002. doi: 10.1086/345548.

- L. Ofman, V. M. Nakariakov, and C. E. Deforest. Slow Magnetosonic Waves in Coronal Plumes. *ApJ*, 514:441–447, March 1999. doi: 10.1086/306944.
- L. Ofman, V. M. Nakariakov, and N. Sehgal. Dissipation of Slow Magnetosonic Waves in Coronal Plumes. *ApJ*, 533:1071–1083, April 2000. doi: 10.1086/308691.
- T. J. Okamoto, S. Tsuneta, T. E. Berger, K. Ichimoto, Y. Katsukawa, B. W. Lites, S. Nagata, K. Shibata, T. Shimizu, R. A. Shine, Y. Suematsu, T. D. Tarbell, and A. M. Title. Coronal Transverse Magnetohydrodynamic Waves in a Solar Prominence. *Science*, 318:1577–, December 2007. doi: 10.1126/science.1145447.
- D. J. Pascoe, V. M. Nakariakov, and T. D. Arber. Sausage oscillations of coronal loops. *A&A*, 461:1149–1154, January 2007. doi: 10.1051/0004-6361:20065986.
- P. Petkaki, C. E. J. Watt, R. B. Horne, and M. P. Freeman. Anomalous resistivity in non-Maxwellian plasmas. *Journal of Geophysical Research (Space Physics)*, 108:1442–+, December 2003. doi: 10.1029/2003JA010092.
- C. D. Pike and H. E. Mason. Rotating Transition Region Features Observed with the SOHO Coronal Diagnostic Spectrometer. *Sol. Phys.*, 182:333–348, October 1998.
- E. Priest and T. Forbes, editors. *Magnetic reconnection : MHD theory and applications*, 2000.
- R. Rankin, P. Frycz, V. T. Tikhonchuk, and J. C. Samson. Nonlinear standing shear Alfvén waves in the Earth’s magnetosphere. *J. Geophys. Res.*, 99:21291–21302, November 1994. doi: 10.1029/94JA01629.
- M. P. Riutova. Negative energy waves in a plasma with structured magnetic fields. *Zhurnal Eksperimental noi i Teoreticheskoi Fiziki*, 94:138–151, August 1988.
- B. Roberts. On magnetohydrodynamic solitons in jets. *ApJ*, 318:590–594, July 1987. doi: 10.1086/165395.
- B. Roberts and A. R. Webb. Vertical motions in an intense magnetic flux tube. *Sol. Phys.*, 56:5–35, January 1978. doi: 10.1007/BF00152630.
- B. Roberts and A. R. Webb. Vertical motions in an intense magnetic flux tube. III - On the slender flux tube approximation. *Sol. Phys.*, 64:77–92, November 1979. doi: 10.1007/BF00151117.

- B. Roberts, P. M. Edwin, and A. O. Benz. On coronal oscillations. *ApJ*, 279: 857–865, April 1984.
- M. S. Ruderman. Coronal Loop Heating by Torsional Alfvén Waves Directly Driven by Footpoint Motions: Harmonic Driving versus Stochastic Driving. *ApJ*, 521: 851–858, August 1999. doi: 10.1086/307584.
- M. S. Ruderman. Comment on “Slow nonlinear waves in magnetic flux tubes” [Phys. Plasmas 11, 2256 (2004)]. *Physics of Plasmas*, 12(3):034701–+, March 2005. doi: 10.1063/1.1856931.
- M. S. Ruderman, E. Verwichte, R. Erdelyi, and M. Goossens. Dissipative instability of the MHD tangential discontinuity in magnetized plasmas with anisotropic viscosity and thermal conductivity. *Journal of Plasma Physics*, 56:285–306, November 1996.
- M. P. Ryutova and S. R. Habbal. The Effects on Mass Flows on the Dissipation of Alfvén Waves in the Upper Layers of the Solar Atmosphere. *ApJ*, 451:381–+, September 1995. doi: 10.1086/176227.
- K. Shibata, Y. Ishido, L. W. Acton, K. T. Strong, T. Hirayama, Y. Uchida, A. H. McAllister, R. Matsumoto, S. Tsuneta, T. Shimizu, H. Hara, T. Sakurai, K. Ichimoto, Y. Nishino, and Y. Ogawara. Observations of X-ray jets with the YOHKOH Soft X-ray Telescope. *PASJ*, 44:L173–L179, October 1992.
- K. Shibata, T. Nakamura, T. Matsumoto, K. Otsuji, T. J. Okamoto, N. Nishizuka, T. Kawate, H. Watanabe, S. Nagata, S. UeNo, R. Kitai, S. Nozawa, S. Tsuneta, Y. Suematsu, K. Ichimoto, T. Shimizu, Y. Katsukawa, T. D. Tarbell, T. E. Berger, B. W. Lites, R. A. Shine, and A. M. Title. Chromospheric Anemone Jets as Evidence of Ubiquitous Reconnection. *Science*, 318:1591–, December 2007. doi: 10.1126/science.1146708.
- M. Shimojo, S. Hashimoto, K. Shibata, T. Hirayama, H. S. Hudson, and L. W. Acton. Statistical Study of Solar X-Ray Jets Observed with the YOHKOH Soft X-Ray Telescope. *PASJ*, 48:123–136, February 1996.
- P. K. Shukla and R. Bingham. Generation of Density Enhancements by Magnetohydrodynamic Waves. *Physica Scripta Volume T*, 107:250–+, 2004. doi: 10.1238/Physica.Topical.107a00250.

- A. K. Srivastava, T. V. Zaqarashvili, W. Uddin, B. N. Dwivedi, and P. Kumar. Observation of multiple sausage oscillations in cool post-flare loop. *MNRAS*, 388: 1899–1903, August 2008. doi: 10.1111/j.1365-2966.2008.13532.x.
- T. K. Suzuki. Coronal heating and acceleration of the high/low-speed solar wind by fast/slow MHD shock trains. *MNRAS*, 349:1227–1239, April 2004. doi: 10.1111/j.1365-2966.2004.07570.x.
- T. K. Suzuki. Structured Red Giant Winds with Magnetized Hot Bubbles and the Corona/Cool Wind Dividing Line. *ApJ*, 659:1592–1610, April 2007. doi: 10.1086/512600.
- T. K. Suzuki. Coronal heating and wind acceleration by nonlinear Alfvén waves - global simulations with gravity, radiation, and conduction. *Nonlinear Processes in Geophysics*, 15:295–304, March 2008.
- T. K. Suzuki and S.-i. Inutsuka. Making the Corona and the Fast Solar Wind: A Self-consistent Simulation for the Low-Frequency Alfvén Waves from the Photosphere to 0.3 AU. *ApJ*, 632:L49–L52, October 2005. doi: 10.1086/497536.
- T. K. Suzuki, K. Sumiyoshi, and S. Yamada. Alfvén Wave-Driven Supernova Explosion. *ApJ*, 678:1200–1206, May 2008. doi: 10.1086/533515.
- Z. Svestka. Slow-mode oscillations of large-scale coronal loops. *Sol. Phys.*, 152: 505–508, July 1994. doi: 10.1007/BF00680454.
- Z. Svestka, B. R. Dennis, B. E. Woodgate, M. Pick, A. Raoult, C. G. Rapley, and R. T. Stewart. Unusual coronal activity following the flare of 6 November 1980. *Sol. Phys.*, 80:143–159, September 1982. doi: 10.1007/BF00153429.
- K. F. Tapping. A torsional wave model for solar radio pulsations. *Sol. Phys.*, 87: 177–186, August 1983. doi: 10.1007/BF00151168.
- M. Terra-Homem, R. Erdélyi, and I. Ballai. Linear and non-linear MHD wave propagation in steady-state magnetic cylinders. *Sol. Phys.*, 217:199–223, November 2003.
- J. Terradas and L. Ofman. Loop Density Enhancement by Nonlinear Magnetohydrodynamic Waves. *ApJ*, 610:523–531, July 2004. doi: 10.1086/421514.

- V. T. Tikhonchuk, R. Rankin, P. Frycz, and J. C. Samson. Nonlinear dynamics of standing shear Alfvén waves. *Physics of Plasmas*, 2:501–515, February 1995. doi: 10.1063/1.870975.
- S. Tomczyk, S. W. McIntosh, S. L. Keil, P. G. Judge, T. Schad, D. H. Seeley, and J. Edmondson. Alfvén Waves in the Solar Corona. *Science*, 317:1192–, August 2007.
- U. Torkelsson and G. C. Boynton. Non-linear spherical Alfvén waves. *MNRAS*, 295: 55–+, March 1998. doi: 10.1046/j.1365-8711.1998.t01-1-29511160.x.
- M. Ugai. Basic Physical Mechanism of Fast Reconnection Evolution in Space Plasmas. *Space Sci. Rev.*, 95:601–611, January 2001.
- T. Van Doorselaere, C. S. Brady, E. Verwichte, and V. M. Nakariakov. Seismological demonstration of perpendicular density structuring in the solar corona. *A&A*, 491:L9–L12, November 2008a. doi: 10.1051/0004-6361:200810659.
- T. Van Doorselaere, V. M. Nakariakov, and E. Verwichte. Detection of Waves in the Solar Corona: Kink or Alfvén? *ApJ*, 676:L73–L75, March 2008b. doi: 10.1086/587029.
- T. Van Doorselaere, V. M. Nakariakov, and E. Verwichte. Coronal loop seismology using multiple transverse loop oscillation harmonics. In R. Erdélyi & C. A. Mendoza-Briceño, editor, *IAU Symposium*, volume 247 of *IAU Symposium*, pages 140–146, May 2008c. doi: 10.1017/S1743921308014798.
- S. Vasheghani Farahani, T. Van Doorselaere, E. Verwichte, and V. M. Nakariakov. Propagating transverse waves in soft X-ray coronal jets. *A&A*, 498:L29–L32, May 2009. doi: 10.1051/0004-6361/200911840.
- S. Vasheghani Farahani, V. M. Nakariakov, and T. Van Doorselaere. Long-wavelength torsional modes of solar coronal plasma structures. *A&A*, 517:A29+, July 2010. doi: 10.1051/0004-6361/201014502.
- S. Vasheghani Farahani, V. M. Nakariakov, T. van Doorselaere, and E. Verwichte. Nonlinear long-wavelength torsional Alfvén waves. *A&A*, 526:A80+, February 2011. doi: 10.1051/0004-6361/201016063.

- G. Verth, R. Erdélyi, and M. Goossens. Magnetoseismology: Eigenmodes of Torsional Alfvén Waves in Stratified Solar Waveguides. *ApJ*, 714:1637–1648, May 2010. doi: 10.1088/0004-637X/714/2/1637.
- E. Verwichte, V. M. Nakariakov, and A. W. Longbottom. On the evolution of a nonlinear Alfvén pulse. *Journal of Plasma Physics*, 62:219–232, August 1999. doi: 10.1017/S0022377899007771.
- E. Verwichte, V. M. Nakariakov, and F. C. Cooper. Transverse waves in a post-flare supra-arcade. *A&A*, 430:L65–L68, January 2005.
- R. W. Walsh and J. Ireland. The heating of the solar corona. *A&A Rev.*, 12:1–41, 2003. doi: 10.1007/s00159-003-0021-9.
- T. Wang, S. K. Solanki, W. Curdt, D. E. Innes, and I. E. Dammasch. Doppler Shift Oscillations of Hot Solar Coronal Plasma Seen by SUMER: A Signature of Loop Oscillations? *ApJ*, 574:L101–L104, July 2002. doi: 10.1086/342189.
- T. J. Wang, S. K. Solanki, W. Curdt, D. E. Innes, I. E. Dammasch, and B. Kliem. Hot coronal loop oscillations observed with SUMER: Examples and statistics. *A&A*, 406:1105–1121, August 2003a. doi: 10.1051/0004-6361:20030858.
- T. J. Wang, S. K. Solanki, D. E. Innes, W. Curdt, and E. Marsch. Slow-mode standing waves observed by SUMER in hot coronal loops. *A&A*, 402:L17–L20, May 2003b. doi: 10.1051/0004-6361:20030448.
- C. E. J. Watt, R. B. Horne, and M. P. Freeman. Ion-acoustic resistivity in plasmas with similar ion and electron temperatures. *Geophys. Res. Lett.*, 29(1):010000–1, January 2002. doi: 10.1029/2001GL013451.
- D. R. Williams, K. J. H. Phillips, P. Rudawy, M. Mathioudakis, P. T. Gallagher, E. O’Shea, F. P. Keenan, P. Read, and B. Rompolt. High-frequency oscillations in a solar active region coronal loop. *MNRAS*, 326:428–436, September 2001.
- T. Yokoyama and K. Shibata. Magnetic Reconnection as the Origin of X-Ray Jets and H α Surges on the Sun. *Nature*, 375:42–+, May 1995.
- T. V. Zaqarashvili. Observation of coronal loop torsional oscillation. *A&A*, 399:L15–L18, February 2003. doi: 10.1051/0004-6361:20030084.

- T. V. Zaqarashvili and K. Murawski. Torsional oscillations of longitudinally inhomogeneous coronal loops. *A&A*, 470:353–357, July 2007. doi: 10.1051/0004-6361:20077246.
- I. D. Zhugzhda and N. S. Dzhililov. Transformation of magnetogravitational waves in the solar atmosphere. *A&A*, 112:16–23, August 1982.
- Y. D. Zhugzhda. Force-free thin flux tubes: Basic equations and stability. *Physics of Plasmas*, 3:10–21, January 1996. doi: 10.1063/1.871836.
- Y. D. Zhugzhda. From thin-flux-tube approximation to two-mode approximation. *Physics of Plasmas*, 9:971–978, March 2002. doi: 10.1063/1.1447254.
- Y. D. Zhugzhda. Response to “Comment on ‘Slow nonlinear waves in magnetic flux tubes’” [Phys. Plasmas 12, 034701 (2005)]. *Physics of Plasmas*, 12(3):034702–+, March 2005. doi: 10.1063/1.1856932.
- Y. D. Zhugzhda and M. Goossens. Hidden problems of thin-flux-tube approximation. *A&A*, 377:330–342, October 2001. doi: 10.1051/0004-6361:20011094.
- Y. D. Zhugzhda and V. M. Nakariakov. Linear and nonlinear magnetohydrodynamic waves in twisted magnetic flux tubes. *Physics Letters A*, 252:222–232, March 1999. doi: 10.1016/S0375-9601(99)00014-6.